The g-factor of the electron bound in $^{28}\text{Si}^{13+}$:
The most stringent test of bound-state quantum electrodynamics

Sven Sturm

geboren in Koblenz

Mainz, den 21.12.2011

1. Gutachter: Prof. Dr. Klaus Blaum
2. Gutachter: Prof. Dr. Werner Heil

Der g-Faktor des gebundenen Elektrons in $^{28}\text{Si}^{13+}$: Der empfindlichste Test der Quantenelektrodynamik gebundener Zustände.

In dieser Arbeit wird die ultra-hochpräzise experimentelle Bestimmung des g-Faktors des in wasserstoffähnlichem $^{28}\text{Si}^{13+}$ gebundenen Elektrons beschrieben. Das Experiment basiert auf der gleichzeitigen Bestimmung der Zyklotron- und Larmorfrequenz eines einzelnen Ions, dass in einem dreifach-Penningfallensystem gespeichert ist. Dabei wird der kontinuierliche Stern-Gerlach Effekt genutzt, der einen nicht-destruktiven Nachweis des Spinzustandes durch eine Kopplung des Spins des gebundenen Elektrons an die Bewegungsfrequenzen des Ions mittels einer magnetischen Flasche ermöglicht. Dazu wurde ein hochempfindliches, kryogenes Nachweissystem entwickelt, das eine direkte, nichtdestruktive Messung der Eigenfrequenzen mit der erforderlichen Präzision erlaubt. Die Entwicklung eines neuartigen, phasensensitiven Nachweisverfahrens erlaubte schließlich die Bestimmung des g-Faktors mit einer bisher unerreichbaren relativen Genauigkeit von $4 \cdot 10^{-11}$. Der Vergleich des so ermittelten Wertes mit dem von der Quantenelektrodynamik (QED) vorhergesagten erlaubt die Überprüfung der Gültigkeit dieser fundamentalen Theorie unter den extremen Bedingungen des starken Bindungspotentials des hochgeladenen Ions. Die exakte Übereinstimmung von Theorie und Experiment ist eine eindrucksvolle Demonstration der Genauigkeit der QED. Die in dieser Arbeit geschaffenen experimentellen Möglichkeiten erlauben in naher Zukunft nicht nur weitergehende Tests der Theorie, sondern auch die Bestimmung der Masse des Elektrons mit einer Genauigkeit, die den bisherigen Literaturwert um mehr als eine Größenordnung übertrifft.

The g-factor of the electron bound in $^{28}\text{Si}^{13+}$: The most stringent test of bound-state quantum electrodynamics

This thesis describes the ultra-precise determination of the g-factor of the electron bound to hydrogenlike $^{28}\text{Si}^{13+}$. The experiment is based on the simultaneous determination of the cyclotron- and Larmor frequency of a single ion, which is stored in a triple Penning-trap setup. The continuous Stern-Gerlach effect is used to couple the spin of the bound electron to the motional frequencies of the ion via a magnetic bottle, which allows the non-destructive determination of the spin state. To this end, a highly sensitive, cryogenic detection system was developed, which allowed the direct, non-destructive detection of the eigenfrequencies with the required precision. The development of a novel, phase sensitive detection technique finally allowed the determination of the g-factor with a relative accuracy of $4 \cdot 10^{-11}$, which was previously inconceivable. The comparison of the hereby determined value with the value predicted by quantumelectrodynamics (QED) allows the verification of the validity of this fundamental theory under the extreme conditions of the strong binding potential of a highly charged ion. The exact agreement of theory and experiment is an impressive demonstration of the exactness of QED. The experimental possibilities created in this work will allow in the near future not only further tests of theory, but also the determination of the mass of the electron with a precision that exceeds the current literature value by more than an order of magnitude.

Contents

List of Figures

List of Tables

1. Introduction

Quantum electrodynamics (QED, see [1] and the references therein), the theory of the interaction of light and matter, was established by Richard P. Feynman, Julian Schwinger and Sin-Itiro Tomonaga in the 1940s, who received the Nobel Prize in 1965 for this fundamental work. QED is today considered to be the most successful of all quantum field theories in the Standard Model [2]. This is on the one hand owed to the capability of the theory to predict physical observables with impressive precision, on the other hand the scope of validity of QED seems to cover all energy and field scales that are accessible to current experiments. Furthermore, the detailed understanding of the electromagnetic interaction is an indispensable foundation for most natural sciences. The evident importance of QED motivated a number of fascinating experiments that aimed for the verification of its predictions. Indeed, despite the impressive precision of these tests, no discrepancy between theoretical prediction and experimental observation has ever been observed.

Among the most prominent of these tests are the determinations of the electron g-factors. The g-factor, which determines the magnetic moment of the electron due to its spin, can be predicted extremely accurately within the framework of QED [3]. The slight deviation of the free electron g-factor from the naive Dirac value of 2 [4] due to the coupling to the radiation field (electron anomaly), described by QED, has been measured by Dehmelt and coworkers in the 1980s [5]. In 1989, Dehmelt received the Nobel Prize, together with Wolfgang Paul and Norman Ramsey, for his work on Penning traps. The refinement of his experiment by Gabrielse in Harvard [6] lead to the determination of the electron anomaly with a relative uncertainty of 0.3 ppb[1]. By comparing the determined value with the theoretical prediction, making use of the tabulated value of the fine structure constant, allows to test QED to about 0.7 ppb.

However, the stringency of this test is restricted to the regime of low field strength. It is therefore of great interest to perform similar tests in the presence of large field

---

[1]parts per billion, 1 part in 10^9

strengths, where hypothetical nonlinearities of QED in the field tensor $F^{\mu\nu}$ become observable. A couple of experiments have been performed on this account, which make use of highly charged ions to provide the highest field strengths available in the laboratory, which range up to 10^{16} V/cm in hydrogenlike uranium. Among the most important measurements are the hyperfine structure of ^{207}Pb^{81+} [7] and the Lamb-shift in ^{238}U^{91+} [8]. However, although these experiments enable tests of the theory in the strongest fields, the significance is limited due to the strong influence of nuclear structure on these values. In order to bridge the gap in precision, a series of experiments to determine the g-factor of bound electrons in highly charged ions has been started at the Johannes Gutenberg-University of Mainz. The g-factor of the bound electron is altered considerably from the free electron case by the interaction of the electron with the binding potential of the nucleus, but the influence of the nuclear structure is significantly lower. The experiment is conceptually similar to the free electron experiments and also makes use of the continuous Stern-Gerlach effect [9]. However, the determination of atomic g-factors imposes additional difficulties for the experiments, due to the drastically larger mass which complicates the detection of the spin state considerably. These experimental challenges have been addressed by the team around H.-J. Kluge, G. Werth, W. Quint and S. Stahl, which culminated in the determinations of the g-factors of hydrogenlike carbon [10] and oxygen [11], conducted by H. Häffner and J. Verdú and coworkers, with an impressive precision of about 1 ppb. The apparatus constructed for this experiment for the first time comprised two Penning traps, one for the precision frequency measurements, termed the Precision Trap (PT), and a second trap that provides the magnetic bottle field for the spin state detection, which was called Analysis Trap (AT). The combination of these two traps allowed to probe the spin transition with microwaves in the homogeneous magnetic field of the PT and to detect successful transitions in the AT. The comparison of the experimentally determined g-factors with bound-state quantum electrodynamic (BS-QED) calculations constitute an important verification of QED in the regime of intermediate field strength.

Despite the great success of these experiments, the constructed apparatus limited the extension of the measurements towards heavier systems. For this reason, a complete rebuild of the setup, incorporating significant technical improvements, became necessary. In addition to the two traps AT and PT, the new apparatus includes a dedicated electron beam ion source and trap (EBIS/T) for the charge-breeding of medium-heavy ions. Within the course of this thesis large parts of the electronics, both for the room temperature and the cryogenic section, and crucial parts of the new setup have been developed. The formidable performance of the new apparatus not only allowed the challenging determination of the g-factor of hydrogenlike silicon [12], but simultaneously enabled to cut down the dominant systematic shifts of the experiment by orders of magnitude and to reach significantly improved precision. Furthermore, a novel phase sensitive frequency detection technique was developed [13] and applied during a second measurement run, which yielded a previously inaccessible precision of 40 ppt[2], an improvement by almost 2 orders of magnitude

---

[2]parts per trillion, 1 part in 10^{12}

compared to previous experiments. In combination with several further improvements that have been driven forth, this paves the way for intriguing measurements, including further tests of fundamental theories and ultra-precision metrology. The results presented in this thesis, combined with the theoretical predictions, currently constitute the most stringent test of QED in strong fields.

This thesis is organized as follows: Chapter 2 gives a short introduction into quantum electrodynamics and specifically into the effects that determine the g-factor. Chapter 3 describes the Penning trap in general, the most important tool used in this work, and some of the techniques used to manipulate and observe ions stored therein. In this context, also the dominant systematic frequency shifts are discussed. Chapter 4 describes the newly developed triple-trap apparatus and details the development of the detection system, which constitutes the heart of this experiment. Furthermore, exemplary results obtained with the developed electronics are shown. Chapter 5 is devoted to the presentation of experimental techniques and the possibilities they open up. Moreover, the novel PnA detection technique and its experimental implementation is introduced. After all elements of the experiment have been presented, chapter 6 finally illustrates the results of the two g-factor measurements performed in this work, one with the traditional cyclotron frequency measurement technique and a second one with the novel PnA method. Both measurements agree perfectly with each other and with the theoretical prediction. The last chapter concludes the thesis and gives an outlook onto the exciting perspectives of this experiment.

2. Quantum Electrodynamics

Quantum electrodynamics (QED) is a fundamental quantum field theory that describes the interaction of fermions with electromagnetic fields mediated by photons. Today QED is considered the most successful of all current theories within the Standard Model of physics, a result of the high predictive power of the theory. The first attempts to build a quantum field theory that would be able to describe the interaction of charged particles with the electromagnetic radiation field were started by Dirac in the late 1920s [14]. However, his results were only in lowest order leading to interpretable results but led to divergences in higher orders. It was not until 1942, when experimental results had already shown that the established theory is giving imperfect predictions [15], that Richard P. Feynman, together with Julian Schwinger and Shinichirō Tomonaga, was able to resolve the problems in the formalism put forth by Dirac by appropriate renormalization. His formulation of QED is based on so-called Feynman diagrams that represent the fundamental interaction at discrete vertices. The interaction strength is ruled by a single number, the fine-structure constant $\alpha \simeq \frac{1}{137.035999679(94)}$. The small value of α causes higher order terms of perturbation theory to contribute less although the number of Feynman diagrams increases with the order. This allows high precision calculations with only a reasonable number of processes being considered.

The newly found theory was hereafter used to predict values for a number of physical observables with intriguing precision. In the last 60 years there was considerable effort to test QED predictions experimentally with continually improving accuracy, yet there was not a single discrepancy found. Nevertheless, the Standard Model and with it also QED, is expected to be incomplete and fail in the limit of high energies or high field strength. In fact it is assumed that the Standard Model is a low-energy approximation of a more fundamental theory that will eventually be able to describe all processes in the universe from its genesis [16]. It is therefor of utmost interest to test the range of validity of QED in order to find an indication for the structure of the superior theory.

On the experimental side the QED of free particles is already tested extensively

and the corresponding comparison between theoretical results and experimental observation demonstrates the remarkable predictive power of QED. Among the most imposing tests is the g-factor of the free electron that has been measured in the Harvard g-2 experiment by Gabrielse *et al.* [6] and is in perfect agreement with the theoretical value that has been calculated using the fine-structure constant derived in an independent photon recoil measurement[17]:

$$\frac{g_{\text{exp}} - 2}{2} \quad = \quad 1.159\,652\,180\,73(28)\ 10^{-3}\,[6] \tag{2.1}$$

$$\frac{g_{\text{theo}} - 2}{2} \quad = \quad 1.159\,652\,181\,13(84)\ 10^{-3}\,[3,\ 17]. \tag{2.2}$$

In the regime of high interaction energy, the measurement of cross-sections for lepton scattering and production can provide a percent-level test [18].

By studying bound systems, many more interesting observables become accessible. A bound system can be isolated from external influences while the binding potential itself can reach impressive values, especially in highly charged systems where the $1s_{1/2}$ level is very close to the nucleus. This allows to test QED in extreme field strength, which might increase the chance to grasp the boundary of the scope of validity of QED. In order to provide a conclusive test of theory, simple systems are of special interest. In these systems, it is possible to identify observables that can be both calculated and measured with high accuracy. Furthermore, both experiment and theory must be able to give correct confidence intervals. There are a number of experiments with bound systems, such as the measurement of the Lamb-shift of hydrogenlike $^{238}\text{U}^{91+}$ [8] that allows a test of bound-state QED (BS-QED) on the percent level, and the hyperfine-splitting in heavy ions [7], that allows for tests in the 10% range. The tests on the basis of these experiments are limited by the accuracy of the theoretical value rather than the experimental accuracy. This is, among other things, a result of the large influence of the nuclear charge distribution on the measured value. The lower influence of this value on the electronic spin g-factor constitutes an important advantage.

2.1   The *g*-factor of the free electron

The determination of the g-factor of the free electron by directly measuring the electron anomaly renders the most precise test of the free QED in the low field range. Historically, the anomaly of the electron has been measured throughout the last 50 years, from the first experiments of Kusch and Foley [19], to the modern experiments of H. Dehmelt and G. Gabrielse [5, 6], an evolution that expresses the impact of these measurements.

The magnetic moment of the electron can be written as the product of the spin vector ($\mathbf{S}$[1]), the Bohr magneton ($\mu_B = \frac{e\hbar}{2m_e}$) and the dimensionless quantity g_s[2]:

$$\boldsymbol{\mu} = -g_s \mu_B \frac{\mathbf{S}}{\hbar},$$

where e/m_e is the charge-to-mass ratio of the electron and $\hbar$ the Planck constant $h/2\pi$. If exposed to a magnetic field, the energy of the particle thus depends on the direction of the spin orientation as $\Delta E = -\boldsymbol{\mu}\mathbf{B}$. The value of g is predicted by the Dirac equation to be exactly 2. This solution assumes a freely propagating electron that couples to a homogeneous background magnetic field. However, in the scope of QED, the electron can interact with the complete electromagnetic field rather than just passively feel the static externally applied magnetic field. This coupling to the electromagnetic field (both real and virtual) alters the energy of the particle and thus accordingly the g-factor. The QED contributions can be expanded in a power series of the fine-structure constant, according to the number of vertices in the corresponding Feynman graphs [20]:

$$g_{\text{free}} = 2 \ \left(C_0 + C_2 \left(\tfrac{\alpha}{\pi} \right) + C_4 \left(\tfrac{\alpha}{\pi} \right)^2 + C_6 \left(\tfrac{\alpha}{\pi} \right)^3 + C_{10} \left(\tfrac{\alpha}{\pi} \right)^5 \right. \tag{2.3}$$

$$\left. + \ldots + a_{\text{heavy lepton,hadronic,weak}} \right) \tag{2.4}$$

The leading contribution is due to the self-energy, where the electron temporarily "stores" part of its energy in a virtual photon while it interacts with the external field. The corresponding Feynman diagram is shown in figure 2.1. Mainly due to historical
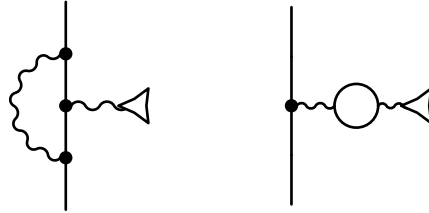
Figure 2.1: Feynman diagrams for the lowest order contributions to the free electron g-factor. The plain line stands for a freely propagating electron, the wavy line is a virtual photon and the dots are interaction vertices. The triagram depicts the coupling to the external magnetic field. The closed loop in the right diagram depicts the creation and annihilation of a virtual lepton / anti-lepton pair (vacuum polarization).

reasons, the vacuum polarization, i.e. the creation of virtual lepton / anti-lepton pairs from the interaction photon, is not considered in the first order because for the electron with its low mass this effect is rather small. However, in the case of the muon

---

[1] Bold faced letters denote vectorial quantities.
[2] In the following, the electron spin g-factor g_s is denoted only as g, since in the context of our experiment the orbital angular momentum always vanishes.

g-factor, this effect increases significantly [21]. The coefficient C_2 can be analytically calculated (as well as the C_4 and the C_6 terms) and has the value 0.5, showing that the QED contribution to the free electron g-factor is on the order of $0.12\,\%$. Here, the advantage of the direct measurement of the anomaly becomes obvious as it increases the precision of the final g-factor value by almost three orders of magnitude. The theoretical g-factor obviously has a dependence on the fine-structure constant, motivating an independent measurement of α in order to complete the QED test. Currently, the most precise independent α-value comes from a rubidium recoil measurement [17], which results in a $\sim$0.7 ppb test of the QED calculations. The last term in equation (2.4) shows that at the current level of precision also the coupling to virtual heavy particles has to be taken into account. The g-factor has the fascinating property that it depends on contributions from all possible particles interacting with the electron. With further increasing resolution, this might be used to test for the existence of unknown particles such as speculative light dark matter [6].

2.2   The g-factor of the bound electron

Even though the free electron g-factor already constitutes an intriguing test for QED theory, the determination of the same value for an electron bound to a strong potential, imposes an even more stringent test in the sense that theory is more likely to break down under the influence of extremely strong fields. Highly charged hydrogenlike ions provide an ideal environment for such tests since these systems are relatively simple to calculate and provide electric field strengths not available elsewhere in laboratories. In the case of the hydrogenlike $^{28}\text{Si}^{13+}$ ion that personates the protagonist of this thesis, the expectation value for the $1\text{s}_{1/2}$ state is close to 10^{14} V/cm. Figure 2.2 shows the field strength in hydrogenlike ions as a function of the nuclear charge Z.

   In the past, the g-factors of $^{12}\text{C}^{5+}$ and $^{16}\text{O}^{7+}$ were already determined with accuracies in the order of $\frac{\delta g}{g} \simeq 10^{-9}$. The extension of these measurement to higher charge states required a complete reconstruction of the setup, and the advances realized within this thesis work lead to the possibility to test BS-QED in a significantly higher field strength while simultaneously a further breakthrough in experimental accuracy was achieved.

2.2.1   Implications of the binding potential

The presence of a strong binding potential alters the g-factor of the electron and with it also the theoretical calculations, a fact which is accounted for by calling these calculations bound-state QED. The description of an electron bound to a heavy nucleus demands the QED propagator of the electron to be a solution of the Dirac equation in the potential of the charge distribution of the nucleus. Although this propagator can be readily constructed [22], the calculation of the corresponding Feynman graphs raises major difficulties concerning the renormalization. To date, only the contributions up to the one-loop level have been calculated using the full
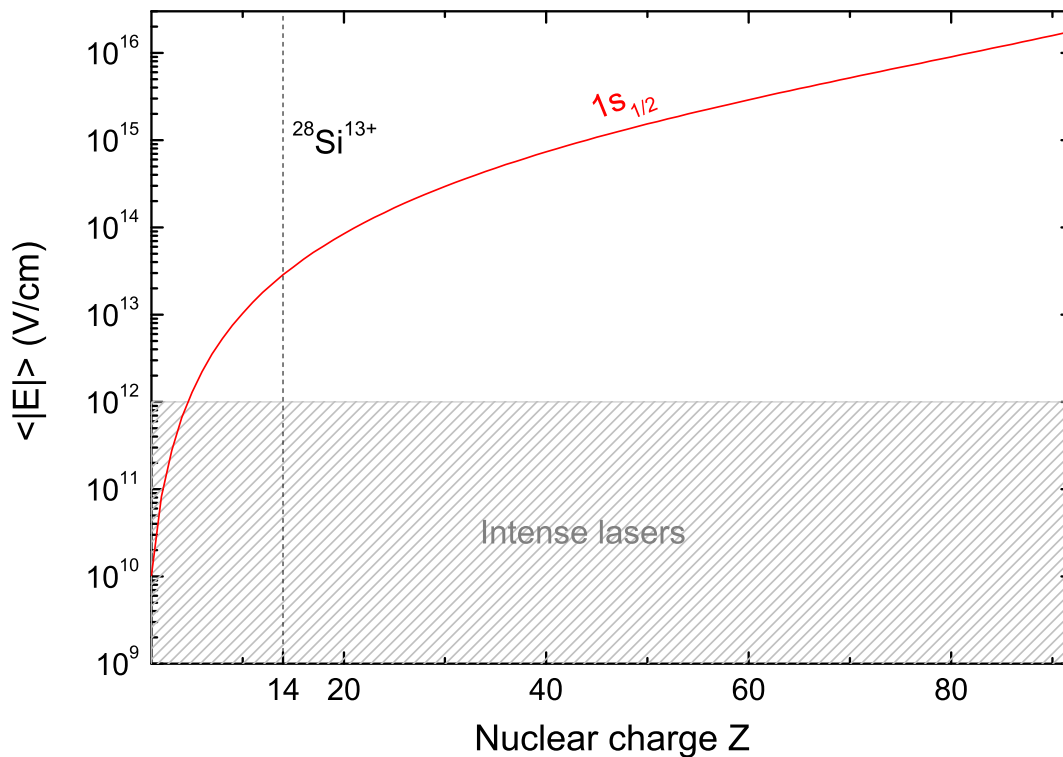
Figure 2.2: Expectation value of the electric field strength for the $1s_{1/2}$ state in hydrogenlike ions. The hatched area shows the electric field range provided by the most intense lasers available today.

bound-state propagator. The two-loop diagrams are evaluated as a second expansion in orders of $(Z\alpha)$, a value that comes close to unity when considering highly charged ions, putting this expansion into question at least for heavy nuclei. Already for $^{28}Si^{13+}$ as investigated here, the uncalculated higher order terms of this expansion constitute the dominating uncertainty of the theoretical value [12]. In the following, the contributions that are considered at the current level of accuracy are introduced.

2.2.2 Relativistic Corrections

The most important difference to the free electron *g*-factor comes already from the solution of the Dirac equation of the electron in the potential of a point-charge with infinite mass. This approximation leads to additional correction terms that are evaluated independently. The so-called relativistic correction was first introduced by Breit in 1928 [23]. In fact the term "correction" is misleading in this context, since it is the direct relativistic solution of the Dirac equation rather than an additional term. The evaluation is straightforward and requires only the calculation of the

expectation value of the magnetic energy of the spin in the well-known 1s state with wave function $|\psi_{100}\rangle$ of a pure Coulomb field:

$$
\begin{aligned}
\Delta E &= -\langle\psi_{100} \mid \boldsymbol{\mu}\mathbf{B} \mid \psi_{100}\rangle = g_s m_z \mu_B B \\
\Rightarrow \quad g_{\mathrm{Breit}} &= -\frac{\langle\psi_{100} \mid \boldsymbol{\mu}\mathbf{B} \mid \psi_{100}\rangle}{m_z \mu_B B} = \frac{2(1 + 2\sqrt{1 - (Z\alpha)^2})}{3}.
\end{aligned}
\tag{2.5}
$$

The relativistic treatment of the electron motion causes a L-S spin orbit interaction between the large and small components of the Dirac equation even for the 1s state. The Breit term makes the g-factor smaller than the value of 2 for the free electron. The effect amounts to 10 ppm of the total g-factor for the hydrogen atom and 5% for hydrogenlike uranium.

2.2.3 Bound-state QED corrections

The radiative corrections originating in the interaction of the quantized electromagnetic field and the electron that are described by QED theory. They constitute, unlike in the case of the free electron, only a smaller correction, causing the g-factor to be smaller than 2 for all $Z > 8$. Analogous to the free electron g-factor, the radiative corrections are evaluated as a series expansion in the fine-structure constant α, corresponding to an ordering of the Feynman diagrams according to the number of emitted virtual photons. However, beyond the coupling to the external magnetic field, the coupling to the binding potential of the nucleus has to be taken into consideration. As already mentioned the additional series expansion in powers of $(Z\alpha)$, corresponding to the number of photons exchanged with the nucleus, is not converging properly for highly charged ions. The most elegant solution is to use an electron propagator that has to been constructed from the solution of the Dirac equation in the binding potential of the nucleus [22]. This way, the interaction with the nucleus is already incorporated in the propagator in all orders of $(Z\alpha)$ and the number of Feynman diagrams that have to be evaluated decreases drastically. Figure 2.3 shows the BS-QED diagrams contributing to the g-factor in first order. The increased complexity of the resulting expressions, however, inhibits an analytical solution and forces a numerical evaluation. Only the diagrams in second order of α have been evaluated in orders of $(Z\alpha)$, justified by the lower relative size of these contributions. Nevertheless, the uncertainty arising from the uncalculated higher order contributions is dominating the theoretical error budget.

2.2.3.1 Nuclear recoil correction

When solving the equations of motion of the electron in the constant central binding potential, the motion of the nucleus due to the recoil from the electron was neglected. Though this is a decent approximation considering the mass ratio $\frac{m_e}{m_{\mathrm{nucl}}}$, in the context of the experimental accuracy of the experiment achieved to date, this has to be taken into account as a correction to the g-factor. The most recent calculations are presented in [24] and are based on an expansion in the product $(Z\alpha)\frac{m_e}{m_{\mathrm{nucl}}}$. The remaining uncertainty of higher order can be neglected at the current level of precision.
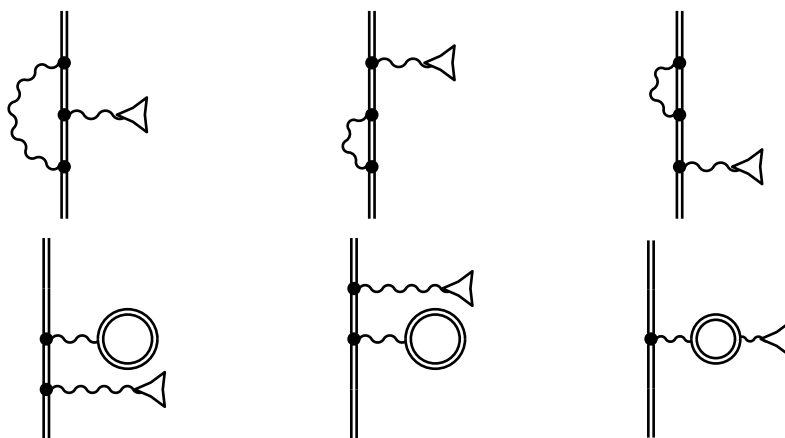
Figure 2.3: Feynman diagrams of BS-QED in first order of α. The double line depicts the BS-QED electron propagator. Additional to the direct analogons to the free electron g-factor, 4 causal permutations have to be considered that were already included in the mass and charge renormalization of the electron propagator for the free electron.

2.2.3.2 Finite nuclear size correction

The Dirac equation is solved for a pure Coulomb potential in order to derive the electron propagator. However, since the charge distribution of the nucleus itself has a finite size, the potential is altered for radii smaller than the nuclear charge radius. This in turn has to be taken into account as a correction to the g-factor. If nuclear levels can be excited by virtual photons, a resulting deformation can furthermore change the radial symmetry of the nucleus [25, 26]. However, due to the arbitrary orientation of the nucleus, the effect mainly manifests as a tiny change in the effective charge radius, the explicitly shape dependent terms are negligible on the current level of precision [25]. The dependence of the g-factor on the charge radius allows in the converse argument to determine the charge radius from a g-factor measurement, if QED is believed to be correct at the required precision. In chapter 6, the charge radius of ^{28}Si is determined as a proof of principle and found to be in excellent agreement with the tabulated value. The nuclear corrections can be discriminated from the remaining effects by measuring the so-called isotope effect, i.e. the difference in g-factor for two isotopes of the same element. The theoretical accuracy is significantly higher for this difference since most of the limiting contributions from uncalculated higher order terms cancel. Such a measurement in currently under preparation in the Ph.D. thesis of Anke Wagner. In Figure 2.4 and table 2.1 all contributions to the g-factor are summarized.
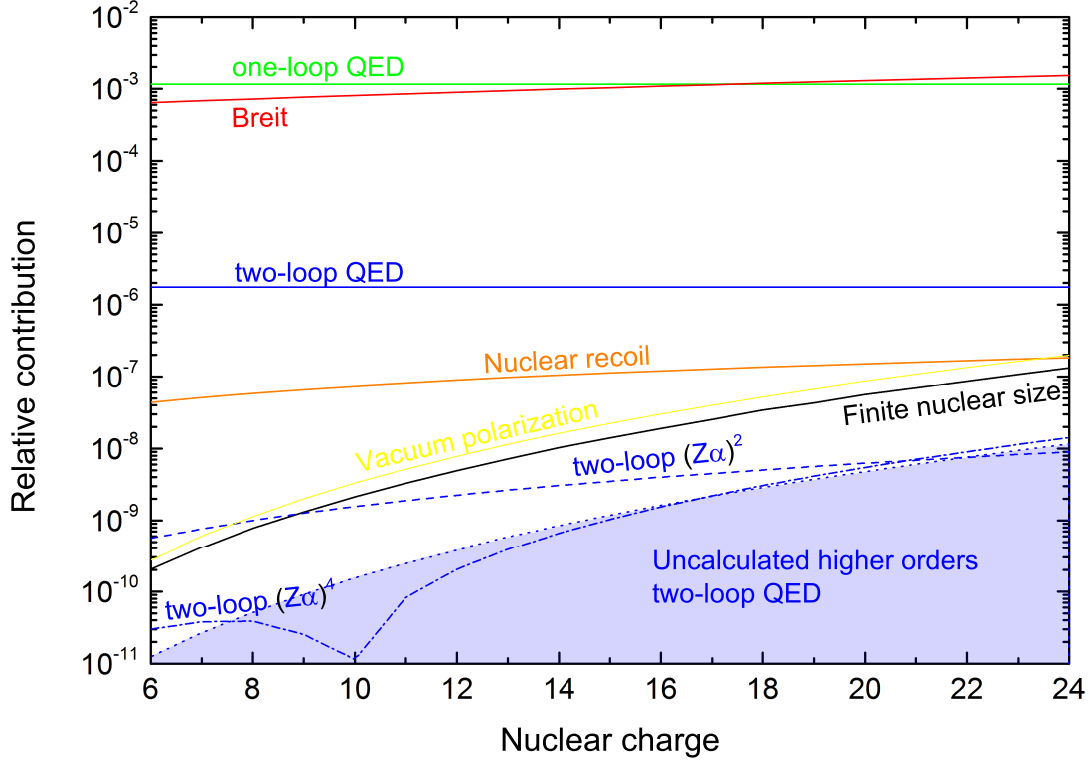
Figure 2.4: Contributions to the g-factor of the last electron in a hydrogenlike ion. The shaded area represents the current theoretical precision limit due to uncalculated higher order terms of the two loop BS-QED [27].

Contribution		Value
Dirac value		1.993 023 571 6
Finite nuclear size		0.000 000 020 5
One-loop QED	$(Z\alpha)^0$	0.002 322 819 5
	$(Z\alpha)^2$	0.000 004 040 7
	$(Z\alpha)^4$	0.000 001 244 6
	h.o. SE	0.000 000 542 8(3)
	h.o. VP-EL	0.000 000 032 6
	h.o. VP-ML	0.000 000 002 5
Two-loop QED	$(Z\alpha)^0$	-0.000 003 515 1
	$(Z\alpha)^2$	-0.000 000 006 1
	$(Z\alpha)^4$	-0.000 000 001 3
	h.o.	0.000 000 000 0(17)
	Recoil m_e/m_{ion}	0.000 000 206 1(1)
	rad-rec	-0.000 000 000 2
	h.o.	-0.000 000 000 1
Total		1.995 348 958 0(17)

Table 2.1: Summary of the contributions to the g-factor of $^{28}\text{Si}^{13+}$ [12].

3. Penning-trap spectrometry

The aim of the experiment is the ultra-accurate determination of the g-factor of the bound electron in hydrogenlike $^{28}\mathrm{Si}^{13+}$. The core requisite for such a measurement is a sufficiently long observation time while the ion under investigation is kept in an extremely well-controlled environment. Furthermore the measurement of the spin-precession frequency calls for a homogeneous magnetic field. The Penning trap constitutes a formidable tool for providing these conditions while simultaneously allowing the non-destructive detection of single ions. This chapter addresses the Penning trap as a measurement tool and introduces the techniques necessary for the g-factor determination.

3.1   The ideal Penning trap

In order to trap a charged particle in the charge-free space, electromagnetic fields have proved their worth. However, pure electrostatic fields cannot provide point-shaped confinement in all three spatial dimensions in charge-free space as can be seen from the Laplace equation. Point-shaped confinement demands the Hessian matrix of the electrostatic energy of the particle be locally positive definite, posing the necessary requirement:

$$\mathrm{Tr}\left(\mathrm{Hess}\big(\Phi(\mathbf{x})\mathrm{q}\big)\right) = \Delta\Phi\mathrm{q} > 0. \tag{3.1}$$

This is in obvious contradiction to the Laplace equation, demanding

$$\Delta\Phi = 0. \tag{3.2}$$

The combination of the homogeneous magnetic field (which is anyway necessary for the Zeeman-splitting in the context of a g-factor experiment, see chapter 3.5) with a quadrupolar electrostatic field of suitable strength, however, creates a strong confinement for charged particles with arbitrary energy. This configuration is termed
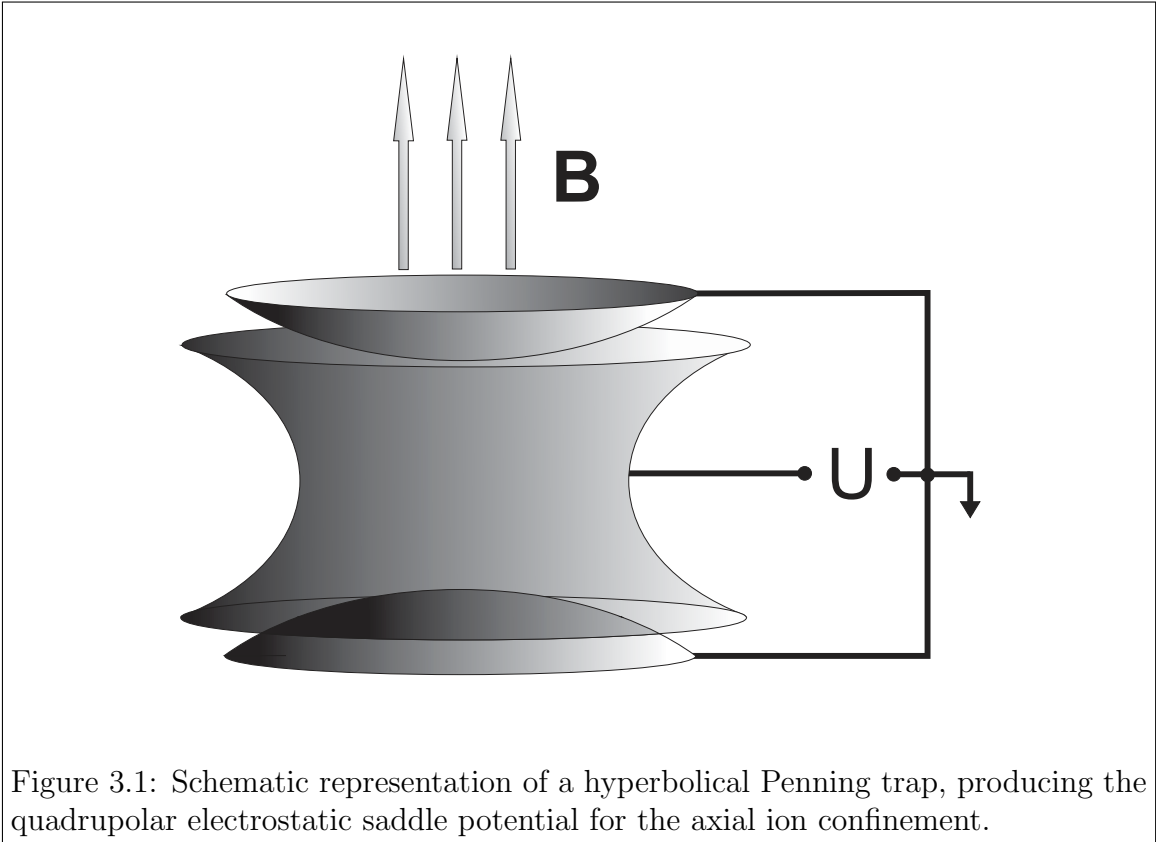
Figure 3.1: Schematic representation of a hyperbolical Penning trap, producing the quadrupolar electrostatic saddle potential for the axial ion confinement.

the ideal Penning trap [28, 29]. In reality, this configuration can be approximated very well. However the finite size of the experiment in combination with finite machining precision gives rise to deviations from the ideal field configuration, which have to be considered at the envisaged measurement accuracy. In the presence of a homogeneous magnetic field, chosen in z-direction without loss of generality,

$$\mathbf{B} = (0, 0, B_0) \tag{3.3}$$

a charged particle undergoes a helical eigenmotion around the magnetic field lines. However, the motion along the z-axis is unbound. For this reason, a quadrupolar electrostatic field[1] of suitable polarity

$$\mathbf{E} = C_2(x, y, -2z) \tag{3.4}$$

is superimposed, causing a bound harmonic eigenmotion along the magnetic field lines. Figure 3.1 shows a possible electrode configuration that produces this potential configuration. In the radial plane, the additional field alters the circular motion slightly, as the perpendicular electric and magnetic fields cause a slow drift in az-

---

[1]Note that the implicit definition of the C_n coefficients used in the following contracts both the length scale and the applied voltage.

imuthal direction. The resultant motion can be decomposed into two independent[2] harmonic oscillations. The drift results in a circular motion around the electrostatic trap center with the frequency ω_-, referred to as magnetron frequency, while the free cyclotron frequency becomes slightly modified and is denoted as ω_+, usually called modified cyclotron frequency. In the non-relativistic classical limit the equations of motion of an ion with mass m and charge q in an ideal Penning trap are [29]:

$$
\begin{aligned}
\ddot{x} &= \frac{q}{m}\left(C_2 x + B_0 \dot{y}\right) \\
\ddot{y} &= \frac{q}{m}\left(C_2 y - B_0 \dot{x}\right) \\
\ddot{z} &= -2\frac{q}{m}C_2 z.
\end{aligned}
\tag{3.5}
$$

For suitable voltages the coefficient C_2 is positive and this coupled system of differential equations can be solved, yielding the three eigenfrequencies as functions of the lowest-order field parameters:

$$
\omega_z = \sqrt{2\frac{q}{m}C_2}
\tag{3.6}
$$

$$
\omega_\pm = \frac{\omega_c}{2} \pm \frac{1}{2}\sqrt{\omega_c^2 - 2\omega_z^2},
\tag{3.7}
$$

where $\omega_c = q/mB_0$ denotes the free cyclotron frequency. In the ideal Penning trap the eigenfrequencies obey the following relations:

$$
\omega_c = \omega_+ + \omega_-
\tag{3.8}
$$

$$
\omega_z^2 = 2\omega_+\omega_-
\tag{3.9}
$$

$$
\omega_c^2 = \omega_+^2 + \omega_z^2 + \omega_-^2.
\tag{3.10}
$$

While (3.8) and (3.9) lose validity in the presence of trap imperfections, equation (3.10), the so-called invariance theorem [29, 30], stays valid under certain deviations from the ideal Penning trap, as will be discussed in chapter 3.2.5. In order to prevent the repulsive radial electrostatic field from making the ion trajectories unstable, the axial frequency has to be chosen sufficiently low:

$$
\omega_z \leq \frac{\omega_c}{\sqrt{2}}.
\tag{3.11}
$$

The typical field parameters then imply the following important hierarchy for the frequencies:

$$
\omega_c > \omega_+ \gg \omega_z \gg \omega_-.
\tag{3.12}
$$

For the Penning trap used in this experiment typical parameters for a $^{28}\mathrm{Si}^{13+}$ ion stored at 7.5 V and 3.76 T are listed in table 3.1:

---

[2]Independent here means that the energy and phase of one mode does not affect the other. This is only true in the ideal and uncoupled trap. Already special relativity leads to a dependence of the frequencies from the energy in the other modes.

Figure 3.2: Electrostatic potential in the radial plane including an exemplary particle trajectory, projected to the x-y plane. For details see text.
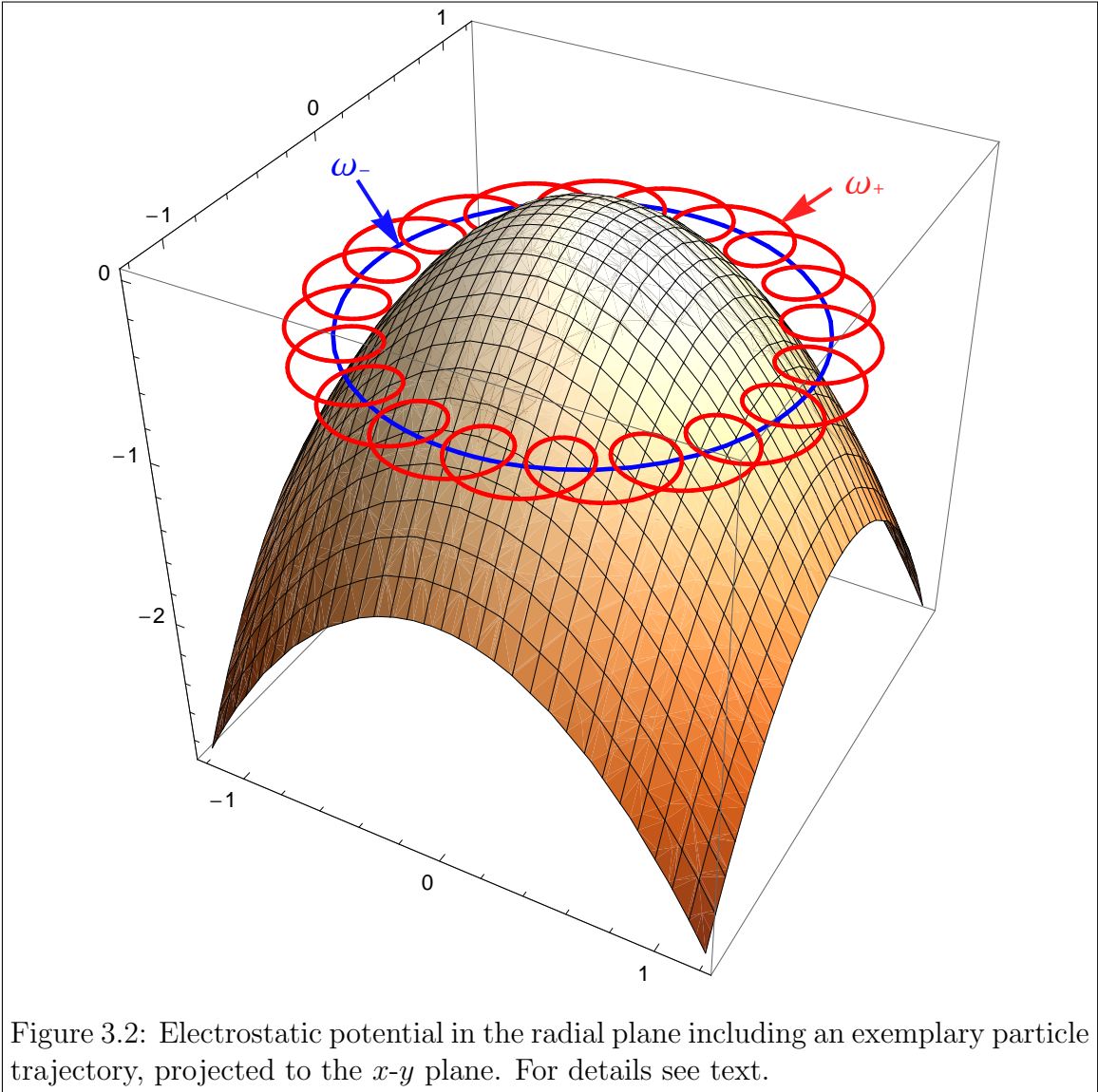
Frequency (Hz)	Energy (meV)	Amplitude (µm)	Temperature (K)
$\nu_+ = 26857410$	6.6	1.2	76
$\nu_z = 704700$	0.17	7.8	2
$\nu_- = 9251$	-0.002	1.2	0.026

Table 3.1: Typical parameters for the eigenmodes of a $^{28}\text{Si}^{13+}$ ion stored in the precision trap (PT) at 7.5 V and 3.76 T.

3.2   The real cylindrical Penning trap

The implementation of a Penning trap with finite-sized electrode structures entails an inherent deviation from the ideal potential distribution. Furthermore, the prepara-

tion of a perfectly homogeneous magnetic field is not possible. It is thus an important challenge to develop a trapping system, providing a nearly ideal field configuration. Simultaneously, the implications of the remaining imperfections have to be well understood. The inherent cylindrical symmetry of the quadrupolar field calls for a rotationally symmetric electrode configuration. The obvious solution is a hyperbolically shaped electrode system, resembling the equipotential surfaces of the ideal field (see figure 3.1). However, there are a number of drawbacks in this configuration. The setup used in this work is composed of a stack of three cylindrical traps, called Creation Trap (CT), used for the charge breeding of ions, Precision Trap (PT), where the high-precision measurements of the eigenfrequencies are done, and Analysis Trap (AT), which uses a magnetic bottle for the detection of the spin state. The AT and PT are geometrically identical 5-pole traps. In the following, the properties of this trap type will therefore be discussed.
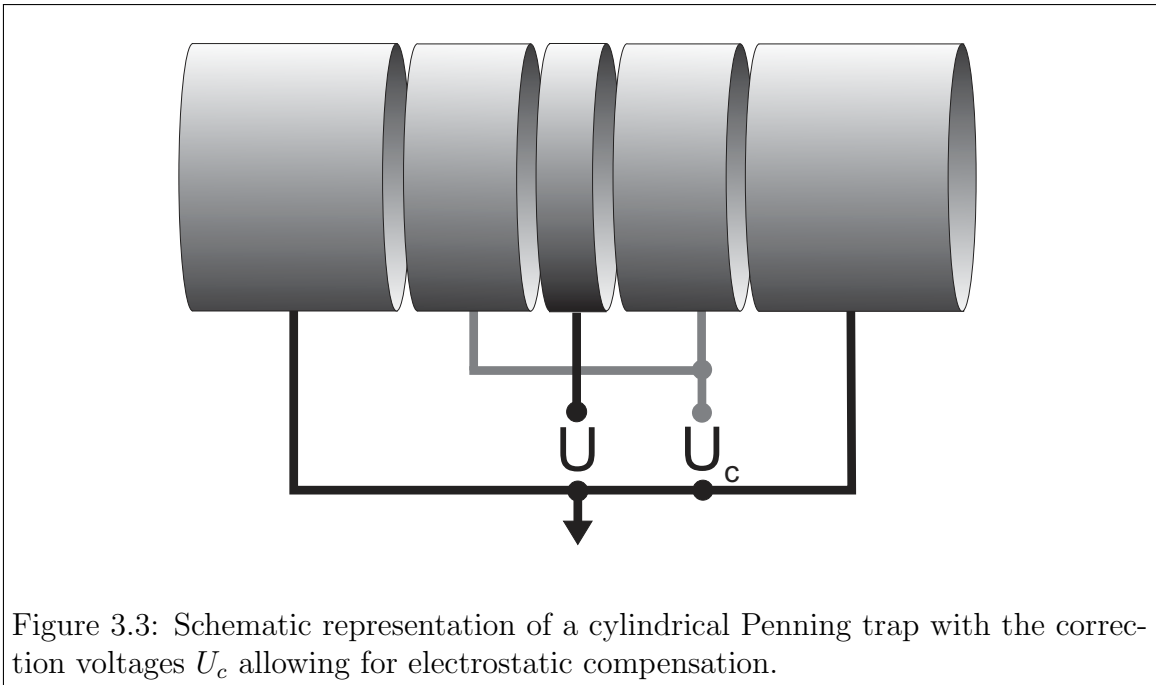
Figure 3.3: Schematic representation of a cylindrical Penning trap with the correction voltages U_c allowing for electrostatic compensation.

3.2.1 The anharmonic electrostatic potential

The necessity to introduce ions from outside the trap demands additional holes in the hyperbolical electrodes and the precision manufacturing and alignment of a stack of hyperbolical traps is not straightforward. As a simple solution, G. Gabrielse has proposed the compensated 5-pole cylindrical Penning trap [31]. This configuration consists of five cylinders with identical inner diameter but different lengths, providing an inherently cylindrical symmetric and mirror symmetric potential. This allows the expression of the potential as a Legendre series:

$$\Phi(r,\theta) = \sum_{k\,\text{even}} C_k r^k P_k(\cos\theta). \tag{3.13}$$

3.2.1.1 Compensation of an orthogonal cylindrical trap

Due to the mirror symmetry, all odd terms vanish, but in general there are undesired terms with $k > 2$. For small motional amplitudes obviously the most important non-trivial anharmonic contribution is the C_4 term. Just as any field configuration with $k > 2$ the quartic potential exhibits a highly undesirable dependence of the frequency on the ion radius. Since the radius cannot be as accurately measured as the frequency, it is of utmost importance to minimize the C_4 term to avoid systematic frequency shifts. A rigorous calculation of the resulting frequency corrections was carried out by Brown and Gabrielse [29]. The result can be depicted in matrix form:

$$
\begin{pmatrix} \Delta\omega_+/\omega_+ \\ \Delta\omega_z/\omega_z \\ \Delta\omega_-/\omega_- \\ \Delta\omega_L/\omega_L \end{pmatrix} = \frac{6C_4}{C_2^2} \begin{pmatrix} \frac{1}{4}(\omega_z/\omega_+)^4 & -\frac{1}{2}(\omega_z/\omega_+)^2 & -(\omega_z/\omega_+)^2 \\ -\frac{1}{2}(\omega_z/\omega_+)^2 & \frac{1}{4} & 1 \\ -(\omega_z/\omega_+)^2 & 1 & 1 \\ 0 & 0 & 0 \end{pmatrix} \cdot \begin{pmatrix} E_+ \\ E_z \\ E_- \end{pmatrix}. \quad (3.14)
$$

The last line of the matrix describes the shift of the electron spin precession (Larmor) frequency, which does not depend on the electric field, for completeness. Considering that the use of five electrodes allows the application of two independent voltages, U_0 and U_c to the ring- and correction electrode, respectively (see figure 3.3), it is obvious that in general it will be possible to choose a voltage $U_c \equiv T\, U_0$ such that $C_4 = 0$. The dimensionless quantity T is usually called tuning ratio. In addition, it is highly desirable to have $C_6 z_0^2 \ll C_4$ for typical axial amplitudes z_0 (listed in table 3.1) in order to minimize systematic frequency shifts. Moreover, in the process of trap optimization it is very convenient to make $C_2 = C_2(U_0)$ independent of the correction voltage U_c and thus the tuning ratio T. Using the Greens function of conducting cylinders, it is possible to calculate the coefficients C_k for a given set of electrode dimensions. After freely choosing the trap radius, it is generally possible to make $C_4 = C_6 = 0$ and simultaneously $\partial C_2/\partial U_c = 0$ by adjusting the ring- and correction electrode lengths and the tuning ratio T, representing three degrees of freedom. The resulting trap configuration is called compensated (C_4 and C_6 are compensated by the correction potential) and orthogonal (the field parameters C_2 and $C_{k>2}$ can be addressed independently) [31]. Close to the optimal tuning ratio, the higher order perturbation coefficients can then be approximated as:

$$
C_{4,6} = (T - T_{\text{opt}}) \cdot D_{4,6}, \quad (3.15)
$$

where $D_{4,6}$ characterize the dependence of the potential contributions $C_{4,6}$ from the mistuning of the tuning ratio and can be obtained numerically. For small ion radii, the resulting potential is not distinguishable from the ideal harmonic potential, providing a basis for high-precision measurements. However, the value of field parameters with $k > 6$ cannot be simultaneously minimized, limiting the usable trap volume considerably. If larger radii have to be used, a hyperbolical trap might be more advantageous.

3.2.2 The inhomogeneous magnetic field

In the ideal Penning trap, the magnetic field is considered to be perfectly homogeneous. In reality, there will generally be deviations from this idealized configuration even in well-shimmed[3] magnetic fields due to the susceptibility of the trap system and ultimately by virtue of the displacement current in the electrostatic field of the trap causing motional magnetic fields [32].
The influence of the radial field component is strongly suppressed by the large axial field component and can thus be neglected in most cases. However, the dependence of the axial magnetic field on the axial and radial coordinates can cause significant systematic frequency shifts. Since the trapped particle is rotating around the trap axis it will in the adiabatic limit[4] generally experience an effectively cylindrically symmetric magnetic field. The effective magnetic field can thus be decomposed into a Legendre series in direct analogy to the electric field. The resulting field coefficients B_n will generally all have secular effects on the ion frequency that have to be considered for finite mode energies.

3.2.2.1 The magnetic bottle

The lowest order correction, apart from the non-secular linear gradient (B_1), is the quadratic component B_2, usually termed the magnetic bottle. This inhomogeneity modifies the eigenfrequencies in all traps, the difference is purely quantitative. However, the strength of the magnetic bottle in the AT, provided by a ferromagnetic ring electrode, is about a factor of $20\,000$ larger than in the PT, where the dominant contribution to the quadratic component is the tail of the magnetic field of the AT ring electrode.
From the Legendre series of the magnetic field, it follows that in second order

$$\Delta B_z(\rho, z) = B_2 \left(z^2 - \frac{\rho^2}{2} \right).$$
(3.16)

Just as in the electrostatic case, the second order contribution creates a saddle point[5]. This means for positive B_2, the ion will see an increasing magnetic field with increasing axial energy. Averaged over one axial oscillation period, the additional magnetic field will be (for negligible radial energy):

$$\Delta B = B_2 z_{\text{rms}}^2 = B_2 \frac{z_0^2}{2} = \frac{B_2}{m\omega_z^2} E_z.$$
(3.17)

---

[3]Superconducting magnets typically allow to tune the magnetic field to near-perfect homogeneity using so-called shim-coils in different field configurations to compensate the field errors of the main field coil.

[4]Adiabatic here means the variations of the motional amplitudes are slow compared to all eigenfrequencies.

[5]Note, however, that this depicts the magnetic field, unlike the corresponding Legendre series of equation (3.13), which represents the electric potential.

This translates into a relative shift for the modified cyclotron frequency:

$$\frac{\Delta\omega_+}{\omega_+} \simeq \frac{B_2}{B_0}\frac{1}{m\omega_z^2}E_z \qquad (3.18)$$

On the other hand, when increasing the cyclotron radius, the magnetic moment resulting from the ion current $I = q\omega_+/(2\pi)$

$$\mu_z^{\mathrm{cycl}} = -I\pi\rho_+^2 = -\frac{\omega_+ q\rho_+^2}{2} = -\frac{qE_+}{m\omega_+} \qquad (3.19)$$

will feel an additional magnetic pseudo-potential in the magnetic bottle:

$$\Phi_{\mathrm{mag}} \equiv -\mu_z^{\mathrm{cycl}}\frac{B}{q} = -\frac{\mu_z^{cycl}B_2}{q}z^2 = \frac{B_2}{m\omega_+}E_+z^2 \qquad (3.20)$$

and thus experiences an additional axial force:

$$F_z = -q\,\partial_z\Phi_{mag} = -\frac{2qB_2}{m\omega_+}E_+z. \qquad (3.21)$$

This additional force will add to the electrostatic force from the trapping potential and alter the axial frequency:

$$\bar{\omega}_z = \sqrt{\omega_z^2 - \frac{F_z}{mz}}. \qquad (3.22)$$

The axial frequency shift thus is:

$$\Delta\omega_z \simeq \frac{B_2}{B_0}\frac{1}{m\omega_z}E_+. \qquad (3.23)$$

This very important result opens the possibility to measure the energy in the cyclotron mode in terms of a shift in the axial frequency. At the same time the cyclotron frequency will shift as a result of the lower magnetic field at higher cyclotron radii:

$$\frac{\Delta\omega_+}{\omega_+} \simeq \frac{\Delta B}{B} = -\frac{B_2}{2B_0}\rho_+^2 = -\frac{B_2}{B_0}\frac{1}{m\omega_+^2}E_+. \qquad (3.24)$$

From equations (3.23) and (3.24) it becomes obvious that

$$\frac{\Delta\omega_z}{\omega_z} = -\left(\frac{\omega_+}{\omega_z}\right)^2\frac{\Delta\omega_+}{\omega_+}. \qquad (3.25)$$

Similarly, there exist equivalent relations for the dependence of the remaining eigen-frequencies on the energy in all modes. Again, Brown and Gabrielse [29] derived the result in matrix form:

$$
\begin{pmatrix} \Delta\omega_+/\omega_+ \\ \Delta\omega_z/\omega_z \\ \Delta\omega_-/\omega_- \\ \Delta\omega_L/\omega_L \end{pmatrix} = \frac{B_2}{B_0} \frac{1}{m\omega_z^2} \begin{pmatrix} -(\omega_z/\omega_+)^2 & 1 & 2 \\ 1 & 0 & -1 \\ 2 & -1 & -2 \\ -(\omega_z/\omega_+)^2 & 1 & 2 \end{pmatrix} \cdot \begin{pmatrix} E_+ \\ E_z \\ E_- \end{pmatrix}.
\tag{3.26}
$$

Note that the relative shifts of the modified cyclotron and Larmor frequency are identical for the magnetic bottle, an important result that will be helpful when measuring the frequency ratio ω_L/ω_c.

3.2.2.2 The continuous Stern-Gerlach effect and non-destructive spin-state detection

The same effect that translates the cyclotron mode energy into a shift of the axial frequency can be used to detect the spin state of the single electron bound to the trapped ion non-destructively. The corresponding magnetic moment couples to the magnetic bottle and causes a frequency shift that is related to the spin direction. This is in analogy to the splitting of spin-carrying atomic beams in magnetic gradients discovered by O. Stern and W. Gerlach in 1922 [33] and was first introduced for spin state detection in Penning traps by Dehmelt [5].

The complete magnetic moment in axial direction can be calculated from the sum of the magnetic moments of the spin and the cyclotron motion[6]:

$$
\mu_z = \mu_z^{\text{cycl}} + \mu_z^{\text{spin}} = -\frac{qE_+}{m\omega_+} \mp \frac{g_s e\hbar}{2m_e},
\tag{3.27}
$$

where e is the elementary charge and m_e denotes the electron mass. Combining the dependence of the axial frequency on the cyclotron energy and the spin state yields:

$$
\Delta\omega_z \simeq \frac{\mu_z \nabla \mathbf{B}}{2mz} = \frac{B_2}{m\omega_z} \left(\frac{E_+}{B_0} \pm \frac{g_s e\hbar}{2m_e} \right).
\tag{3.28}
$$

It is evident that there is an axial frequency difference for the two possible spin orientations. However, the tiny difference that amounts to 240 mHz for a $^{28}\text{Si}^{13+}$ ion within the axial frequency of several hundred kHz in our Analysis Trap will be only detectable if the cyclotron energy E_+ is either extremely small ($\ll 2\,\text{K}$) or at least sufficiently stable. Simultaneously, the ring voltage fluctuations between consecutive measurements have to be considerably smaller than

$$
\left(\frac{\delta U_{\text{rms}}}{U} \right) \ll 2 \left(\frac{\Delta\omega_z}{\omega_z} \right) \simeq 10^{-6}.
\tag{3.29}
$$

This imposes a challenge for the design of a suitable voltage source.

---

[6]The tiny magnetic moment caused by the magnetron motion is neglected here.

3.2.2.3 Other secular magnetic field inhomogeneities

All field components $B_{k>2}$ lead to frequency shifts with nonlinear energy dependence. However, considering that for typical energies in the precision trap the shift from B_2 is barely visible, it is not necessary to account for higher field components during the precision measurements with the measurement methods employed in this thesis. An estimate can be derived by calculating the magnetic field on typical cyclotron radii:

$$\frac{\Delta\nu_c}{\nu_c} \simeq \frac{3B_4}{8B_0}\rho^4 \ll 10^{-13}. \tag{3.30}$$

In the Analysis Trap, the B_4 coefficient is large as a result of the ferromagnetic ring, but there is no need to perform absolute frequency measurements in this trap. However, there is a subtle consequence of this field component on the tuning ratio of the trapping potential [34]. Already the magnetic bottle alters the tuning ratio by adding a voltage-independent harmonic pseudo-potential. The quartic magnetic field component comprises a term that makes the magnetic pseudo-potential dependent on the cyclotron energy[7]. The quartic part of the combined magnetic and electric potential reads:

$$\Phi_4(z) \quad = -\mu_z^{cycl}\frac{B_4}{q}z^4 + D_4(T - T_{opt})z^4 \tag{3.31}$$

$$= \frac{B_4}{m\,\omega_+}E_+ z^4 + D_4(T - T_{opt})\,z^4. \tag{3.32}$$

Combining this expression and equation (3.19), the energy dependence of the optimal tuning ratio T'_{opt} can be deduced:

$$T'_{opt} = T_0 - \frac{B_4}{D_4 m\omega_+}E_+. \tag{3.33}$$

In principle, this effect leads to tuning-ratio variations if the cyclotron energy is changed, potentially corrupting the spin-state detection by introducing energy coupling between the axial and radial modes. However, for the equilibrium temperatures achieved in the g-factor setup (see table 3.1), the variation of the tuning ratio is less than 1 ppm, which is negligible.

The analysis of the odd order perturbations of the magnetic field is slightly different since these do not have a direct secular effect on the ion frequencies. However, the radial magnetic moment causes a shift of the equilibrium position of the ion in axial direction:

$$0 = \partial_z\left(\Phi_{\mathrm{m}} + \Phi_{\mathrm{el}}\right) \rightarrow \Delta z \simeq -\frac{B_1}{2C_2 m\omega_+}E_+. \tag{3.34}$$

This leads to a energy dependent cyclotron frequency shift [34]:

$$\frac{\Delta\nu_+}{\nu_+} \simeq \frac{B_1\Delta z}{B_0} \simeq -\frac{1}{m\omega_z^2}\left(\frac{B_1}{B_0}\right)^2 E_+, \tag{3.35}$$

---

[7]All other contributions (magnetron and spin energy) are neglected here.

corresponding to $\Delta\nu_+/\nu_+ \simeq 2\,\mathrm{ppt/eV}\ E_+$ in the g-factor setup, which is small compared to the effect of the harmonic magnetic perturbation.

3.2.3 Relativistic corrections

Although the velocities of the ion, which is typically cooled to 4.2K, are extremely small compared to the speed of light, the precision attained in this experiment demands to account for relativistic corrections to the eigenfrequencies. In good approximation the corrections to the free cyclotron frequency are given by the mass increase predicted by special relativity due to the speed of the ion in the reduced cyclotron mode [29]:

$$\frac{\delta\omega_c}{\omega_c} = \frac{\bar{\omega}_c - \omega_c}{\omega_c} = \frac{\gamma - 1}{\gamma} \simeq \frac{E_+}{m_{\mathrm{ion}}\,c^2}, \tag{3.36}$$

where $\gamma = 1/\sqrt{1 - \beta^2} = 1/\sqrt{1 - (v/c)^2}$ denotes the Lorentz factor of special relativity. The effect of special relativity upon the spin precession frequency is more subtle. Since the spin precession, as opposed to the cyclotron rotation, occurs in the rest frame of the moving electron and ion, rather than in the laboratory frame, its value within the rotating reference frame of the ion[8] is subject to a Lorentz boost of the magnetic field:

$$\mathbf{B}' = \gamma\left(\mathbf{B} - \frac{\mathbf{v}}{c^2}\,\mathbf{v} \times \mathbf{E}(r_+, r_-, z)\right), \tag{3.37}$$

where $\mathbf{B}'$ denotes the magnetic field in the reference frame of the ion, which moves with the velocity $\mathbf{v}$ with respect to the laboratory system. Fortunately, the motional magnetic field induced by the electrostatic trapping field is negligible compared to the static magnetic field for typical conditions on the current level of accuracy[9]. The Larmor frequency in the rotating frame is thus:

$$\omega_L' = \frac{g_s}{2}\frac{e}{m_e}\gamma B_z = \gamma\omega_L. \tag{3.38}$$

When transforming back to the laboratory system, the time contraction cancels the effect of the magnetic field boost[10]. However, the rotation of the rest frame of the ion gives rise to a shift of the Larmor frequency due to the Thomas precession [35]:

$$\omega_L = \frac{1}{\gamma}\omega_L' + (1 - \gamma)\omega_c \simeq \omega_L^0 - \frac{\beta^2}{2}\omega_c. \tag{3.39}$$

For typical ion velocities of $\beta \leq 4\cdot 10^{-6}$, the correction due to the Thomas precession is negligible, in contrast to the free electron case, where the large cyclotron frequency

---

[8]Strictly speaking, the rest frame of the ion is not an inertial system in terms of special relativity, a fact that is accounted for later.

[9]A rough estimate can be done by assuming a thermalized magnetron motion and a cyclotron energy no larger than 3000 K. Under these assumptions the motional magnetic field for a $^{28}\mathrm{Si}^{13+}$ ion is smaller than $4 \cdot 10^{-14}$ T, which is negligible compared to the 3.76 T static field.

[10]Provided that the Lorentz factors of the electromagnetic field boost and the time dilation are exactly identical as assumed by special relativity.

of the electron increases this correction drastically [36].

Since the relativistic transformation of the Larmor- and cyclotron frequency are different, the measured frequency ratio will generally depend on the ion energy, especially of the cyclotron mode. This is a strong motivation for keeping the motional amplitudes during the measurement small.

3.2.4   Alignment errors

When placing the trap system in the magnetic field, great care is taken to align the electric trap axis with the magnetic field lines. However, a minimal tilt of typically $|\Theta| < 0.2°$ is generally inevitable. In order to calculate the corresponding frequency deviations, it is assumed that the particle trajectory will still be aligned to the strong magnetic field while the electrostatic field is tilted. Then the rotated electrostatic potential in the new axial direction (defined by the magnetic field lines) reads:

$$\Phi_z^{\text{tilt}}(z, \Theta) = C_2 \left(\cos (\Theta)^2 - \frac{\sin (\Theta)^2}{2} \right) z^2 \simeq C_2 z^2 \left(1 - \tfrac{3}{2}\Theta^2 \right). \tag{3.40}$$

Using equation (3.6), it is simple to calculate the axial frequency shift:

$$\Delta \omega_z \simeq -\tfrac{3}{4}\omega_z \Theta^2. \tag{3.41}$$

This relation can obviously be used to tune the alignment of the trap in situ, provided that the mechanical requirements are given. Similarly, it is possible to calculate the effect of the tilt on the other frequencies. Additionally, the finite machining precision of the trap and unwanted patch potentials at the surface of the electrodes can conspire to produce in first order an ellipticity of the otherwise harmonic potential. The systematic shifts arising from these mechanical imperfections in principle have the potential to cause systematic frequency shifts much larger than the precision aimed for in this experiment. Fortunately, the invariance theorem [29] discussed above helps to circumvent these issues.

3.2.5   The invariance theorem and its implications

Since all eigenfrequencies experience different shifts from the alignment, the final systematic error when determining the free cyclotron frequency depends on the relation used to translate the measured eigenfrequencies into the final measurement result. Brown and Gabrielse noticed that, when using equation (3.10), the frequency shifts arising from alignment errors and ellipticity cancel completely. This is illustrated by expressing the so-called invariance theorem [29] as:

$$\omega_c^2 = \bar{\omega}_+^2 + \bar{\omega}_z^2 + \bar{\omega}_-^2, \tag{3.42}$$

where the accented quantities are representing the measured frequencies, while the cyclotron frequency is the ideal free cyclotron frequency in absence of the electrostatic field. This paves the way for measuring the free cyclotron frequency in the

presence of a non-perfect electrostatic field to extremely high accuracy. Closer inspection reveals that even the magnetic bottle correction drops out when measuring the axial and cyclotron frequencies at the same cyclotron energy (e.g. simultaneously), while the magnetron frequency is measured at low energy.

3.3 Image-current detection

For a successful g-factor measurement, the eigenfrequencies have to be measured non-destructively and with high precision. These requirements can be met by the image-current detection method. To this end, the current induced by the oscillating charge of the stored ion in one of the electrodes is measured. For small amplitudes, the induced charge will depend linearly on the ion's deflection:

$$q^{\text{el}}(t) = \frac{q}{D} z(t). \tag{3.43}$$

Here, D denotes a typical length scale that relates the response of the trap system to an equivalent plate capacitor. The numerical value of D can be accurately calculated with the solution of the Laplace equation for the electrode set. With equation (3.43) it is possible to calculate the current:

$$I^{\text{el}}(t) = \dot{q}^{\text{el}}(t) = \frac{q}{D} \dot{z}(t) \qquad \rightarrow \qquad I^{el}_{rms,z} = \frac{q\omega_z}{D} z_{\text{rms}}. \tag{3.44}$$

When the ion is cooled to low energies around 4 K (see table 3.1), the current in our experiment amounts to $I^{\text{el}}_{\text{rms,z}} \simeq 7\,\text{fA}$. The measurement of such a tiny current calls for a transimpedance amplification with a large resistance at the axial frequency. This can be realized with a superconducting tank circuit with a high quality factor (Q), tuned to the ion's eigenfrequency. In resonance, this tank circuit forms a resistance $R = Q\,\omega\,L$, where L denotes the tank circuit's coil inductance. For ions of high axial energy, the voltage drop across the resonator is given by $U = Z(\omega)\,I^{el}$, and reaches values that are relatively simple to measure with solid-state electronic amplifiers (see chapter 4.3.3). However, the orthogonal part of the voltage appearing at the electrode has a retroactive effect on the ion, which experiences an effective drag force [29]

$$F^{\text{drag}}(t) = \frac{q^2\,\text{Re}(Z(\omega))}{D^2}\,\dot{z}(t) \equiv m\gamma\dot{z}(t), \tag{3.45}$$

giving rise to energy transfer from the hot ion to the colder electron plasma of the resonator. Since the electron plasma is coupled to the lattice, the resonator constitutes a heat bath where the ion's energy is dumped. In general, the temperature of the ion will exponentially approach the temperature of the resonator's electron plasma with a time constant[11]

$$\tau = \frac{m\,D^2}{q^2\,\text{Re}\,(Z(\omega))}. \tag{3.46}$$

---

[11]This time constant τ is typically referred to as cooling time constant.

In our system with $D = 7.38$ mm and $\mathrm{Re}(Z) = 6.8$ MΩ, we obtain $\tau \simeq 88$ ms for a single $^{28}\mathrm{Si}^{13+}$ ion. The final equilibrium temperature is typically similar to
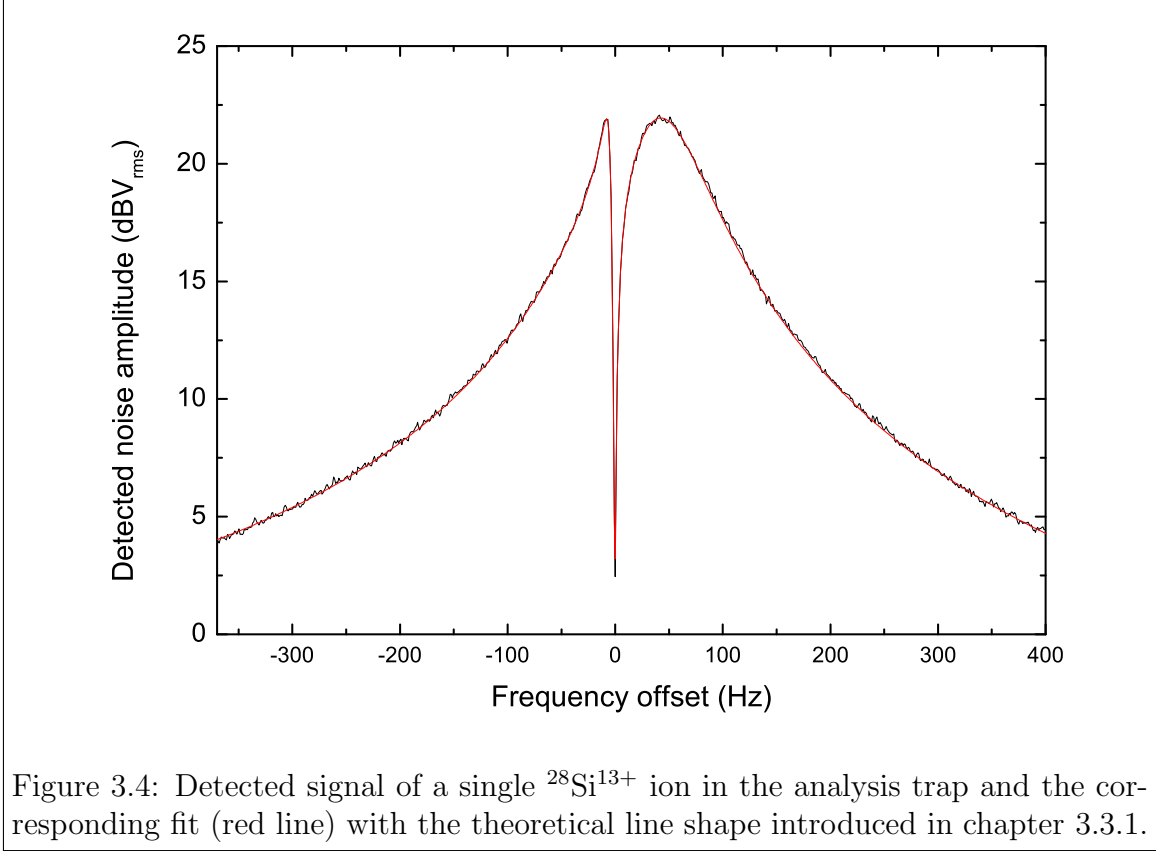
Figure 3.4: Detected signal of a single $^{28}\mathrm{Si}^{13+}$ ion in the analysis trap and the corresponding fit (red line) with the theoretical line shape introduced in chapter 3.3.1.

the lattice temperature, in the g-factor experiment 4.2 K, but can be altered with electronic feedback techniques as outlined in chapter 4.3.3.2.

When the ion is in thermal equilibrium with the tank circuit, the ion's signature on the resonator will adopt a fundamentally different shape. The ion is now driven and damped by the incoherent thermal noise of the resonator. The detected signal is not anymore dominated by the coherent peak signal of a hot ion, but resembles the thermal noise of the coupled system formed by the ion and the resonator (see figure 3.4).

Since there is virtually no energy sink for the ion but the resonator, it is evident that in equilibrium the voltage spectrum at the position of the ion has to feature a dip in the spectral power density, as any remaining signal would lead to excitation of the axial motion of the otherwise undamped ion. The ion's axial energy and phase will thus adjust until its induced signal cancels the thermal noise of the resonator at the axial frequency.

3.3.1   Signal line shape of the thermalized ion

This consideration opens the possibility to measure the ion's axial eigenfrequency at the lowest possible energy, which is very advantageous for precision experiments

because it decreases the influence of trap imperfections dramatically. In order to extract the eigenfrequency from the axial dip signal, the line shape has to be known analytically. The equations of motion (eom) of the trapped ion in contact with the tank circuit can be expressed as function of the voltage u_e at the electrode [37]:

$$\ddot{z} = -\omega_z^2 \, z + \frac{u_e \, q}{m \, D}. \tag{3.47}$$

By using equation (3.44) it is possible to express the eom in terms of the ion current:

$$u_e = m \frac{D^2}{q^2} \partial_t i + \frac{m\omega_z^2 D^2}{q^2} \int i \, \mathrm{d}t = L_{\mathrm{ion}} \, \partial_t i + \frac{1}{C_{\mathrm{ion}}} \int i \, \mathrm{d}t. \tag{3.48}$$

As expected this is the equation of motion of a linearly damped harmonic oscillator. By exploiting the obvious analogy to a damped electrical series resonator, substitutional parameters can be extracted:

$$
\begin{aligned}
C_{ion} &\equiv \frac{q^2}{mD^2\omega_z^2} \simeq 90 \cdot 10^{-21} \, \mathrm{F} \\
L_{ion} &\equiv m\frac{D^2}{q^2} \simeq 600 \, \mathrm{kH} \\
\omega_z^2 &\equiv \frac{1}{L_{ion} \, C_{ion}}.
\end{aligned}
\tag{3.49}
$$

Using this analogy, the Johnson noise voltage density at the electrode, u_e, can be calculated by determining the transfer function $K(\omega) \equiv \frac{u_e}{u_J}$ from the virtual noise generator u_J, representing the Johnson noise of the equivalent resistance of the tank circuit:

$$
\begin{aligned}
u_J &= \sqrt{4 \, k_B \, T \, R} \\
|u_e(\omega)| &= |u_n \cdot K(\omega)| \\
&= u_n \left| \frac{\omega\omega_R(\omega - \omega_z)(\omega + \omega_z)}{\omega\omega_R\omega_z^2(\imath - \frac{\gamma\omega}{\omega_R^2}) - \imath\omega^3\omega_R + Q(\omega - \omega_R)(\omega + \omega_R)(\omega - \omega_z)(\omega + \omega_z)} \right|.
\end{aligned}
\tag{3.50}
$$

Here, ω_R is the resonance frequency of the tank circuit. After correcting for the electronic noise contribution of the amplifier, u_{en}, and allowing for a slight frequency dependence of the detection system, the final line-shape function can be determined:

$$u_d(\omega) = A \cdot (1 + \kappa_{\mathrm{det}}(\omega - \omega_R)) \cdot \sqrt{u_e^2(\omega) + u_{en}^2(\omega)}, \tag{3.51}$$

where κ_{det} accounts for a possible frequency dependence of the detector's transfer function in first order. Figure 3.5 shows the equivalent circuit representation and the resulting line shape. In practice, the resonator parameters Q, R and ω_R as well as κ and u_{en} are determined independently and fixed during the fit procedure. The functional parameters of the fit are thus the ion frequency ω_z, the dip-width parameter $\gamma = 1/\tau$ and the amplification of the detection system, A.

If n identical ions are stored simultaneously, all previous considerations still hold in the limit of negligible direct coulomb interaction when substituting

$$q \to n \cdot q, \, m \to n \cdot m \qquad \Rightarrow \qquad \gamma \to n \cdot \gamma. \tag{3.52}$$

Since the width of the observed dip scales linearly with γ, the fitted value of γ can be used to determine the number of simultaneously stored ions.
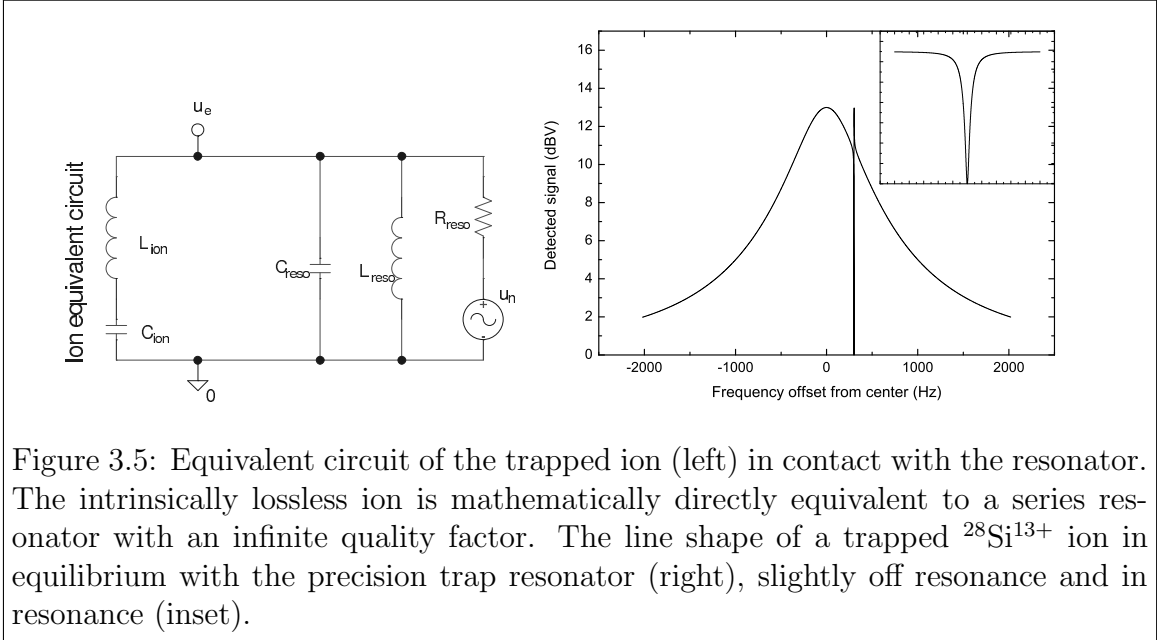
Figure 3.5: Equivalent circuit of the trapped ion (left) in contact with the resonator. The intrinsically lossless ion is mathematically directly equivalent to a series resonator with an infinite quality factor. The line shape of a trapped $^{28}\text{Si}^{13+}$ ion in equilibrium with the precision trap resonator (right), slightly off resonance and in resonance (inset).

3.4   Radiofrequency excitations

For high-precision Penning trap measurements it is of utmost importance that the ion's motional state can be extremely well controlled. The instrument of choice for this purpose is the radiofrequency excitation of the ion's motion and sidebands. The following chapter will outline the basic excitations in the monopolar- to quadrupolar field configuration and their respective resonances. Higher-order excitations have been considered in a different context [38, 39], but are not employed within this work.

3.4.1   Monopolar (parametric) excitation and squeezing

The monopolar or parametric excitation is the lowest order excitation possible in a Penning trap. As the name suggests, the parameter of the (axial) oscillation, C_2, is modulated:

$$\ddot{z} = -\bigl(\omega_z^2 + A_{\text{rf}}\cos(\omega_{\text{rf}}t + \phi_{\text{rf}})\bigr)z. \tag{3.53}$$

This modulation can be introduced by application of a radiofrequency drive to any electrode of the trap. The resulting driven system features a strong resonance at

the double eigenfrequency $2\,\omega_z$ and the respective even harmonics. Naively, the resonance can be understood by assuming a slowly varying axial amplitude:

$$z(t) \simeq z_0(t)\cos(\omega_z t + \phi_z). \tag{3.54}$$

In this approximation and further neglecting higher frequency non-secular terms, the equation of motion (3.53) reads:

$$\ddot{z} = -\omega_z^2 z - \tfrac{1}{2}A_{\mathrm{rf}}z_0(t)\cos\big((\omega_{\mathrm{rf}} - \omega_z)\,t + \phi_{\mathrm{rf}} - \phi_z\big). \tag{3.55}$$

By choosing $\omega_{\mathrm{rf}} = 2 \cdot \omega_z$, the requirement for resonant excitation can be read:

$$\phi_z = \tfrac{1}{2}(\phi_{\mathrm{rf}} + \tfrac{\pi}{2}). \tag{3.56}$$

As expected from symmetry considerations, this condition can be met by two distinct values of ϕ_z, separated by 180°. This symmetry can lead to bifurcation and chaotic behavior. It can be exploited for measuring the axial phase in multiples of π for arbitrarily small amplitudes that are far below the detection limit of the image-current detection. The excited motion will lock with the phase closer to its original phase before excitation.

If the ion is driven to sufficiently large amplitudes such that the quartic potential contribution $(C_4 z^4)$ becomes significant while being in contact with the resonator, the trapped ion is a close-to-ideal representation of the Duffing oscillator [40]. The measurement of the well-understood bi-stable resonance allows the determination of the higher-order field contributions [41].

If the ion is resonantly excited at $\omega_{\mathrm{rf}} = 2 \cdot \omega_z$ for a period τ_{rf} short compared to the axial cooling time constant, the resulting distribution can be described in terms of the in-phase and quadrature component of the motion [42]:

$$z(t, \tau_{\mathrm{rf}}) = C(\tau_{\mathrm{rf}}) \cdot \cos(\omega_z t) + S(\tau_{\mathrm{rf}}) \cdot \sin(\omega_z t), \tag{3.57}$$

where

$$C(\tau_{\mathrm{rf}}) = C_0 \cdot \mathrm{e}^{\frac{A_{\mathrm{rf}}\omega_z\tau_{\mathrm{rf}}}{4}} \tag{3.58}$$

$$S(\tau_{\mathrm{rf}}) = S_0 \cdot \mathrm{e}^{\frac{-A_{\mathrm{rf}}\omega_z\tau_{\mathrm{rf}}}{4}}. \tag{3.59}$$

After resistive cooling the initial distribution is circular in the C-S phasespace. The parametric excitation can now be used to squeeze the distribution to the needs of the experiment. For the advanced cyclotron frequency measurement technique PnA [13], developed within this work, which will be introduced in chapter 5.5, it is advantageous to squeeze the phase distribution at the expense of the amplitude distribution. Since the dominant energy dependent systematic shifts all scale linearly with the cyclotron energy and thus quadratically with the cyclotron radius (see equations (3.14) and (3.26)), the resulting mean cyclotron frequency shift after excitation can be calculated by averaging over the distribution of initial energies and phases. The possibility to squeeze the ion phase-space distribution was originally

introduced by V. Natarjan et al. [42]. However, the application to the phase definition is new to this work. Figure 3.6 shows the energy necessary for defining the cyclotron phase for a squeezed distribution and a circular distribution offset by a dipolar excitation. Obviously the parametric excitation is superior for all energies. For further information see chapter 5.5.
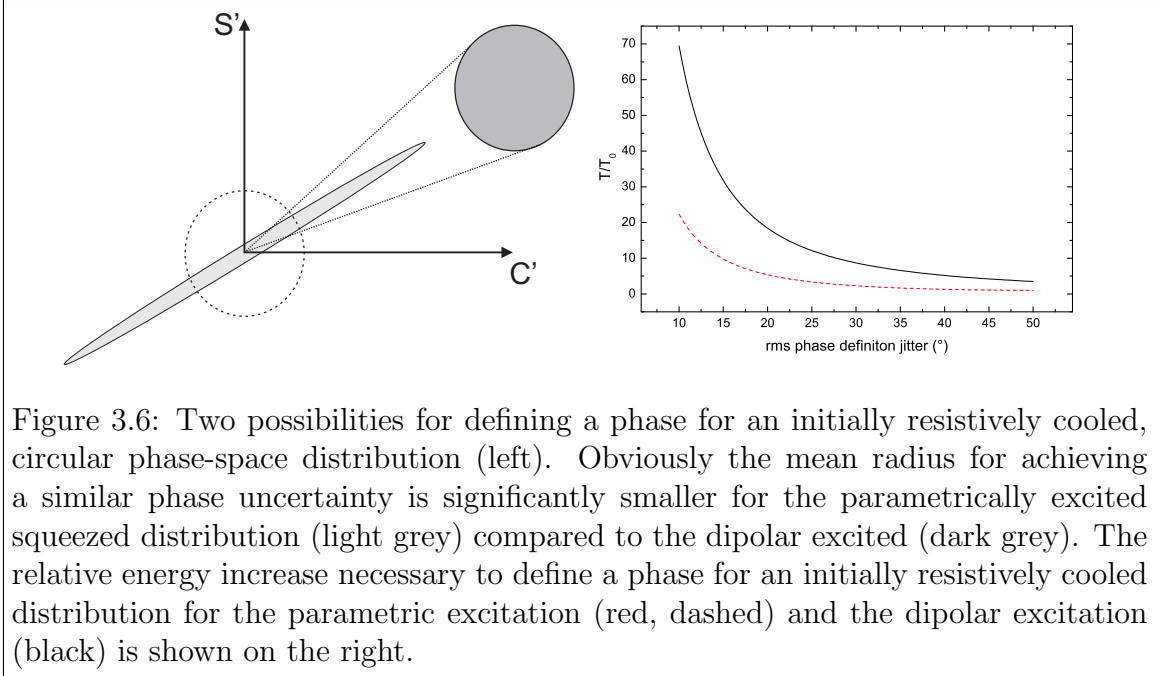
Figure 3.6: Two possibilities for defining a phase for an initially resistively cooled, circular phase-space distribution (left). Obviously the mean radius for achieving a similar phase uncertainty is significantly smaller for the parametrically excited squeezed distribution (light grey) compared to the dipolar excited (dark grey). The relative energy increase necessary to define a phase for an initially resistively cooled distribution for the parametric excitation (red, dashed) and the dipolar excitation (black) is shown on the right.

3.4.2   Dipolar excitation

The dipolar excitation, generated by a position independent radiofrequency force,

$$F_{\mathrm{dip,x,z}} = q\,A_{\mathrm{rf}}\,\cos(\omega_{\mathrm{rf}}t + \phi_{\mathrm{rf}}) \tag{3.60}$$

is very simple to treat in the quadrature phase-space, as it only produces a vectorial offset in the in-phase component, as shown in figure 3.6. This configuration can resonantly drive all eigenfrequencies of the ion in the trap, provided that a suitable electrode is used. For excitation of the axial motion the drive can be applied to the correction electrode or the endcap, for radial excitation a laterally split correction electrode is used. The dipolar excitation is used for defining a starting phase for the phase-sensitive measurement methods discussed in chapter 5.5 and for bringing the ion to deliberately large mode radii, enabling peak detection for mass spectra or for cleaning the trap from contaminating ions (see chapter 5.3).

3.4.3   Quadrupolar excitation and radiofrequency coupling

The quadrupole excitation is the most versatile of the excitation configurations used in the g-factor trap. It is the lowest order configuration that is able to couple two

otherwise independent modes and to transfer energy quanta between these. The application of the radiofrequency drive with amplitude A_rf to the split correction electrode produces a tilted field configuration in the x-z plane:

$$\mathbf{F}_\mathrm{quad} = q\, A_\mathrm{rf} \begin{pmatrix} z \\ 0 \\ x \end{pmatrix} \cos(\omega_\mathrm{rf} t + \phi_\mathrm{rf}). \tag{3.61}$$

The eom of the ideal Penning trap in the presence of a quadrupolar excitation read [43]:

$$\ddot{z} = -\omega_z^2 z + \mathrm{Re}\left(\tfrac{q}{m} A_\mathrm{rf}\, e^{\imath \omega_\mathrm{rf} t}\right) x \tag{3.62}$$

$$\ddot{u} = \frac{\omega_z^2}{2} u + \imath \omega_c \dot{u} + \mathrm{Re}\left(\tfrac{q}{m} A_\mathrm{rf}\, e^{\imath \omega_\mathrm{rf} t}\right) z, \tag{3.63}$$

where the abbreviation $u \equiv x + \imath y$ was used for simplicity. Inserting the obvious general solutions

$$z(t) = \mathrm{Re}\left(\zeta(t) e^{\imath \omega_z t}\right) \tag{3.64}$$

$$u(t) = \kappa_+(t) e^{\imath \omega_+ t} + \kappa_-(t) e^{\imath \omega_- t}, \tag{3.65}$$

allows to identify several frequency combinations, called sidebands, that can potentially show a secular effect on the respective eigenmotions because the effective force features a component at the respective eigenfrequency:

$$\omega_{1,2} = \omega_+ \pm \omega_z \tag{3.66}$$

$$\omega_{3,4} = \omega_z \pm \omega_-. \tag{3.67}$$

When choosing a radiofrequency close to any of these sidebands, the evolution of the slowly varying mode amplitudes can be extracted by neglecting the non-resonant higher-frequency terms that do not have any secular effect (rotating wave approximation). After some algebra the eom for the complex amplitudes can be identified:

$$\dot{\zeta} = \frac{1}{\omega_z} \begin{cases} \Gamma \kappa_+^* e^{\imath \delta t}, & \text{for } \omega_\mathrm{rf} = \omega_1 + \delta \\ -\Gamma^* \kappa_+ e^{-\imath \delta t}, & \text{for } \omega_\mathrm{rf} = \omega_2 + \delta \end{cases} \tag{3.68}$$

$$\dot{\kappa}_+ = \frac{1}{\omega_+ - \omega_-} \begin{cases} \Gamma\, \zeta^*\, e^{\imath \delta t}, & \text{for } \omega_\mathrm{rf} = \omega_1 + \delta \\ \Gamma\, \zeta\, e^{\imath \delta t}, & \text{for } \omega_\mathrm{rf} = \omega_2 + \delta \end{cases} \tag{3.69}$$

where * denotes complex conjugate and $\Gamma \equiv \frac{q A_\mathrm{rf}}{4m\imath}$. These eom can be combined in order to find the evolution of the motional amplitudes:

$$\ddot{\zeta} = -\Omega_{1,2}^2\, \zeta - \imath \delta \dot{\zeta} \tag{3.70}$$

$$\ddot{\kappa}_+ = -\Omega_{1,2}^2\, \kappa_+ + \imath \delta \dot{\kappa}_+, \tag{3.71}$$

where

$$\Omega_{1,2}^2 = \mp \frac{\Gamma\Gamma^*}{\omega_z(\omega_+ - \omega_-)}. \tag{3.72}$$

The possible detuning to the sidebands, δ, is taken into account by defining modified frequencies

$$\Omega_{1,2}^l = \frac{\sqrt{4\Omega_{1,2}^2 + \delta^2} - \delta}{2} \tag{3.73}$$

$$\Omega_{1,2}^r = \frac{\sqrt{4\Omega_{1,2}^2 + \delta^2} + \delta}{2}. \tag{3.74}$$

The final general solution for the complex amplitudes is of identical form for all sidebands:

$$\zeta(t) = \zeta_1\, e^{i\,\Omega_{1,2}^r\, t} + \zeta_2\, e^{-i\,\Omega_{1,2}^l\, t} \tag{3.75}$$

$$\kappa_+(t) = \kappa_1\, e^{i\,\Omega_{1,2}^r\, t} + \kappa_2\, e^{-i\,\Omega_{1,2}^l\, t}. \tag{3.76}$$

For the lower sideband ω_2 this solution describes a cyclic phase dependent modula-
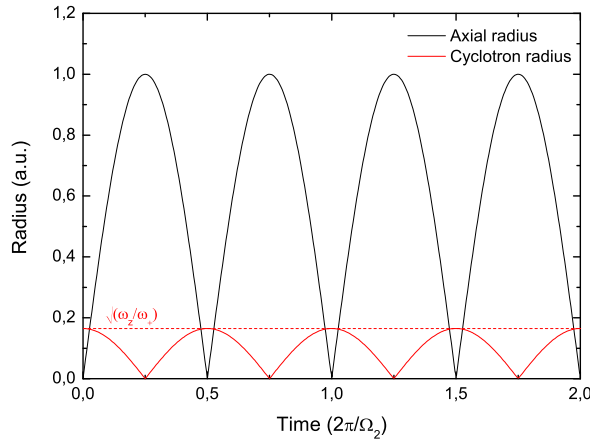
Figure 3.7: Exemplarily evolution of the mode radii with resonant excitation at the lower cyclotron sideband ω_2. The behavior is a classical analog to Rabi oscillations between the two coupled modes.

tion of the motional amplitudes due to exchange of the classical action $\oint p\mathrm{d}q$ between the two respective modes (see figure 3.7). On the other hand, the excitation of the upper cyclotron sideband ω_1 leads to an exponential growth of the motional amplitudes in both modes involved. In contrast to the dipolar excitation, now the excited mode phases depend strongly on the initial phases in all modes. This finding enabled the development of the advanced phase sensitive measurement method PnA, which will be described in chapter 5.5.

The lower sideband plays an important role in the measurement of the radial eigenfrequencies and in the cooling of these modes to the effective thermal equilibrium with the axial tank circuit. The effective evolution in dependence of the initial conditions $\kappa_0 \equiv \kappa_+(0)$ and $\zeta_0 \equiv \zeta(0)$ can now be found by inserting the general solution (3.76) into the eom:

$$\zeta_{1,2}^{\delta=0} = \frac{\zeta_0}{2} \pm \frac{\Gamma^*}{2\omega_z\Omega_2}\kappa_0 \tag{3.77}$$

$$\kappa_{1,2}^{\delta=0} = \frac{\kappa_0}{2} \pm \frac{\Gamma^*}{2(\omega_+ - \omega_-)\Omega_2}\zeta_0. \tag{3.78}$$

If the sideband is driven continuously, the time-averaged energy in the respective modes takes a constant ratio [29]:

$$\langle E_+ \rangle = \frac{\omega_+^2 + \omega_z^2}{\omega_z\omega_+} \langle E_z \rangle \simeq \frac{\omega_+}{\omega_z} \langle E_z \rangle. \tag{3.79}$$

The solution for the magnetron sidebands, $\omega_{3,4}$, is analogous, keeping in mind that the magnetron energy is negative due to the contribution of the electrostatic potential. As a result, the two sidebands change role compared to the cyclotron sidebands and the energy ratio becomes:

$$\langle E_- \rangle \simeq -\frac{\omega_-}{\omega_z} \langle E_z \rangle. \tag{3.80}$$

This close coupling of two eigenmodes is used extensively to selectively couple the otherwise undetected radial modes to the axial detector.

3.5 *g*-factor measurement principle

The hitherto presented techniques lay the basis for the high-precision measurement of the free cyclotron frequency ν_c^{ion} of the ion that can be used, together with the knowledge of the ion mass, as a probe for the magnetic field at the position of the bound electron. If simultaneously the Larmor frequency of the electron

$$\nu_L^{\text{e}} = \frac{g}{2}\nu_c^{\text{e}} = \frac{g}{2}\nu_c^{\text{ion}}\frac{e}{q_{\text{ion}}}\frac{m_{\text{ion}}}{m_{\text{e}}} \tag{3.81}$$

can be determined with comparable precision, the *g*-factor of the bound electron can be extracted:

$$g = 2\frac{\nu_L^{\text{e}}}{\nu_c^{\text{ion}}}\frac{q_{\text{ion}}}{e}\frac{m_{\text{e}}}{m_{\text{ion}}} \equiv \Gamma_0 \frac{q_{\text{ion}}}{e}\frac{m_{\text{e}}}{m_{\text{ion}}}, \tag{3.82}$$

with $\Gamma_0 \equiv \nu_L^{\text{e}}/\nu_c^{\text{ion}}$. The Larmor frequency again can be determined by probing the transition between the two discrete spin-states of the electron. The transition probability will be maximized for an excitation at the instantaneous Larmor frequency (under idealized conditions, compare chapter 6.1.4).

The measurement principle thus makes use of the possibility to determine the spin

state of the single bound electron unambiguously with the continuous Stern-Gerlach effect [9]: In the precision trap, where the energy dependent frequency shifts are minimal due to the extremely homogeneous magnetic field, a microwave excitation is applied close to the Larmor frequency and simultaneously the cyclotron frequency of the ion is measured. Afterwards, the ion is transported to the analysis trap, where the spin-state is determined and compared to its previous value. By repeating this process several hundred times and varying the microwave frequency around ν_L, the fractional spinflip rate can be plotted as function of the time-independent ratio $\Gamma_i = \frac{\nu_{\mathrm{mw}}}{\nu_c^{\mathrm{ion}}}$. Finally the g-factor can be determined with equation (3.82) after extracting the ratio Γ_0 from this resonance using a fit with a well-known line shape (see chapter 6.1.3.6). The experimental realization of the fundamental steps for this measurement algorithm

- Precision cyclotron frequency measurement

- Microwave excitation

- Adiabatic ion transport between AT and PT

- Spin state detection

are discussed in chapter 5.

4. The g-factor apparatus

*"The larger the island of knowledge, the longer
the shoreline of wonder."*

Ralph W. Sockman

The design of the g-factor apparatus is based on the apparatus built by Stefan Stahl, Wolfgang Quint, Nikolaus Hermanspahn, Manfred Tönges, Hans-Jürgen Kluge and Günter Werth for the first measurements of the g-factor of the bound electron in light ions [44]. The measurements with hydrogenlike carbon ($^{12}C^{5+}$) and later oxygen ($^{16}O^{7+}$),were carried out by N. Hermanspahn [45] and H. Häffner [10] and J. Verdú [11], respectively. The first direct determination of the g-factor of $^{12}C^{5+}$ was achieved by N. Hermanspahn in 1998.

After these measurements the apparatus was redesigned to meet the requirements of the creation of heavier highly charged ions. The additional dedicated miniature electron beam ion source and trap (EBIS/T) allows the creation of hydrogenlike ions up to calcium [46] and several adjustments of the trap layout allows for even smaller field errors. Large parts of the new setup, including the electronics have been developed in the framework of this thesis and provide the basis for significant precision improvements.

This chapter gives an introduction to the trap system and the associated electronics. Further details can be found in the Ph.D. thesis of Birgit Schabinger [46].

4.1   Overview

The apparatus consists of the following basic components:

- The superconducting 3.7 T magnet

- A combined liquid nitrogen and liquid helium cryostat used to cool the trap and electronics to 4 Kelvin

- A temperature stabilization system for the surrounding of the magnet, including the room temperature electronics

- A pressure stabilization system for the LHe dewars

- The triple cylindrical Penning trap setup with the EBIS/T

- Self-developed cryogenic electronics for the detection and manipulation of the ion motion

- Further electronics modules operated at room temperature, e.g. an ultra stable voltage source

- Miscellaneous function generators referenced to a rubidium atomic clock

- A dedicated FFT analyzer

- A microwave system supplying the W-band[1] excitation at the Larmor frequency of the electron

- A PC with LabView to control the measurement

Figure 4.1 shows a cut through the magnet with the experimental section opened. The superconducting magnet, manufactured by Oxford Instruments for NMR measurements, has a room-temperature bore with 127 mm diameter and provides the 3.764 Telsa homogenous magnetic field. Within its bore a second cryostat is inserted, featuring concentric heat radiation baffles at 77K, coupled to a liquid nitrogen bath and at 20K, in thermal contact with the evaporating liquid helium. The final temperature of the inner experimental setup (4K stage) is provided by the liquid helium bath. The only direct thermal contact from the 4K stage to room-temperature is through the constantan and steel wires for the electronics and a thin steel tube that allows the refilling of liquid helium and simultaneously serves for suspension of the setup. The isolation vacuum is maintained by the cryopumping effect, making electronically noisy pumps unnecessary during operation.

The precision electronics is located close to the traps within the magnetic field at 4K temperature. Since most commercial electronics fail under these conditions, specialized electronics was developed in the course of this thesis, including cryogenic transimpedance amplifiers with extremely low input related noise and matching superconducting resonators for the detection of single ions (see chapter 4.3.3). The massive closed metal enclosure of the experimental setup provided by the magnet and the cryostat in combination with a sophisticated electronic radiofrequency shielding concept allows the detection of the tiny signals of the stored ion and safeguards the ion from unwanted radiofrequency disturbances.

---

[1]The frequency band of millimeter waves, ranging from 75 GHz to 110 GHz.
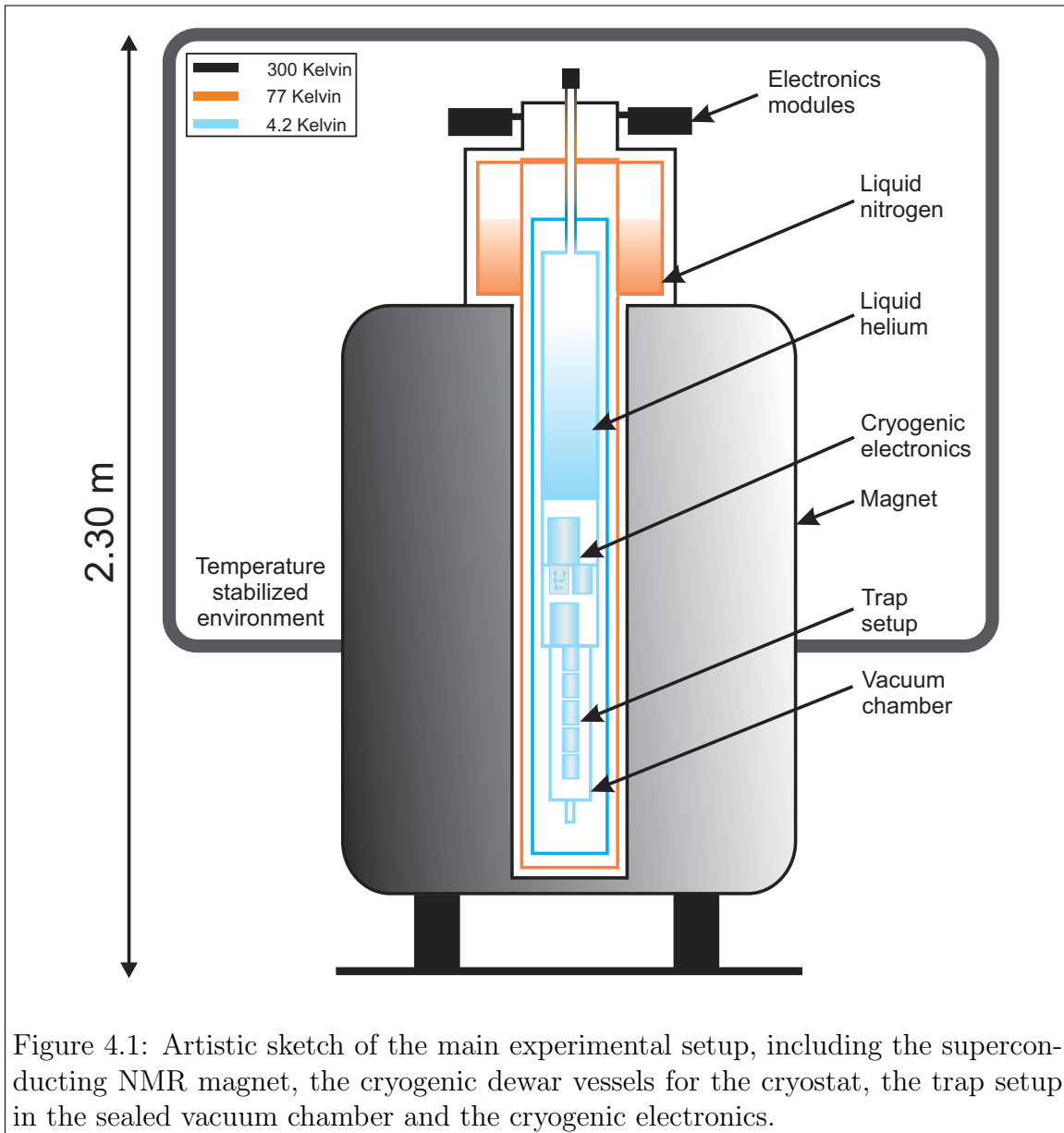
Figure 4.1: Artistic sketch of the main experimental setup, including the superconducting NMR magnet, the cryogenic dewar vessels for the cryostat, the trap setup in the sealed vacuum chamber and the cryogenic electronics.

The magnetic field strength of the magnet fixes the Larmor frequency of the electron to approximately 105 GHz, a frequency in the W-band microwave range. The excitation is produced externally by a commercial synthesizer and frequency multiplication system and transported to the trap with waveguides (see chapter 4.4). The trap setup is located in a vacuum chamber that separates the UHV[2] isolation vacuum, which is in contact with the room-temperature components, from the XHV[3] trapping vacuum. After pumping the vacuum chamber to UHV with a turbo molecular pump a thin OFHC[4] copper tube is pinched off, forming a cold-welded seal

---

[2]UHV: Ultra High Vacuum, 10^{-12} mbar $< p < 10^{-7}$ mbar.
[3]XHV: eXtremely High Vacuum, $p < 10^{-12}$ mbar.
[4]Oxygen Free High Conductivity

for the vacuum chamber. After cooling to 4K the rest gas freezes and adsorbs at the walls of the vacuum chamber which brings the vacuum into XHV. The vacuum was estimated (see chapter 5.3) to be $p < 10^{-17}$ mbar, which basically eliminates any disrupting interaction between the stored ion and the rest gas and allows the storage of the ion for virtually infinite time. In practice a storage time of 6 months was demonstrated for a highly charged hydrogenlike silicon ion, limited by technical problems rather than interactions with the rest gas [46].

The signals taken by the cryogenic detection system are further amplified at the room-temperature stage by self-developed low-noise amplifiers, quadrature mixed to lower frequencies and finally recorded by a dedicated FFT[5]. For ion manipulation a bunch of DDS[6] function generators (Agilent AG33250 and Stanford Research DS345) are synchronized with the 10 MHz signal of a rubidium atomic clock (Stanford Research FS725).

Finally a PC with National Instruments LabView is connected via GPIB[7], USB[8], RS232 and Ethernet to the devices and controls the experimental cycle.

4.2   The triple-trap setup
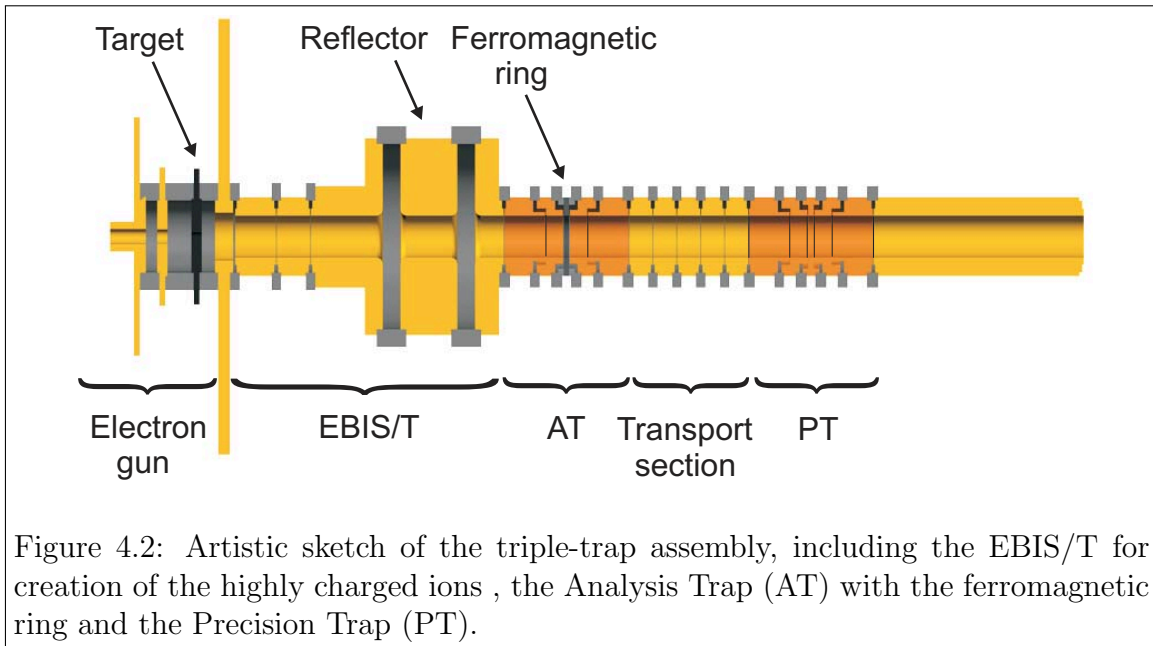
Figure 4.2: Artistic sketch of the triple-trap assembly, including the EBIS/T for creation of the highly charged ions , the Analysis Trap (AT) with the ferromagnetic ring and the Precision Trap (PT).

The heart of the apparatus is a setup of three Penning traps, the creation trap (CT), serving as EBIS/T for the creation of the highly charged ions, and the two geometrically identical traps for the detection of the spin-state (AT) and the precision frequency measurements (PT), completed by several electrodes dedicated to the transport of the ions between the traps. All electrodes except for the ring electrode

---

[5]Fast Fourier Transformer

[6]Direct Digital Synthesis

[7]General Purpose Interface Bus, IEEE-488

[8]Universal Serial Bus

of the AT are precision manufactured from OFHC copper and galvanically gold plated with a silver layer preventing the gold to form an alloy with the copper base material. The ring electrode of the AT, which provides the magnetic bottle field for spin-state detection, is made from gold plated nickel. Sapphire rings and balls provide both mechanical fixation and electric isolation. Undercuts in the electrodes inhibit electric field errors from charged isolators. The high voltage electrodes of the CT are isolated with MACOR rings.

With this electrode assembly it is possible to produce highly charged ions, to isolate a single ion of arbitrary species and charge-state and to measure the g-factor of the electron bound to this ion.

4.2.1 Creation trap

The Creation trap is used as an EBIS/T [46]. The electron beam emitted from the field emission point (FEP) of the electron gun is accelerated to energies up to 8 keV and follows the magnetic field lines until it is reflected from the high-voltage reflector. Since the electrons have lost fractions of their kinetic energy to radial motion and synchrotron radiation, the beam is trapped between the FEP and the reflector electrode, until sufficient space charge has built up to allow the fringe of the beam to impinge on the target anode. The electrons then evaporate atoms from the material of the target surface. These atoms freely travel through the CT volume, until they are hit by another electron of the beam, creating a singly charged positive ion. If this process happens in the trapping region of the CT, the ion is localized close to the center of the EBIT, where the electron beam can repeatedly impinge and successively remove the remaining electrons of the ion. If both the current density and the energy of the electron beam are sufficient, after some time the CT will be filled with a cloud of ions of different species and charge states. For the creation of hydrogenlike silicon the necessary charge-breeding time is on the order of 5 seconds. Heavier ions like calcium will need longer creation time and energy [47, 48, 46].

Since the electron beam is continuously supplying energy to the ion cloud, ions will be lost from the ensemble. The detailed analysis of the function of the EBIT, which goes beyond the scope of this thesis, shows that preferably light ions are boiled off in this process. This suggests that for the creation of higher charge states of heavy ions also light ions should be present in the target material.

The CT is an anharmonic three-pole trap that does not allow further selection of charge states. After the end of the creation process the high voltage is switched off and the unmodified cloud of ions is transported with adiabatic[9] changes of the potentials at the electrodes via the reflector to the precision trap.

4.2.2 Precision trap

After creation of the ions in the CT, the preparation of the ion to be measured is done in the PT. In contrast to the CT, the PT is a five-pole compensated and

---

[9]Adiabatic here refers to the rate of change of the potentials compared to the respective eigenfrequencies. If theses changes are sufficiently slow and additionally the trap is always kept at similar depth, the ion will experience negligible energy changes during the transport.

orthogonal trap (see figure 4.3), placed in the most homogeneous region of the super-conducting magnet. The potential of the PT can be analyzed with a finite elements
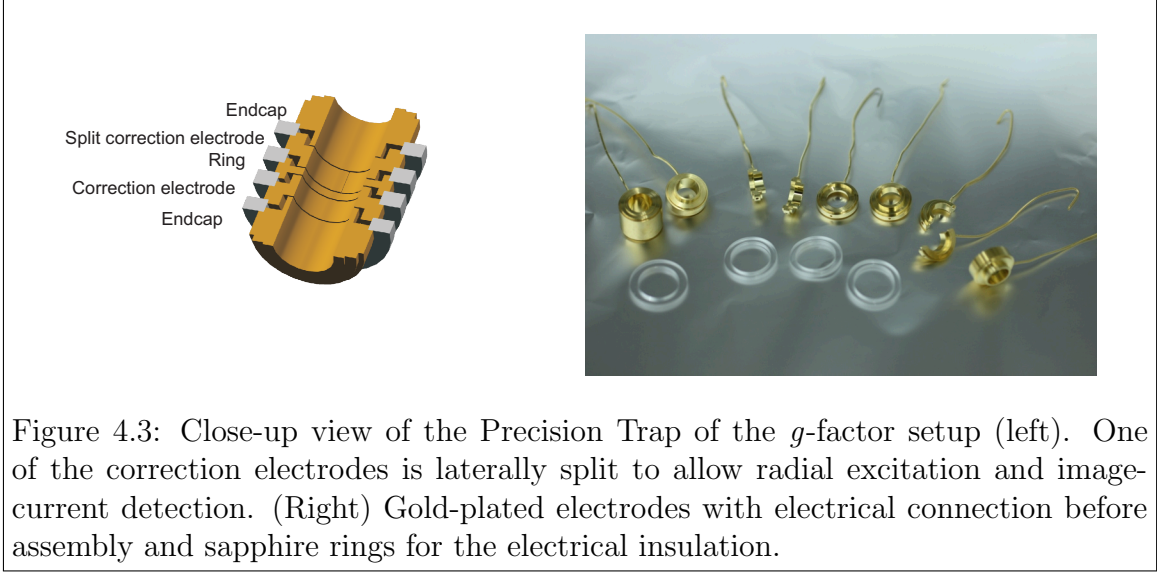
Figure 4.3: Close-up view of the Precision Trap of the g-factor setup (left). One of the correction electrodes is laterally split to allow radial excitation and image-current detection. (Right) Gold-plated electrodes with electrical connection before assembly and sapphire rings for the electrical insulation.

numerical solution of the Laplace equation with Dirichlet boundary conditions using e.g. COMSOL. By exploiting the superposition principle of the Laplace equation, the potential generated by any arbitrary electrode voltage set $(0,V_c,V,V_c,0)$ can be constructed from a linear combination of the orthogonal solutions with a unit voltage applied to the electrodes:

$$\Phi(z)_{(0,V_c,V,V_c,0)} = V\,\Phi(z)_{(0,0,1,0,0)} + V_c\,\Phi(z)_{(0,1,0,1,0)}. \tag{4.1}$$

From a polynomial fit to the hereby obtained potential distribution, the field coefficients C_n can be deduced. Figure 4.4 visualizes this process. The result shows compensation of the quartic potential contribution C_4 at the tuning ratio $T \simeq 0.86668$, but at this value C_6 does not vanish completely. The contribution of C_6 to the potential $\delta\Phi/\Phi = 6 \cdot 10^{-13}$ at typical thermal amplitudes (see table 3.1) is negligible. However, at higher energies as required for peak phase detection, the higher order contributions can cause unwanted phase jitter and poses a practical limit for the achievable phase resolution. An improved trap design should account for this limitation by altering the ring length such that C_4 and C_6 can be compensated simultaneously at the same tuning ratio.

4.2.2.1   Tuning-ratio optimization

In practice, the optimal tuning ratio is expected to deviate from the calculated value due to finite machining precision and charged dielectric patch potentials. It is therefore necessary to optimize the trap potential experimentally by applying suitable correction voltages. By applying a burst excitation at the magnetron frequency ω_- to a previously thermally cooled ion it is possible to set a defined magnetron energy. Equation (3.14) predicts a linear dependence of the subsequent axial frequency shift

Figure 4.4: (Left) The potential of the electrode set can be calculated from the weighted superposition of the orthogonal potentials obtained with COMSOL. For details see text. (Right) A fit to the potential allows the determination of the potential coefficients C_n.
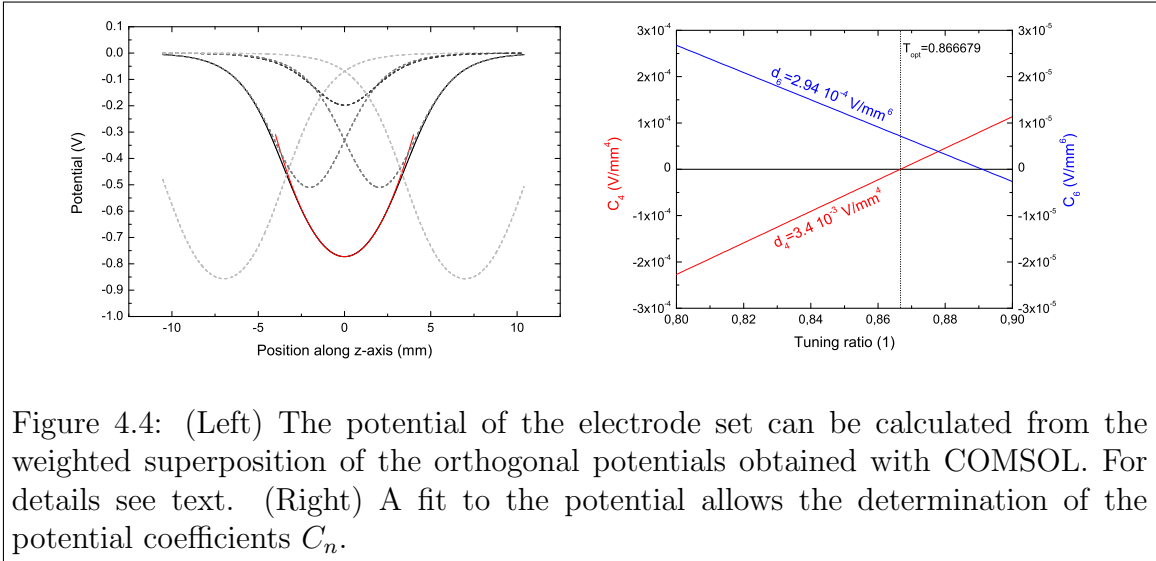
on the current value of C_4. Measuring the axial frequency shift between the cold and hot ion as function of the applied tuning ratio reveals the correct tuning ratio, where the frequency shift vanishes, provided that additional frequency shifts arising e.g. from the magnetic inhomogeneities are negligible. Figure 4.5 shows the result of such a measurement.

After optimization of the voltages applied to the correction electrodes, the resulting electrostatic potential is sufficiently harmonic for small amplitudes to not limit measuring accuracy even for the highest precisions achieved in this work.

4.2.2.2 Effective electrode distance

In chapter 3.3 it was assumed that the charge induced into the electrode set is similar to the one induced into an equivalent parallel plate capacitor with a plate distance of D. For the true electrode configuration this effective plate distance can be determined from the potential distribution of the electrodes, calculated with COMSOL. A parallel plate capacitor charged to a voltage V would generate an electric field at the position of the ion:

$$E_z^{\mathrm{pp}} = \frac{V}{D}. \tag{4.2}$$

If the image current is tapped at one of the correction electrodes, the effective electrode distance can be determined by extracting the electric field of the correction electrode at the position of the ion, E_z^{el}, from the numerical solution of the potential. In combination with equation (4.2) the value of D can be extracted:

$$D = \frac{V}{E_z^{\mathrm{el}}} = 7.38 \, \mathrm{mm}. \tag{4.3}$$
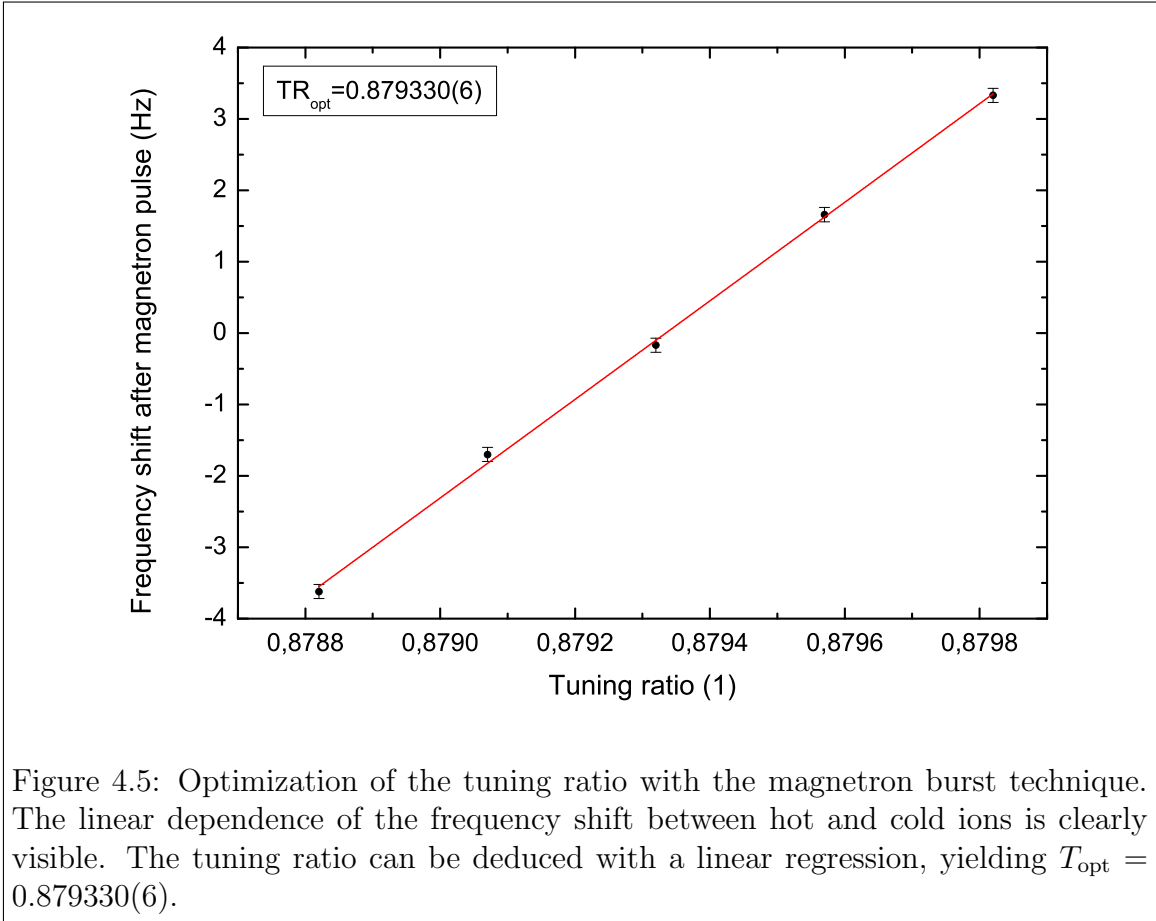
Figure 4.5: Optimization of the tuning ratio with the magnetron burst technique. The linear dependence of the frequency shift between hot and cold ions is clearly visible. The tuning ratio can be deduced with a linear regression, yielding $T_{\text{opt}} = 0.879330(6)$.

4.2.3   Analysis Trap

The AT is dedicated to the detection of the spin-state of the ion using the continuous Stern-Gerlach effect described in chapter 3.2.2.2. In order to resolve the tiny frequency shift caused by the spin of the single electron, the axial frequency has to be extremely stable. However, in the strong magnetic bottle field of the AT, the magnetic moments of all modes cause frequency shifts on the axial frequency. It is therefore of utmost importance to avoid any undesired coupling between the eigenmodes that would easily inhibit successful spin-state detection. For this reason the AT has at least the same requirements on the harmonicity as the PT. In fact the AT is identical to the PT except for the material of the ring, which is gold-plated ferromagnetic nickel with a saturation magnetization of roughly 0.645 T. Again, the magnetic bottle field can be determined with a finite-elements solver (see figure 4.6). As expected, the ring is nearly completely magnetized in the homogeneous field of 3.76 T. In the center of the ring, the additional field is counteracting the homogenous field, lowering the homogenous contribution by $\simeq 1.5\%$. A parabolic fit to the numerical field solution yields a magnetic bottle strength of $B_2 = 10.0(5)\frac{\text{mT}}{\text{mm}^2}$[10], sufficient for making the bound electron spin to cause a frequency shift of ± 120 mHz

---

[10]The uncertainty given here reflects a conservative estimate of the uncertainty of the tabulated saturation magnetization of nickel at cryogenic temperatures.

depending on its alignment. However, when the first ions were transported to the

Figure 4.6: The magnetic field contribution (magnetic bottle) generated by the ferromagnetic ring electrode in the AT can be calculated with the Finite Elements Method (FEM). The diagram shows the axial component of the magnetic field.
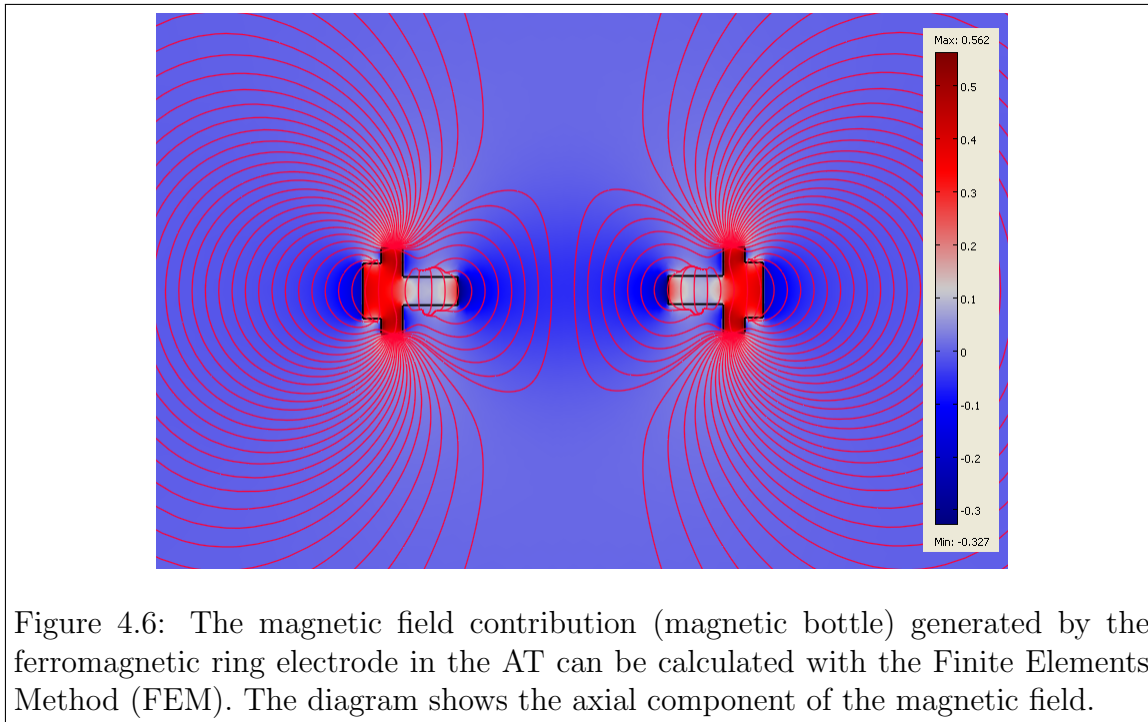
AT, axial frequency fluctuations as large as 100 Hz made the prospect of reliable detection of the 240 mHz frequency change due to spinflips look rather unrealistic. It took a long time and cumbersome data analysis to identify and rule out the major sources of these fluctuations. These can be subdivided into two parts:

- Electrostatic field errors

- Radiofrequency disturbances.

Although the mechanical trap design is identical to the PT, surface patch potentials on the electrodes cause additional fields that are not covered by the Laplace relaxation. These potentials originate on the one hand from inhomogeneous surface coverage with gold, exposing copper and silver, which feature different work functions[11]. On the other hand, the surface can generally feature regions that are electrically isolating, e.g. as result of frozen rest gas. These regions can trap charges from ions lost in the creation process, especially at cryogenic temperatures, where neither rest gas nor diffusion can help to deplete the charge patches. In the AT a large amount of singly charged ions that are unstable in the strong trapping field of the original reflector design[12] were impinging on the electrodes. This problem was solved with the combination of a revised reflector electrode design that features a smoother radial drop of the potential and an additional distance electrode between

---

[11]The work functions depend even on the crystal structure.

[12]The original design of the experiment envisaged a hyperbolically shaped reflector electrode.

the reflector and the AT that absorbs large parts of the remaining ion losses. Additionally new electrodes for the AT were manufactured, which were fine-polished before gold-plating. The combination of these efforts resulted in a dramatically improved electrostatic field quality. For details of this optimization see the Ph.D. thesis of Anke Wagner.

Similarly troublesome is the influence of tiny radiofrequency disturbances that can cause incoherent excitation and coupling of the eigenmodes. Although the setup is extensively shielded from external influences, spurious signals can enter e.g. through magnetic and ground loops created by the excitation lines and subsequently appear at the split correction electrodes, influencing the cyclotron motion. These disturbances have been eliminated by introducing cryogenic solid-state switches that short-out the excitation lines in normal operation close to the trap while they are not needed (see chapter 4.3.3.4). The result of these efforts is a axial frequency stability that is no longer limited by magnetic moment changes but solely by the stability of the precision voltage source [49].

4.2.4 Adiabatic ion transport

Since the spin-state detection with the continuous Stern-Gerlach effect in the AT and the precision frequency measurements in the PT have been spatially separated, the ion has to be transported between these two traps multiple times during the *g*-factor measurement. This transport is realized with adiabatic potential changes, slowly moving the potential minimum from one trap to the other [37]. Since the changes are adiabatic compared to all eigenfrequencies, the energy changes in the eigenmodes during the transport is predictable and the final ion energy is similar to the original if a similar potential strength is chosen. Furthermore, there should be virtually no influence on the particle spin from these smooth transports, which is a crucial requirement for the *g*-factor measurement. Indeed, test measurements have not shown a single spontaneous or transport induced spinflip over several hundred transports, as expected.

However, the adiabatic transport shows an dodgy pitfall that inhibited successful ion transport for a long time. Since in the adiabatic limit the ion follows the electrostatic center of the trap rather than the magnetic field lines, it is important to keep the electrostatic center close to the mechanical center of the trap during the transport. This is especially hard to guarantee for electrodes that are considerably longer than wide. In the center of these electrodes the external electric field vanishes almost completely. Any surface patch potential will now shift the electrostatic center to arbitrarily large radial positions, possibly leading to ion loss at the surface of the electrode during passage. This problem was solved by using exclusively short electrodes in the transport section that feature a strong externally controllable electrostatic center.

4.3 Electronic non-destructive ion detection

In the course of this thesis a cryogenic ion detection system was developed that is able to detect a single stored ion with previously unachievable SNR [44]. Simultaneously,

great care was dedicated to guarantee negligible parasitic retroaction of the detector on the ion, allowing the application of advanced noise feedback temperature control, as described in chapter 4.3.3.2. The system consists basically of two main building blocks, the superconducting resonator that is responsible for the transimpedance amplification of the ion signal, and the ultra low-noise cryogenic solid state amplifier, which serves for picking up the tiny signals of the ion and transporting them to the room-temperature stage for further analysis. All information on the ion is deduced from the signal of these amplifiers and large parts of the experiment are directly depending on their performance, demonstrating the importance of an optimized detection system. Figure 4.7 shows a simplified equivalent circuit diagram of the detection system.
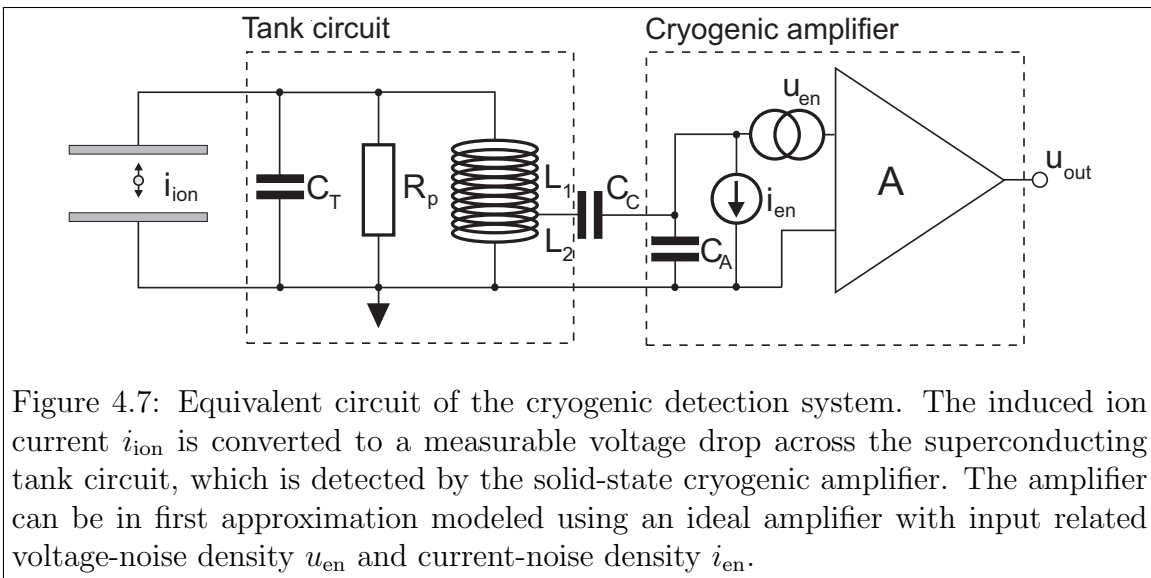
Figure 4.7: Equivalent circuit of the cryogenic detection system. The induced ion current i_{ion} is converted to a measurable voltage drop across the superconducting tank circuit, which is detected by the solid-state cryogenic amplifier. The amplifier can be in first approximation modeled using an ideal amplifier with input related voltage-noise density u_{en} and current-noise density i_{en}.

4.3.1 Detection electronics

In order to detect the induced image current of a single trapped ion cooled to thermal temperatures with good SNR, it is mandatory to produce a large impedance at the frequency of the ion, so that the tiny induced current is transformed into a measurable voltage drop. At the frequencies of the axial motion ($\simeq$MHz), the impedance of the trap system will be limited by the parasitic capacitance of the electrodes and the vacuum feedthroughs for the signal lines. However, by adding a parallel inductance to the system that compensates the capacitance, large impedances can be achieved at the resonance frequency of the resonator. The requirements on the parameters of the detection system depend on the method of detection. For the detection of a coherently excited ion as a peak in the recorded spectrum, the SNR can be defined as the ratio of signal induced onto the resonator and the noise originating mainly from the thermal Johnson voltage-noise density of the resonator [50], the input related

voltage-noise density of the amplifier and the current-noise density of the amplifier flowing to the resonator and measured for a time span τ_m:

$$
\begin{aligned}
\mathrm{SNR}_{\mathrm{peak}} &\equiv \frac{I_{\mathrm{ion}} R_p \kappa \sqrt{\tau_m}}{\sqrt{(u_j \kappa)^2 + u_{en}^2 + (i_{en} R_p \kappa^2)^2}} \\
&= \frac{q\omega_z \kappa R_p \sqrt{\tau_m}}{D\sqrt{2\left(4k_B T R_p \kappa^2 + u_{en}^2 + (i_{en} R_p \kappa^2)^2\right)}} z_{\mathrm{rms}},
\end{aligned}
\tag{4.4}
$$

where $\kappa \equiv L_1/L$ (see figure 4.7) denotes the amplifier noise matching ratio. Typically both noise contributions of the cryogenic amplifier can be neglected for peak detection, giving the simple approximation:

$$
\mathrm{SNR}_{\mathrm{peak}} \simeq \frac{q\omega_z \sqrt{R_p \tau_m}}{D\sqrt{8k_B T}} z_{\mathrm{rms}}.
\tag{4.5}
$$

From this relation it seems obvious that a larger parallel resistance R_p or equivalently a higher quality factor Q and a lower temperature T is desirable. However, considering that the ion is cooled exponentially with a time constant $\tau_{\mathrm{cool}} \sim 1/R_p$ while it is in contact with the resonator, the measurement time τ_m is limited to approximately $\tau_m \leq 2 \cdot \tau_{\mathrm{cool}}$. Without further measures, the achievable SNR will thus not scale at all with the quality factor (provided that it is sufficiently high to support equation (4.5)), however feedback cooling can remove this limitation.

The detection of the ion with the dip method (see chapter 3.3.1) imposes even stronger demands on the performance of the detection system. Since in this detection mode there is no distinctive signal above the noise floor of the thermal noise anymore but rather the signature is the absence of the thermal noise at the frequency of the ion, the SNR is defined as the ratio of the thermal noise and the remaining noise floor at the frequency of the ion, caused by the electronic noise contribution of the amplifier:

$$
\mathrm{SNR}_{\mathrm{dip}} = \frac{\sqrt{4k_B T R_p \kappa^2 + (i_{en} R_p \kappa^2)^2}}{u_{en}},
\tag{4.6}
$$

Interestingly, the temperature and the current-noise contribution now both appear in the nominator of the SNR, showing that dip detection becomes simpler with higher temperature of the detection system. However, the increased SNR comes at the expense of an increased ion temperature in equilibrium, generating highly undesired systematic frequency errors. The most reasonable method for increasing the SNR is the optimization of the voltage-noise contribution of the cryogenic amplifier, together with an optimization of the tank circuit quality factor as well as the detector coupling κ.

4.3.2 Axial tank circuit

For an ideal parallel resonator, the impedance approaches infinity at the resonance frequency

$$
\nu_R = \frac{1}{2\pi\sqrt{LC}}.
\tag{4.7}
$$

In reality, the parallel resistance of a tank circuit is limited by ohmic losses in the conductors and dielectric losses in the isolation of the conductors and the surrounding of the coil. The parallel resistance R_p of the tank circuit is connected to its quality factor Q and inductance L by [51]

$$R_p = Q\omega L. \tag{4.8}$$

The quality factor is defined as the inverse relative spectral width of the resonator: $Q = \frac{\nu_R}{\delta\nu}$, or

$$Q = \nu_R\tau, \tag{4.9}$$

where τ denotes the exponential rate of energy loss. As expected, the quality factor increases if the rate of energy loss is decreased or if the time scale of the oscillation is shortened.

Since the trap electrodes are surrounded by vacuum, the energy loss of the parasitic trap capacitance is almost negligible. The main loss mechanisms are resistive heating from the ion current and dielectric heating in the wire insulation, typically FORMVAR. Both processes obviously scale linearly with the wire length l_w, while the stored energy scales with the inductance L:

$$E_{\mathrm{mag}} = L \cdot I^2, \tag{4.10}$$

leading to the conclusion that the inductance per wire length should be maximized in order to minimize losses. Simultaneously, the capacitance should be minimized such that the resonator frequency increases (compare equation (4.9)). The helical resonator geometry is a good choice for this figure of merit. For a long helical coil with diameter D_{coil} and length l the inductance can be roughly estimated by:

$$L \simeq N^2\frac{D_{\mathrm{coil}}^2}{l}\mathrm{nH}. \tag{4.11}$$

The wire length is $l_w \simeq N\pi D$, so that it is possible to express the figure of merit as:

$$Q \sim \frac{L}{l_w} \simeq \frac{D_{\mathrm{coil}}}{\pi d}, \tag{4.12}$$

for densely wound coils with wire diameter d. Equation (4.12) tells that the quality factor depends linearly on the coil diameter. Since in reality available space is limited, especially in the cryogenic region of the experiment, the quality factor achievable has to be additionally optimized by directly lowering the losses. This is possible by using superconducting wire, which shows essentially negligible resistive losses for frequencies below $\sim$1 MHz. All materials within the high-field region of the coil, including wire insulation material, coil core and fixation material, should feature low dielectric loss tangents. In this work, PTFE[13] was chosen.

The experiment needs two resonators, one for each of the two main traps. The resonator for the AT is significantly larger than the one for the PT and accordingly

---

[13]PTFE: Polytetrafluoroethylene or colloquially Teflon.

	Analysis Trap	Precision Trap
Resonance Frequency (kHz)	412	711
Inductance (mH)	5.36	1.5
Quality factor	3100	950
Parallel resistance (MΩ)	43	6.8

Table 4.1: Parameters for the AT and PT axial resonators in the final setup.

shows a larger quality factor. The parameters of the two resonators are compiled in table 4.1.

4.3.3   Ultra low-noise amplifier

The second key component of the detection system is the solid state amplifier in the cryogenic region that samples the voltage induced by the ion and the thermal noise of the tank circuit. In order to limit the capacitance of the tank circuit and the dielectric loss angle of the overall system, it is absolutely necessary to place the amplifier as close as possible to the resonator, directly in the cryogenic region. This again means, that the amplifier has to cope with both the low temperature and the magnetic field of ~ 3 T. The magnetic field inhibits the use of any ferromagnetic components, which would not only degrade the homogeneity of the magnetic field but also would be completely magnetized, discontinuing proper function in most cases. Furthermore, most integrated electronics based on silicon semiconductor material will suffer from carrier freeze-out at the temperature of 4.2 K [52]. Since for silicon the typical donor and acceptor activation energy for doping with group 3/5 elements is around 50 meV, at 4.2 K only a small fraction ($< 1\%$) of the majority carrier states are activated, inhibiting the function as semiconductor. Luckily other compound semiconductors as Gallium-Arsenide (GaAs) allow doping with elements that generate carrier states with significantly lower activation energy around 6 meV (at least for the donor levels). Still, the special conditions of the *g*-factor experiment require the design of specialized, discretely[14] built electronics. In the course of this thesis a novel amplifier system was developed that surpasses the performance of the previously used amplifiers by far in all fundamental requirements:

- Low voltage-noise density around the axial frequency of the ion

- Low power consumption

- High input resistance

- Negligible parasitic feedback

---

[14]Discrete here means that only basic passive, reactive and active elements are used, e.g. transistors, without the use of complex integrated circuits as operation amplifiers.

- Low current-noise density.

The requirements of high input resistance and low current-noise density, emerging from the demand of a high SNR (see chapter 4.3.1), make the use of field effect transistors (FET), configured in common source topology (see figure 4.8), preferable. Most commercially available GaAs based FETs are configured as MESFET[15], where
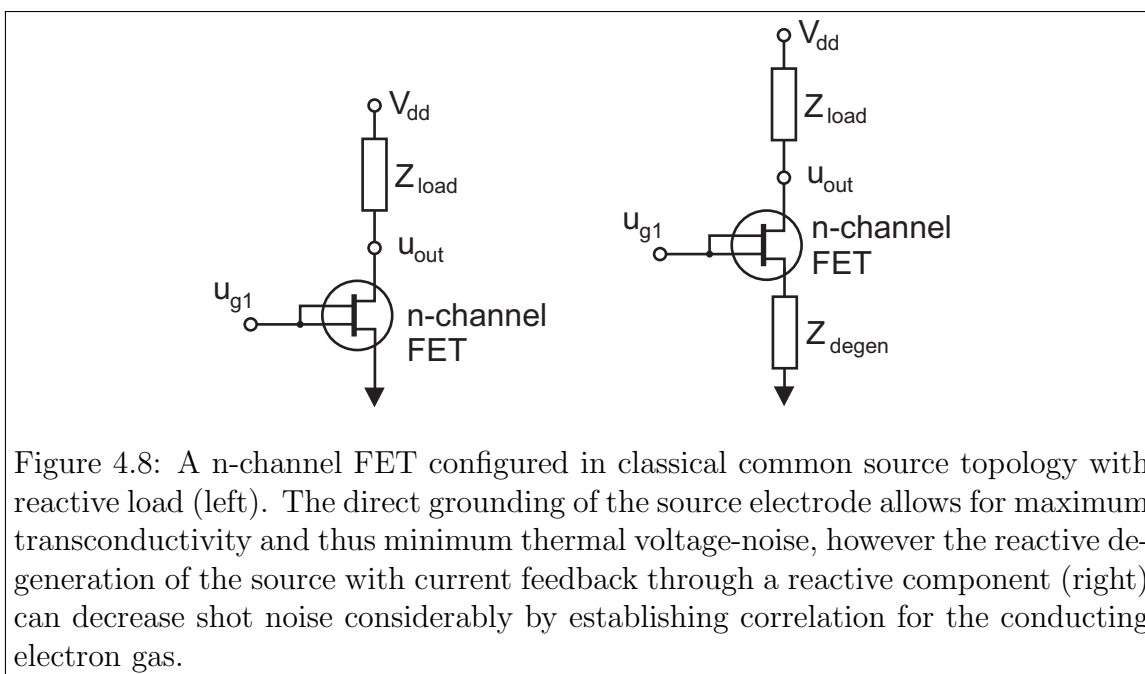
Figure 4.8: A n-channel FET configured in classical common source topology with reactive load (left). The direct grounding of the source electrode allows for maximum transconductivity and thus minimum thermal voltage-noise, however the reactive degeneration of the source with current feedback through a reactive component (right) can decrease shot noise considerably by establishing correlation for the conducting electron gas.

the gate electrode is a backwards biased diode, quite similar to a JFET[16], but instead of using a p-n semiconductor junction, the gate is a Schottky-type metal contact directly grown on the semiconductor substrate. Owing to the comparably high carrier mobility in GaAs, these transistors are commonly used for high-frequency components operating at frequencies in excess of 10 GHz. The optimization of the MESFETs for these frequencies causes drawbacks if they are used for measurements at the comparably low axial frequency of approximately 1 MHz. These drawbacks have been directly addressed in the design of the amplifier. In the future, the design of a specialized transistor for cryogenic low frequency measurements could give even more room for optimization, however until now the high prize for the production of a custom transistor forbid this option. Comparing the MESFET with other transistor types which potentially work at liquid helium temperature, shows that the MESFET is by far the most reliable and simple to use type. Transistors based on silicon-germanium heterostructures (SiGe) promise extremely low input related voltage-noise, in the order of less than 100 pV/$\sqrt{\text{Hz}}$ [53]. However, since these devices until now are only available as bipolar transistors, the current-noise density will undo this advantage if the amplifier is connected to the tank circuit, although these transistors

---

[15]MESFET stands for MEtal on Semiconductor Field Effect Transistor.
[16]JFET: Junction Field Effect Transistor

can be very advantageous when used for broadband detection [54] where the input impedance is lower. Silicon based JFETs will mostly not work at 4.2 K, however, by proper thermal isolation, these transistors can be heated with the power dissipated in the channel to higher temperatures. Due to the lower carrier mobility of the silicon bulk material, these transistors can be advantageous for low frequency detection, but again current-noise density has to be considered. Additionally the handling of these devices would be quite complicated, as the transistor properties will depend strongly on the die[17] temperature. The MESFET features an extremely low current-noise density, since the gate leakage current decreases exponentially towards lower temperatures, reaching a typical level of less than 1 fA/$\sqrt{\text{Hz}}$ at 4.2 K. The voltage-noise density of these devices also decreases with the temperature, however low frequency noise will generally dominate at the frequencies considered here. For a decent noise optimization the origin of the noise contributions has to be analyzed.

4.3.3.1   Noise sources for the cryogenic MESFET

Several contributions to the noise of a MESFET based transistor amplifier can be differentiated [55]. The conducting drain-source channel has an effective resistance r_{ds} that causes Johnson-type thermal noise

$$u_1^2 = 4k_B T r_{ds}, \tag{4.13}$$

which decreases with the channel temperature. Since this noise contribution is frequency independent, it is called white noise. For frequencies in excess of 10 MHz the channel thermal noise is the dominant noise contribution. In general, the channel noise will couple to the gate electrode via the Drain-Gate capacitance C_{gd}, possibly causing a considerable excess noise at the resonance frequency of the tank circuit. The thermal noise contribution can be derived from the static properties of the transistor and can be optimized by choosing a proper operating point for the transistor. Shot noise of the drain current can potentially add a white noise contribution, but is generally of little importance due to the relatively large drain currents used. Source degeneration can cancel large parts of the shot noise if extremely low drain currents have to be used. The frequency dependent noise contributions can be more troublesome. In the frequency range of interest for the g-factor experiment most contributions fall with 1/f or faster. The frequency where the 1/f or flicker noise becomes comparable to the white thermal noise background is referred to as the flicker noise corner. It is highly desirable to push this corner to frequencies lower than the axial frequency. Flicker noise (sometimes referred to as pink noise due to the large fraction of low frequency noise) is caused by processes related to impurities within the semiconductor material. The dominant effects are generation and recombination (g-r) noise and mobility fluctuations due to scattering at impurities [56], making the 1/f noise strongly dependent on the production process. As a result, flicker noise will vary between different transistors of the same type and especially between different production batches. G-r noise, which typically dominates at room temperature, is

---

[17]Die: the piece of semiconductor, i.e. the active part of the transistor.
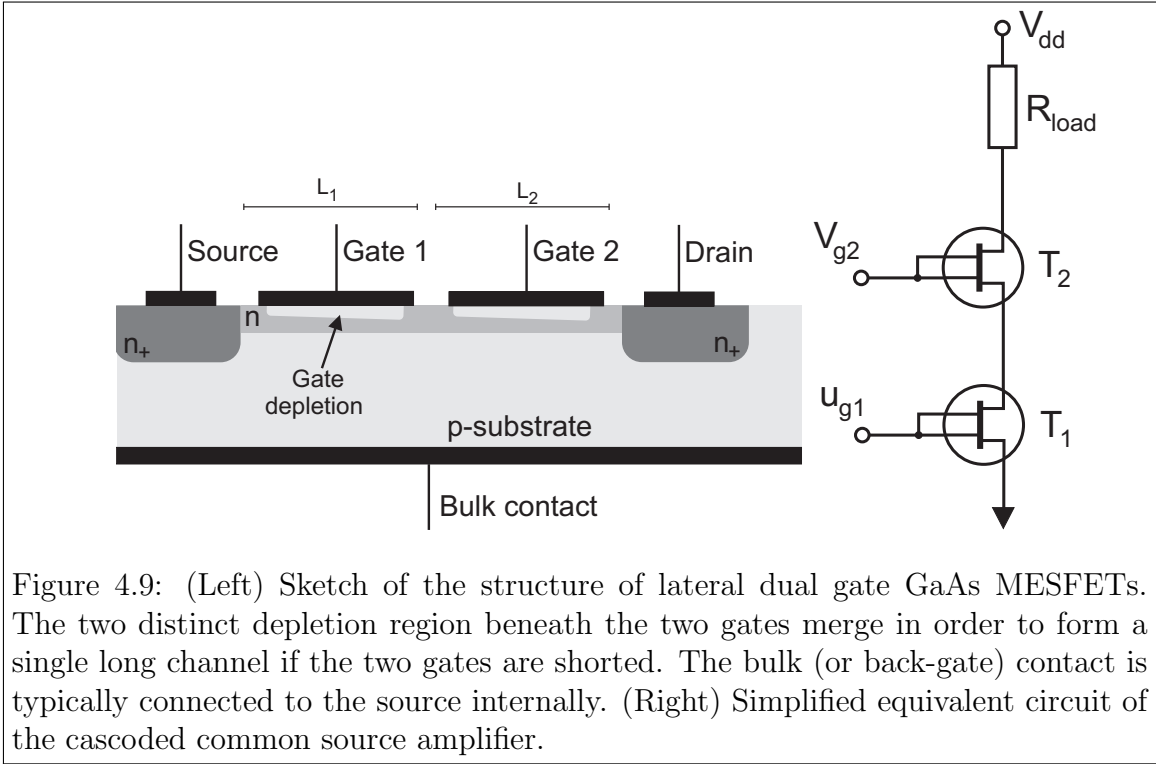
Figure 4.9: (Left) Sketch of the structure of lateral dual gate GaAs MESFETs. The two distinct depletion region beneath the two gates merge in order to form a single long channel if the two gates are shorted. The bulk (or back-gate) contact is typically connected to the source internally. (Right) Simplified equivalent circuit of the cascoded common source amplifier.

caused by the random thermal creation and trapping of carriers at impurities mainly in the depletion region of the gate. Since the depletion area scales with the device size $W \cdot L$, g-r noise can be influenced with transistor design only weakly and at the expense of the gate capacitance. Fortunately, g-r noise decreases dramatically with device temperature, since the trapped charges will not be activated at sufficiently low temperature [56]. At these temperatures the fluctuation of the carrier mobility due to random scattering at impurities dominates the flicker noise. This process can be described by the empirical Hooge equation [57]:

$$u_2^2 = \alpha_L \frac{I_{ds}^2 r_d s^2}{NL},$$ (4.14)

where α_L is an empirical parameter dependent on the fabrication process, I_{ds} is the dc drain current, r_{ds} the effective drain resistance, N the number of free charges in the channel and L the channel length. Assuming that the transistor is operated in the strong inversion regime, the drain current can be expressed as [58]:

$$I_{ds} = k_n \frac{W}{L} \left((V_{gs} - V_T) V_{ds} - \frac{V_{ds}^2}{2} \right),$$ (4.15)

where k_n is a proportionality constant depending on several semiconductor parameters, and V_T denotes the threshold voltage of the drain-source channel. These equations can be combined to find an expression for the flicker noise density:

$$u_2^2 \sim \frac{1}{L^2 f}. \tag{4.16}$$

Interestingly, the voltage-noise density caused by the mobility fluctuation scales strongly with the channel length. This is because the number of available carriers increases with the channel length, while the drain current decreases with L. For low frequency appliances as the axial amplifier, this paves the way for a significant reduction of the effective electronic noise by choosing or designing a transistor with a long channel. Unfortunately, almost all GaAs-MESFETs are short channel devices, optimized for high-frequency operation where flicker noise is of no concern. Hence, for the cryogenic amplifier an artifice is exploited: many of the commercially available transistors are dual-gate devices, that incorporate basically two transistors in series that share one degenerate electrode, meant for the implementation of cascoded amplifiers. By shorting the two gates of such devices, the channel will extend from the source of the lower device all the way to the drain of the upper transistor. The effective channel length is thus approximately the sum of the length of both transistors. If both devices have comparable gate length, the resulting flicker noise contribution will be lower by a factor of 4, while the input capacitance only increases by a factor of 2. Additionally, all incoherent noise contributions can be cut down by a factor of $1/\sqrt{N}$ by paralleling N identical transistors.

In order to inhibit parasitic feedback of the amplified signal through the gate-drain
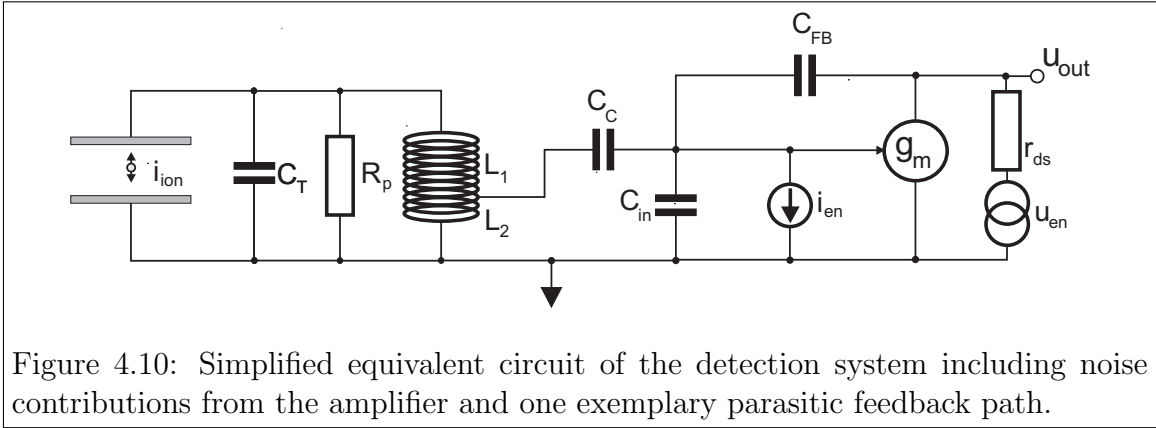
Figure 4.10: Simplified equivalent circuit of the detection system including noise contributions from the amplifier and one exemplary parasitic feedback path.

Miller [59] capacitance, radiofrequency shielding with conducting sheets can be employed. A more elegant measure is, however, the spatial isolation of the primary gate from the hot end of the amplifier, which becomes possible through the implementation of a dedicated discrete cascode stage. To this end, a further transistor with fixed gate voltage is connected in series to the primary transistor, acting as a low impedance load or voltage source for the primary transistor while forming a

high parallel impedance for the resistive load R_{load} (see figure 4.9). This way, the small-signal current through the first transistor T_1 is given by

$$i_{ds} = g_{m1}u_{g1}, \tag{4.17}$$

where g_{m1} is the small signal transconductance of the primary transistor T_1. Since the voltage at the gate of the second transistor is held fixed, the voltage at the drain of T_1 is given by:

$$u_{d1} = -\frac{g_{m1}}{g_{m2}}u_{g1}. \tag{4.18}$$

If the transconductance of the second transistor is similar or larger than that of the first transistor, the voltage appearing across the miller capacitance of T_1 is only $2u_{g1}$, far less than the voltage between the hot end and the input. Furthermore, since the load is almost purely resistive, the phase of the feedback signal is well defined and exactly $180°$. At the drain of T_2, the current i_{ds} creates the amplified voltage across the load resistance R_L:

$$u_{\text{out}} = -i_{ds}R_L \parallel r_{ds} = -u_{g1}g_{m1}\frac{R_L r_{ds}}{R_L + r_{ds}} \equiv -Au_{g1}. \tag{4.19}$$

Together with proper definition of ground planes and suitable choice of PCB[18] material (laminated TEFLON sandwich), these measures ensure negligible back action on the tank circuit, even for very high quality factors where the resonator acts as very effective signal pickup. The compound discrete cascode amplifier is thus well suited as voltage amplification stage for the cryogenic amplifier. In order to transport the signal to the room temperature stage via long coaxial cable without imposing a strong capacitive load for the primary stage, a third transistor configured as source follower is added. The input of this stage is highly resistive, while the output can be adjusted to the $50\ \Omega$ impedance of the transmission line. The voltage follower provides no further voltage amplification (in fact the voltage amplification is always slightly lower than unity), but can deliver the current necessary in order to drive the transmission line and furthermore serves for decoupling the room temperature stage from the cryogenic tank circuit. This helps in preventing reflections in the long cables, which could cause oscillations. The actual implementation of the amplifier furthermore adds filters for decoupling the gate and drain biasing from the radiofrequency signals. The gate voltages of T_1 and T_2 are controlled from the room temperature stage in order to adjust the operating point of the transistors. Since the amplifier is not self-biassing, the optimal gate bias voltages are strongly dependent on the production process, such that paralleled devices should be roughly selected for similar characteristics.

The input related voltage-noise density of $400\ \text{pV}/\sqrt{\text{Hz}}$ for frequencies in excess of 400 kHz (see figure 4.12) in combination with the extremely low current-noise density of $\sim 1\ \text{fA}/\sqrt{\text{Hz}}$, the negligible back-action, the low power consumption and the static input capacitance of only 4 pF makes this cryogenic amplifier unique and interesting for a number of experiments. Accordingly, the design was adopted for the

---

[18]PCB: Printed Circuit Board
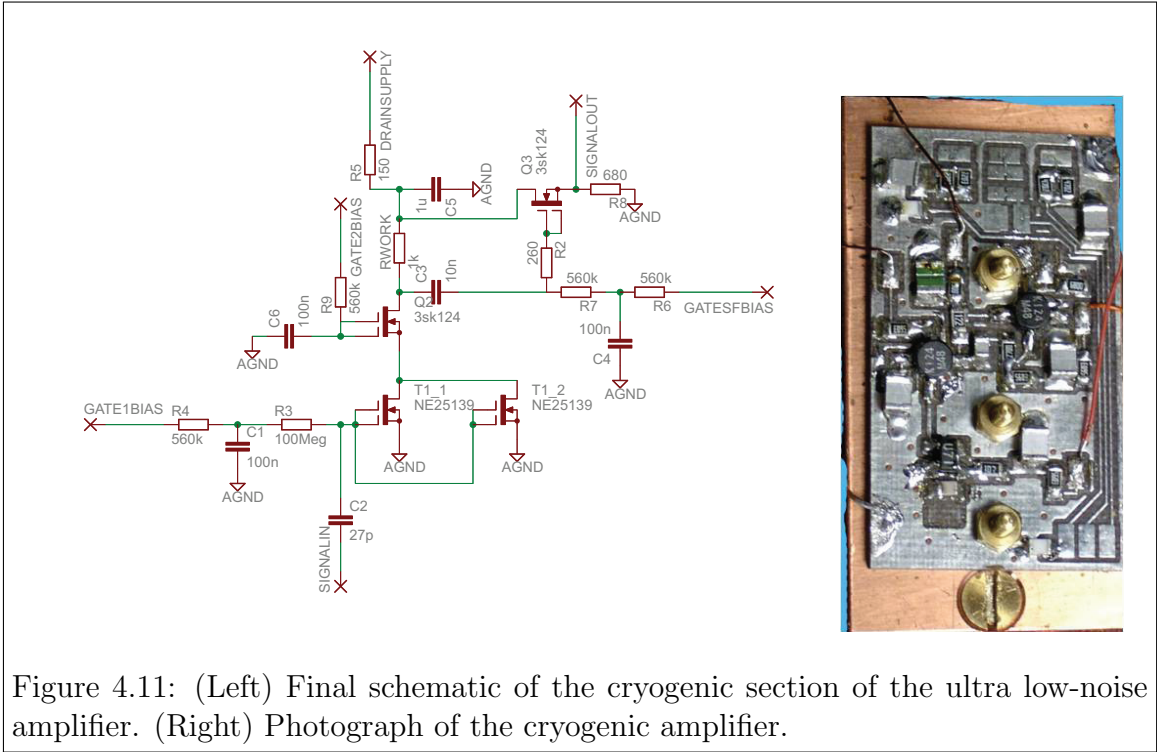
Figure 4.11: (Left) Final schematic of the cryogenic section of the ultra low-noise amplifier. (Right) Photograph of the cryogenic amplifier.

broad-band detection system of the TRIGATRAP [60] experiment, at the cryogenic storage ring CSR in Heidelberg [61], and will also be used in the upcoming ultra high-precision mass measurement setup PENTATRAP [62].

4.3.3.2 Electronic feedback

Considerable effort was dedicated in order to minimize the parasitic back action of the novel cryogenic amplifier. Simultaneously, the voltage-noise background of the amplifier has dropped far below the Johnson noise density of the resonator. This fact can be expressed by considering the noise temperature of the amplifier, which is defined as the equivalent temperature of the source T_s that would make the Johnson noise power of the source equivalent to the voltage-noise of the shorted amplifier input [63]:

$$4k_B T_s R_p = u_{en}^2 \Rightarrow T_s = \frac{\kappa u_{en}^2}{4k_B R_p} \simeq 23\text{mK}. \qquad (4.20)$$

This remarkable number already suggests that the new amplifier can be used for advanced control over the physical tank circuit parameters as electron gas temperature and quality factor by allowing for a well controlled feedback of the measured noise onto the resonator [64]. Figure 4.14 shows the connection diagram used for implementing noise feedback control. For simplicity the small current-noise contribution will be neglected in the analysis. If the feedback is switched off ($u_0 = 0$), the small capacitance $C_{FB} \simeq 0.3$ pF only adds to the parallel capacitance of the tank circuit C_T. The effect of non-vanishing amplification depends on the phase and amplitude of the generalized complex amplification $A = a + \imath b$, which contracts the
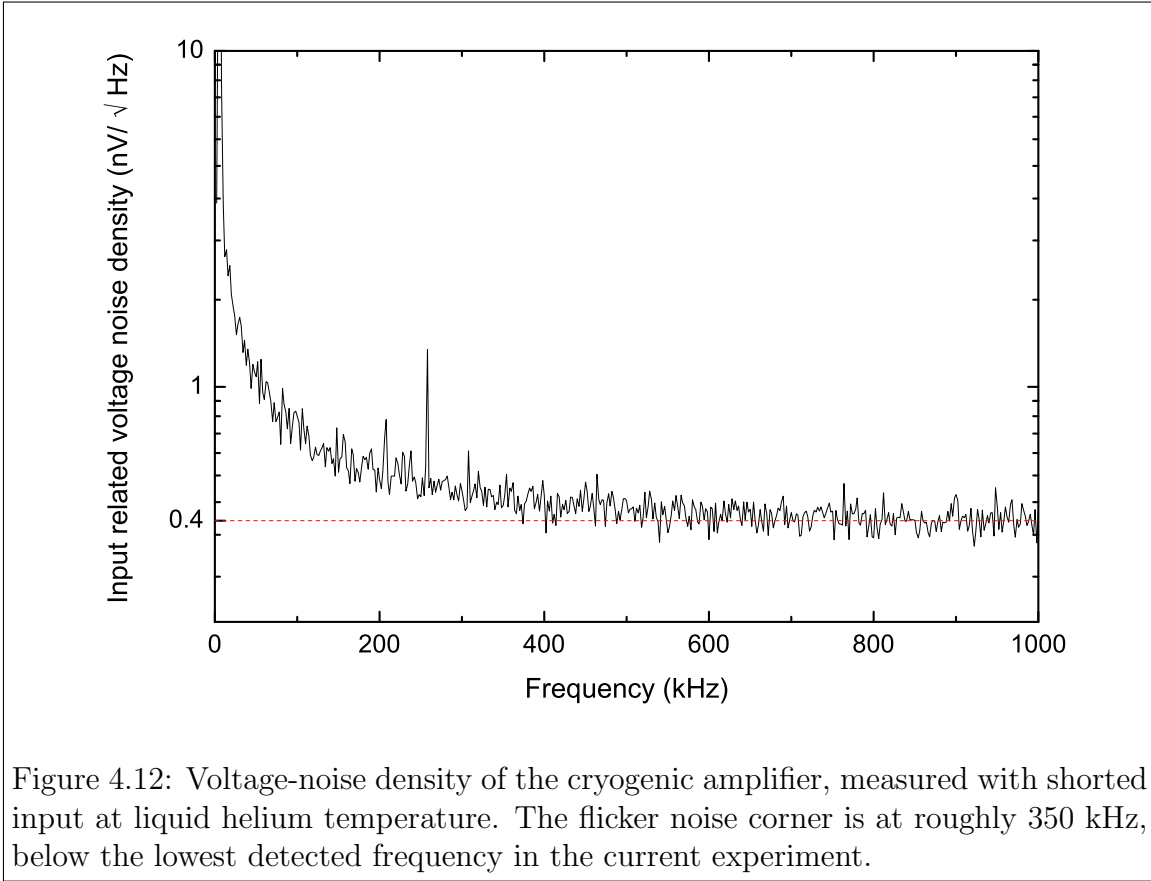
Figure 4.12: Voltage-noise density of the cryogenic amplifier, measured with shorted input at liquid helium temperature. The flicker noise corner is at roughly 350 kHz, below the lowest detected frequency in the current experiment.

coupling constant κ, the feedback free amplification A_c and the transfer function of the phase shifter and the attenuator. Two orthogonal cases can be distinguished that are termed 90° and 180° feedback, respectively. If the feedback gain is exactly 180°, the effective impedance of the feedback capacitor becomes:

$$Z_{\text{FB,eff}} = \frac{u_1}{u_1 - u_0} \frac{1}{\imath\omega C_{\text{FB}}} = \frac{1}{\imath\omega(1 - A)C_{\text{FB}}}. \tag{4.21}$$

This result shows that it is possible to alter the effective parallel capacitance of the resonator by applying 180° feedback. In principle it is possible to shift the resonance of the axial resonator to any arbitrary frequency. However, the additional noise and the difficulty to maintain exactly 180° in the feedback phase for all frequencies limits the tuning range with this method to typically a few linewidths of the resonator. This is sufficient to increase e.g. the cooling time constant considerably, which is extensively used during the phase sensitive axial frequency detection in the analysis trap (see chapter 5.7).

Fundamentally different is the effect of 90° feedback. At the resonance frequency of the tank circuit, parts of the Johnson thermal noise of the effective parallel resistance
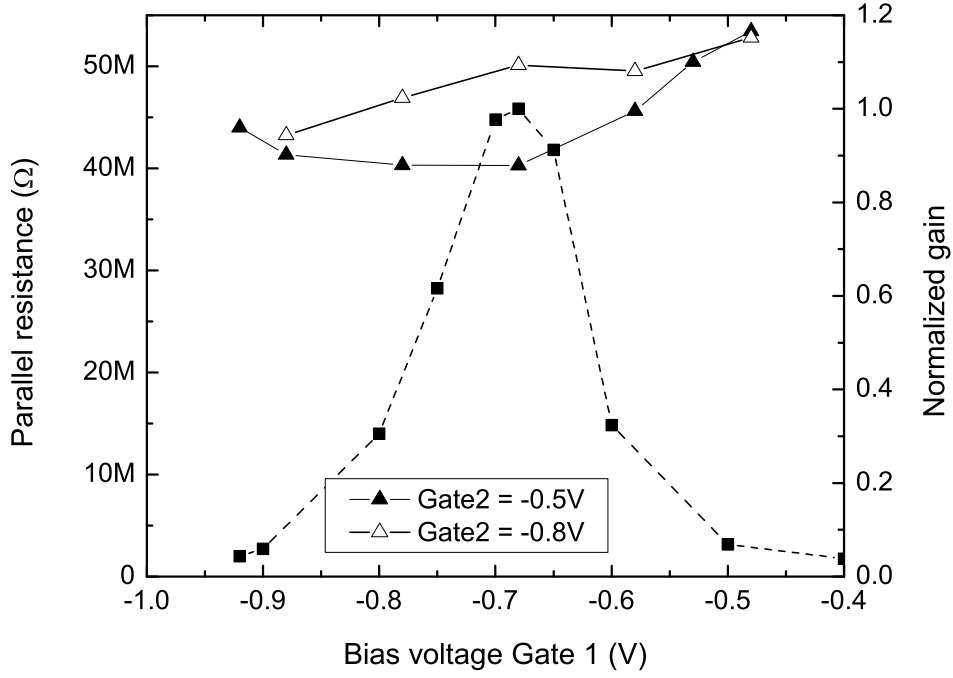
Figure 4.13: Normalized amplifier gain (filled squares) and the resultant tank circuit quality factor (triangles) for two different bias settings of the cascode gate (Gate2) for the novel cryogenic amplifier. The voltage at Gate2 has only very little influence on the amplification. If the cascode is well set-up (open triangles), the Q-value (or parallel resistance) is virtually independent of the amplifier gain, which demonstrates the negligible back-action even for very high quality factors.

R_p is coherently reinjected through the feedback capacitor C_{FB}. The excess current through the tank circuit due to feedback is:

$$I_{\mathrm{FB}} = u_0 \imath \omega C_{\mathrm{FB}}. \qquad (4.22)$$

The feedback thus acts to make the voltage across the tank circuit u_1:

$$u_1 = \frac{1}{1 - \imath \omega R_p C_{\mathrm{FB}} A} u_J \equiv \gamma u_J. \qquad (4.23)$$

Simultaneously the effective parallel resistance of the tank circuit, as seen by the trapped ion, is also altered by the feedback loop:

$$R_{\mathrm{eff}} \equiv \frac{\partial u_1}{\partial i_{\mathrm{ion}}} = \gamma R_p \qquad (4.24)$$
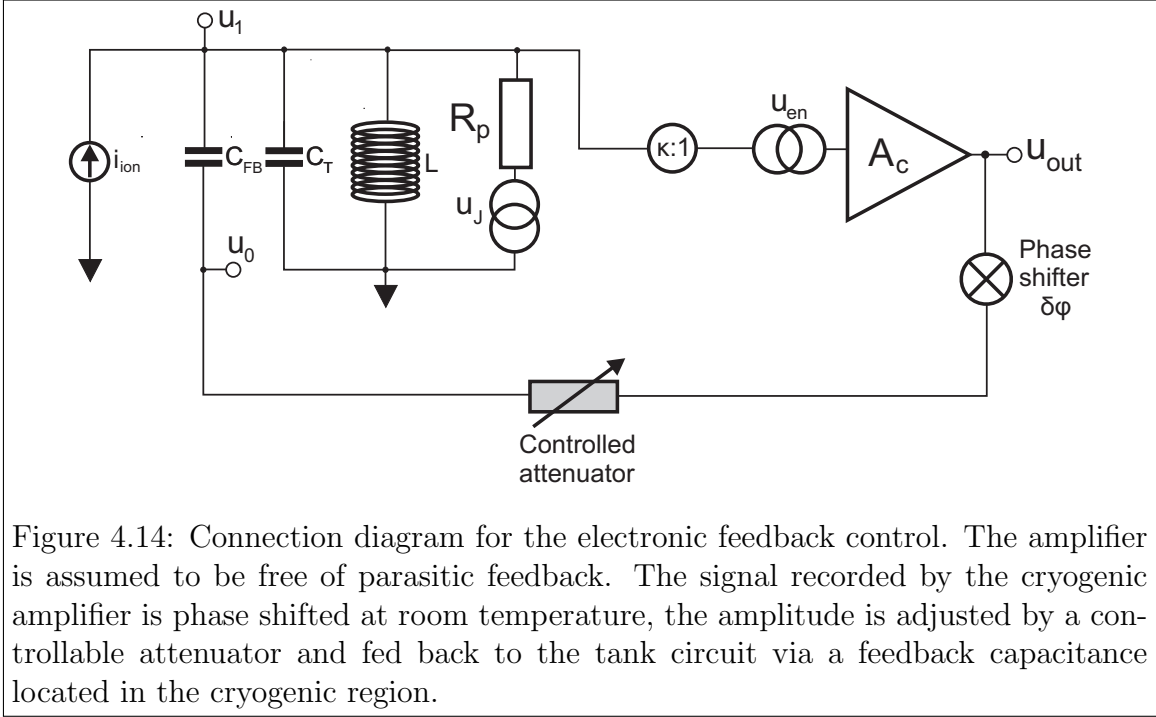
Figure 4.14: Connection diagram for the electronic feedback control. The amplifier is assumed to be free of parasitic feedback. The signal recorded by the cryogenic amplifier is phase shifted at room temperature, the amplitude is adjusted by a controllable attenuator and fed back to the tank circuit via a feedback capacitance located in the cryogenic region.

Combining equations (4.23), (4.24) and (3.50) reveals that the resonator with closed loop 90° noise feedback can be modeled as a passive resonator with effective parameters:

$$T_{\text{eff}} = \gamma T \tag{4.25}$$
$$R_{\text{eff}} = \gamma R_p. \tag{4.26}$$

This result opens the possibility to actively control the temperature and Q-value of the tank circuit, allowing either the detection with arbitrarily high SNR or the cooling of the ion below the equilibrium temperature of the tank circuit lattice. Although the feedback parameter γ is unbound, the finite electronic excess noise of the cryogenic amplifier acts to limit the lowest achievable temperature. Again, the excess current due to the electronic voltage-noise u_{en} (equation (4.22)), amplified in the closed feedback loop, generates a voltage drop

$$u_1^{\text{en}} = \imath\omega C_{\text{FB}} R_p \tag{4.27}$$

across the tank circuit's parallel resistance R_p. This yields a closed loop electronic noise contribution of

$$u_1^{\text{en}} = (\gamma - 1)\frac{u_{\text{en}}}{\kappa}. \tag{4.28}$$

Assuming that the Johnson noise and the electronic noise of the amplifier are uncorrelated, the final noise amplitude at the resonator is:

$$u_1^{\text{full}} = \sqrt{(\gamma u_J)^2 + \left((\gamma - 1)\frac{u_{\text{en}}}{\kappa}\right)^2}. \tag{4.29}$$
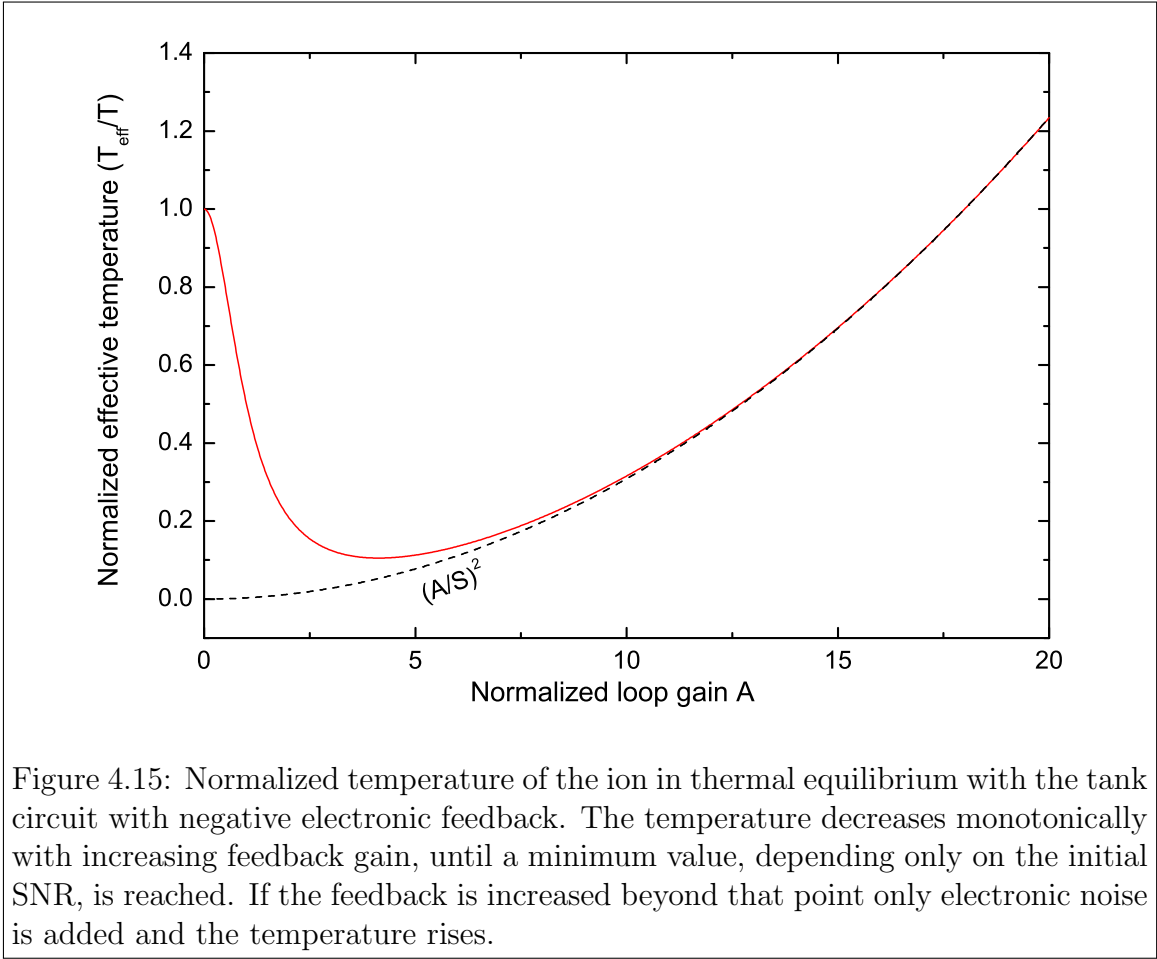
Figure 4.15: Normalized temperature of the ion in thermal equilibrium with the tank circuit with negative electronic feedback. The temperature decreases monotonically with increasing feedback gain, until a minimum value, depending only on the initial SNR, is reached. If the feedback is increased beyond that point only electronic noise is added and the temperature rises.

In combination with the still valid expression $R_{\text{eff}} = \gamma R_p$, it is possible to derive the closed loop temperature of the tank circuit including the electronic noise contribution:

$$T_{\text{eff}}^{\text{en}} = T \left(\gamma + \frac{(\gamma - 1)^2}{\gamma} \frac{1}{\text{SNR}^2} \right). \tag{4.30}$$

The minimum achievable temperature thus depends only on the lattice temperature of the tank circuit and the SNR of the detector. For SNRs in the order of 26 dB as in the g-factor experiment of the work presented here, the minimum temperature can be reasonably well approximated by

$$T_{\text{min}} \simeq T \cdot \left(\frac{1}{19.159 + 0.99275(\text{SNR} - 20)} \right) \simeq 248\text{mK}. \tag{4.31}$$

Figure 4.15 shows the achieved closed loop temperature as function of the normalized feedback gain. Evidently it is counterproductive to increase the feedback gain beyond the optimal value since the additional electronic voltage-noise will increase the particle temperature excessively. However, the temperature increase is not as sharp as equation (4.30) suggests since in the experimental realization the loop am-
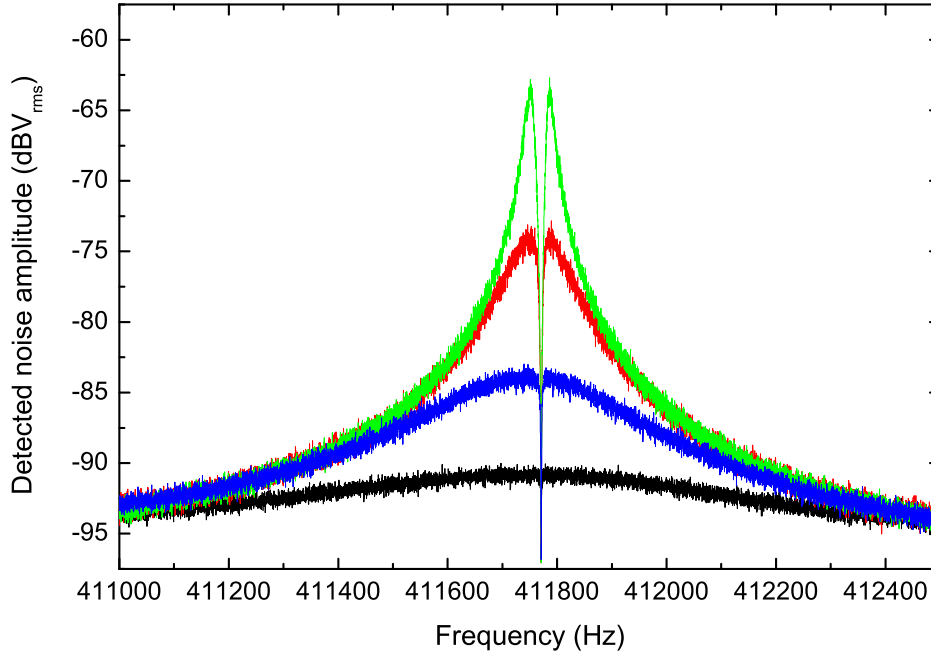
Figure 4.16: Thermal noise of the AT resonator with various strengths of the feedback gain. The narrow feature superimposed to the resonance is the axial dip signal of a single ion.

plification A, rather than the parameter γ, is varied linearly.

If positive feedback is applied, the Q-value of the tank circuit can be increased arbitrarily, simplifying the rapid detection of ions with low charge. However, excessively increasing the positive feedback gain beyond the divergence $\gamma \to \infty$ will cause spontaneous oscillation of the tank circuit, possibly leading to ion loss.

For precision measurements it is very important to avoid parts of the feedback to be parasitically applied directly to other electrodes, since this feedback (which will generally have an unpredictable phase) will lead to systematic frequency shifts by detuning the series resonator equivalent circuit of the ion. If the feedback is applied directly to the resonator, the extremely low amplitudes are typically negligible.

4.3.3.3 Development of a self-excited single ion oscillator (SEO)

Even with negative feedback on the tank circuit the measurement time available for coherent frequency or phase determination is limited since the ion is cooled during data taking. Infinite measurement time can be achieved by applying negative feedback deliberately to one of the trap electrodes. The force exerted on the ion will now depend only on the difference of the voltage at the electrodes $u_1 - u_0$ (possibly weighted by a dimensionless factor if different electrodes are used). If the

ion is excited to large amplitudes so that Johnson noise and electronic noise can be neglected in first order, the effective voltage can be calculated:

$$du \equiv u_1 - u_0 = u_1(1 - A). \tag{4.32}$$

Equivalently, the effective cooling time constant τ_{eff} can be expressed as:

$$\tau_{\text{eff}} = \frac{\tau}{1 - A}. \tag{4.33}$$

Obviously the cooling time diverges at $A = 1$, since at this setting there is no effective dissipative force acting on the ion [64]. The ion will in principle remain on any amplitude that it is excited to and allow for very accurate determination of the motional parameters. However, any mistuning or unintentional change of the amplification A will lead either to an exponentially changing amplitude. In order to make the direct feedback usable, the feedback amplitude A has to be regulated in realtime, keeping the amplitude determined from a floating time window DFT[19] constant. This has been implemented in the course of this thesis on basis of a dedicated DSP[20] board equipped with self developed analog circuitry that allows a regulation of the feedback gain from within the DSP firmware. In the beginning, when the ion is cooled to thermal equilibrium, the feedback amplitude is maximized, leading to self-oscillation that increases the thermal oscillation until the desired particle amplitude is reached. Hereafter, the ion amplitude is regulated to a fixed value with a simple PID[21] regulator implemented in the DSP firmware. Simultaneously the ion frequency is determined from the phase evolution of the detected DFT signal. With this setup, the detection of the axial frequency to within the information theoretical Cramér-Rao bounds [65] is possible. Since the ion is continuously monitored, the frequency resolution scales proportional to $1/\sqrt{T_{\text{meas}}^3}$. However, it is necessary to cancel the parasitic feedback appearing on the resonator by applying suitably scaled feedback amplitudes to different electrodes [66]. This way it is possible to null the effective feedback on the resonator, while keeping a finite force acting on the particle. In practice this method is exceedingly laborious, considering that a much simpler method (see chapter 5.4.1) is giving satisfactory results.

In the future, the SEO can be applied for the spin-state detection of heavier ions, where the axial frequency difference due to spin flips is getting exceedingly small.

4.3.3.4   Cryogenic switches

As mentioned in chapter 4.2.3, radiofrequency noise introduced into the cryogenic region of the experiment either through coupling to magnetic loops formed, e.g., by the ground returns or by imperfect shielding properties of the coaxial excitation lines can cause highly undesirable parasitic influence on the motional energies of the ion,

---

[19]DFT: Discrete Fourier Transform. Within the DSP, a DFT rather than a FFT is implemented, since the DFT can determine the Fourier series of a running time sample more effectively by reusing the overlapping data.

[20]DSP: Digital Signal Processor

[21]PID: Proportional, Integrating, Differential
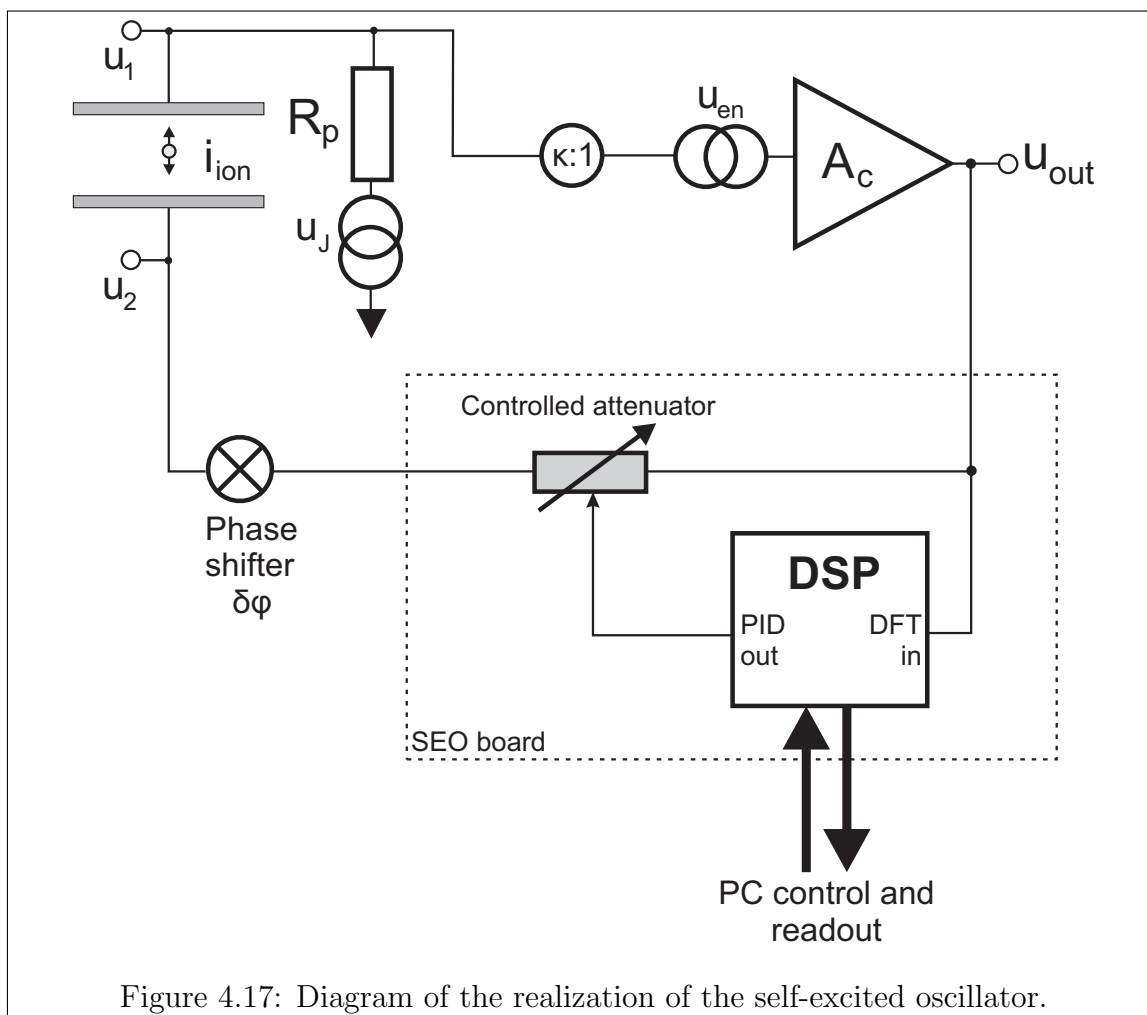
Figure 4.17: Diagram of the realization of the self-excited oscillator.

possibly inhibiting successful spin-state detection. Over and above the elaborate shielding of external noise, a major breakthrough was achieved by introducing solid-state analog switches in the cryogenic region. These switches allow to shortcut the excitation lines while they are unused. Despite the conceptional simplicity of the switches (see figure 4.18), the effect on the experiment was both surprising and resounding. For successful spin-sate detection it is absolutely necessary to keep the switches closed. A similar effect might be achieved by a stronger decoupling of the excitation lines, however this would call for larger excitation amplitudes.

4.4 The microwave system for spin-state excitation

For the determination of the g-factor, the electron spin has to be excited at its Larmor frequency, which amounts to approximately 105 GHz at the magnetic field of 3.76 T. The fundamental frequency is derived from the 10MHz reference, generated by the rubidium reference cell (SRS FS725), with a DDS[22] synthesizer (Anritsu MG3692B).

---

[22]Direct Digital Synthesis
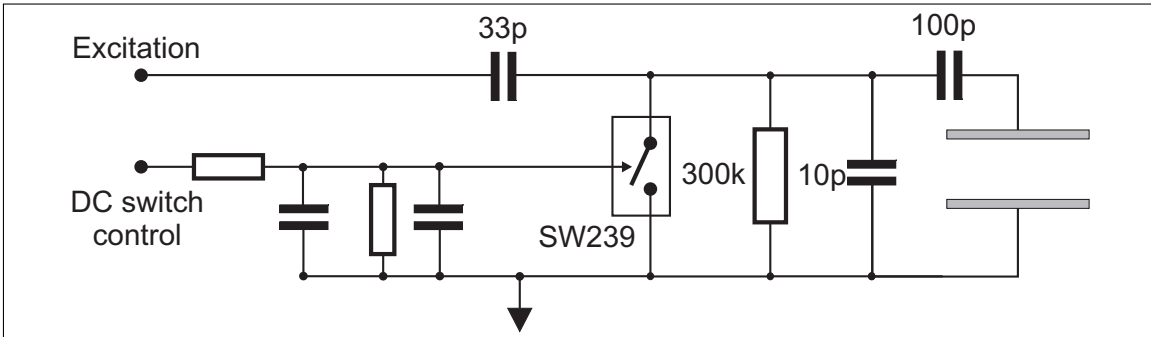
Figure 4.18: Implementation of the cryogenic solid state switches that short-out residual radiofrequency disturbances acting on the trap electrodes. The switches are based 4 SW239 integrated GaAs transistors connected in parallel to minimize the residual on-resistance.

The fundamental frequency of approximately 17.5 GHz is multiplied with an active nonlinear millimeter wave multiplier (OML S10MS) by a factor of 6. The active multiplier offers a maximum output power of 3 mW without degrading the relative frequency stability. After this multiplication the signal can only be transported by suitable (W-band) waveguides. The waveguides within the magnet bore are made from stainless steel in order to minimize the thermal conductivity from the 4 K to the room temperature region. Since stainless steel gives rise to severe power losses, it might be advantageous in the future to use waveguides coated with a thin gold layer[23]. With the present setup, the Rabi frequency for the incoherently driven spin-flip transition is about 30 s in the AT, which contributes considerably to the overall measurement duration. Since the spin-flip detection has been accelerated compared to predecessor experiments [34], the amount of data collected within a certain time could be easily improved by increasing the microwave power in the trap.

---

[23]Due to the skin effect, a few µm of gold at the surface suffices to reduce the losses considerably.

5. Experimental results

After introducing the theoretical foundation of the g-factor determination and the apparatus built for this measurement, the following chapter will focus on experimental methods and results that are important for the experiment. Many of the methods are common to precision Penning-trap experiments, however, in the course of this thesis a couple of novel ideas have been developed and implemented, which allowed the improvement of the measurement accuracy by more than an order of magnitude.

5.1 Creation and charge-breeding of ions

Since the triple trap setup is enclosed in a hermetically sealed vacuum chamber, the ions under investigation have to be created in the setup. As mentioned in chapter 4.2.1, a dedicated mini-EBIT setup [46] is available for this purpose. After charge-breeding with an electron current of typically several 100 nA for a couple of seconds, the CT is filled with a mixture of ions of different elements originating from the surface of the target electrode. Furthermore, all elements exist in different charge-states. Due to the electron energy of up to 8 keV in the current setup elements up to calcium can potentially be charge-bred to hydrogenlike ions [46]. For the g-factor determinations, mainly those nuclei without nuclear spin are interesting[1]. Furthermore, the mass of the ion has to be known with the same or preferably better precision than the g-factor experiment. Since it is envisaged to test the isotopic effect of the g-factor directly, the element should have at least two stable isotopes with significantly different mass. Combining these requirements, only a few elements remain. Among those is the element measured in the course of this thesis, $^{28}\text{Si}^{13+}$ and $^{30}\text{Si}^{13+}$, which will be addressed soon, $^{24,26}\text{Mg}^{11+}$, and $^{40,48}\text{Ca}^{19+}$. After the successful measurement of $^{28}\text{Si}^{13+}$, Mg became less interesting as candidate for a direct check

---

[1]It is planned to extend the g-factor experiment to ions with nuclear spin in order to determine high-precision nuclear magnetic moments. However, the appropriate experimental technique is not completely developed and goes beyond the scope of this thesis.

of the BS-QED. However, unlike ^{30}Si, the masses of both Mg isotopes have been measured by the SMILETRAP collaboration as hydrogenlike ions to good precision [67], enabling the direct determination of the isotopic effect with these elements. Calcium again is the element with the strongest binding field effect (among the available ions), promising the most stringent BS-QED test, provided that theoretical calculations can cope with the challenge of the requested accuracy [68], and features a 20% mass difference between different stable isotopes, which allows to test the isotope effect of the g-factor.

The already measured ^{12}C^{5+} is a very promising candidate for the determination of an improved value of the electron mass and will be remeasured with the improved precision obtained in this work.

5.2   Mass spectrum

After the charge-breeding process, the cloud of ions is adiabatically transported to the PT. Here, for the first time it is possible to take a meaningful glance at the composition of the cloud. Since the non-destructive image current detection as introduced in chapter 4.3 is the only possibility to detect ions in the g-factor experiment, also the creation of mass spectra relies on this technique. In order to be able to detect ions despite the strong space-charge interaction and distinguish between different ion species, the peak detection method for the axial frequency is used [37]. All ions are excited with a dipolar excitation and brought successively into resonance with the axial tank circuit by ramping the trapping voltage. Since the axial frequency is depending on the charge-to-mass ratio q/m, the voltage where the ion comes in resonance with the tank circuit is characteristic for the ion species, though there are ambiguities for isobars with very similar q/m ratios due to the very limited resolution of the mass spectrum.

For the creation of a mass spectrum the integrated power of the tank circuit is recorded with a custom-made detection amplifier, while the trapping voltage is ramped continuously from high voltages down to a minimum voltage. By applying a continuous axial dipolar excitation at a frequency slightly higher than the tank circuit, the ions coming into resonance have a high kinetic energy that is dumped onto the resonator. The spectrum is recorded by a digital oscilloscope which can be read out via GPIB. Figure 5.1 shows two exemplary mass spectra. The axial mass spectrum technique is a very simple and straightforward concept that nevertheless allows for the detection of large ion clouds as well as single ions within a short time. This allows the characterization of the charge-breeding process.

5.3   Preparation of single ions

After the creation of an ion cloud in the EBIS, the mass spectrum shows a large amount of ions of different species and charge states. Since for the final measurement only a single isolated ion should remain in the trap, it is necessary to implement an effective cleaning method that allows the selection of the ion of interest from a large number of contaminant ions. Different methods are used for this purpose and only
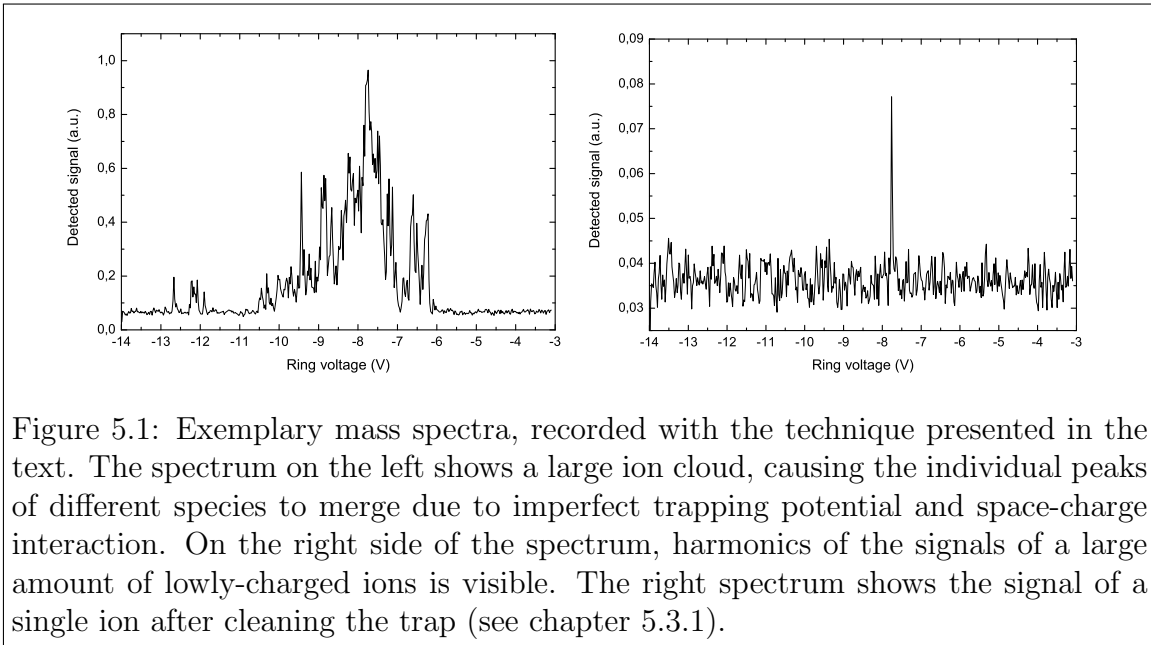
Figure 5.1: Exemplary mass spectra, recorded with the technique presented in the text. The spectrum on the left shows a large ion cloud, causing the individual peaks of different species to merge due to imperfect trapping potential and space-charge interaction. On the right side of the spectrum, harmonics of the signals of a large amount of lowly-charged ions is visible. The right spectrum shows the signal of a single ion after cleaning the trap (see chapter 5.3.1).

the two most effective ones are presented here. The preparation of single ions starts with the isolation of a single q/m range. For this purpose, all ions with charge-to-mass ratios other than the desired one are ejected from the trap. Two methods have proved their worth during the experiment.

5.3.1 SWIFT cleaning

The simplest method is the axial excitation of all ions until the unwanted ones get lost. Here, all ions except for the wanted ones are excited and reach accordingly large axial amplitudes. After a certain time the excitation is switched off and the trap voltage is lowered non-adiabatically to a minimum value. Ions with large axial energies are not bound anymore and leave the trap. For this purpose, an excitation signal originating from the inverse Fourier transform of white noise with notches at the magnetron and axial frequency of the wanted ion species is applied [69]. Additionally it turned out that the parametric excitation at the double axial frequency has to be avoided. This signal is stored in the RAM of a suitable signal generator (SRS DS345) and played back continuously. During the excitation, the wanted ions are brought into resonance with the tank circuit in order to dump excess energy from collisions with excited contaminant ions. After several iterations, only ions of the desired species remain in the trap. The SWIFT[2] cleaning is conceptually very simple. However, it has a fundamental drawback if a small amount of desired ions has to be extracted from a large ion cloud. Since the excited ions continuously oscillate through the cloud of selected ions, the energy transfer can be rather strong, especially if the amount of ions in the cloud is large enough such that space-charge effects dominate. Furthermore, the axial frequency is strongly dependent on the

---

[2]Stored Waveform Inverse Fourier Transform

motional radii. For this reason this method is virtually unusable for the selection of ions with very small abundances.

5.3.2   Selective magnetic trapping

For the unfortunate situation mentioned in the section above, a more advanced method was developed in the course of this thesis. It relies on the excitation of the cyclotron mode rather than the axial mode. Since the radial motion is two-dimensional, this has the advantage to decouple the motion of the excited and cold ions virtually entirely, which inhibits unwanted energy transfer to the wanted ions. Furthermore, the cyclotron frequency is far less sensitive to mode radii and space-charge than the axial frequency. An arbitrary number of species is selected by several chirped dipolar excitations in the PT, bringing these ions on large cyclotron radii. The cloud of ions is then transported to the AT. When the ions have arrived within the magnetic bottle of the AT and the axial energy is reduced via contact to the axial resonator, the electrostatic potential is switched off, leading to instantaneous axial loss of almost all ions. Only those ions that are on sufficiently large radii are still bound due to the magnetic moment of the cyclotron motion:

$$E_{\mathrm{mb}} \simeq \mu_z^{\mathrm{cycl}} B_2 z_{\mathrm{max}}^2 = q \frac{\omega_+}{2} r_+^2 B_2 z_{\mathrm{max}}^2. \tag{5.1}$$

The minimal cyclotron orbit necessary for successful magnetic trapping is given by the axial energy. For $^{28}\mathrm{Si}^{13+}$ ions in thermal equilibrium the minimum radius evaluates to

$$r_+ \geq \sqrt{\frac{2 k_B T_z}{q \omega_+ B_2 z_{\mathrm{max}}^2}} = 10 \,\mu\mathrm{m}, \tag{5.2}$$

when demanding a maximum axial amplitude of 1 mm, smaller than the typical dimension of the magnetic bottle. The selected ions can thereafter be transported back to the PT, where the cyclotron energy is dissipated via resonant sideband coupling to the axial resonator. This method allows a very effective selection of an ion species, especially in the presence of a large amount of contaminant ions.

5.4   Bolometric detection

5.4.1   Axial frequency detection and stability

As described in chapter 4.3, the detection of the eigenfrequencies is based on the detection of a dip in the thermal noise of the axial tank circuit. The determinability of the dip frequency is therefore of extraordinary importance for the success of the experiment. The line-splitting accuracy is dependent on the SNR of the detection system as well as the linewidth of the dip. For this reason, Monte Carlo simulations [70] were performed in order to determine the optimal averaging time for the specific setup. The variance of the fits to the Monte-Carlo data gives a model-free estimate for the performance of the line-splitting at these particular settings. As naively expected, the standard deviation of the determined frequency decreases with the

inverse square root of the averaging time and the SNR, and increases roughly linearly with the dip linewidth. The imperfect stability of both the trapping voltage and the magnetic field renders excessively long averaging durations, i.e. longer than about 100 s, undesirable. For this reason there are basically two possiblilies to optimize the final precision. Artificially increasing the temperature of the tank circuit with either externally applied white noise or a coherent SWIFT signal immediately increases the SNR of the detector with the square root of the effective temperature and accordingly also the precision of the frequency determination, as long as the particle motion stays sufficiently harmonic at the accordingly increased axial amplitude. However, the increased particle temperature leads to highly undesired systematic effects in the final g-factor determination such that there is a natural limit to the applicability of this technique, as outlined in chapter 6.1.4. When applying noise feedback to the resonator, the SNR increases linearly with the temperature, because also the effective resistance is scaled. This allows to reach the same SNR at a much lower temperature than possible with the excitation of the tank circuit. As a disadvantage the linewidth of the dip also scales with the feedback gain, strongly degrading the improvement due to the increased SNR. Figure 5.2 demonstrates that the most effective precision improvements are obtained by increasing the SNR with a less noisy amplifier and decreasing the linewidth by decoupling the ion from the tank circuit via a larger effective electrode distance. However, the latter possibility can have severe disadvantages when employing coherent detection methods that rely on the detection of a peak signal.

For this work an averaging duration of 90s was chosen to optimize the precision of the final free space cyclotron frequency. For the planned measurements with other species, this value should be adjusted accounting for the different linewidth due to the charge of these ions.
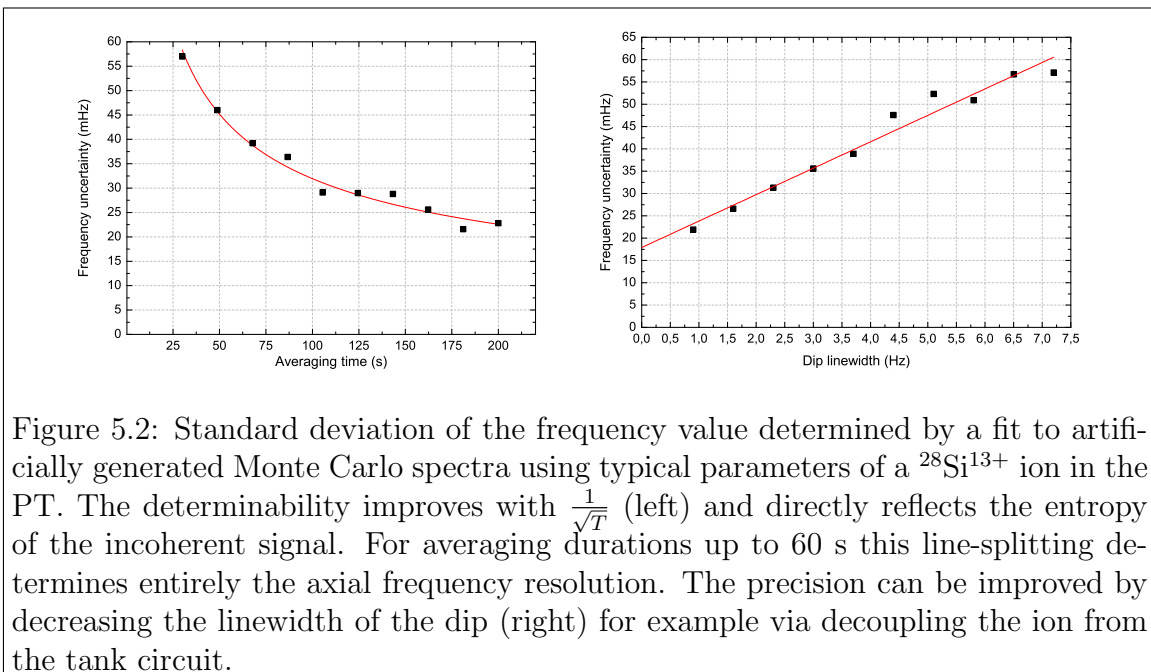
Figure 5.2: Standard deviation of the frequency value determined by a fit to artificially generated Monte Carlo spectra using typical parameters of a $^{28}\text{Si}^{13+}$ ion in the PT. The determinability improves with $\frac{1}{\sqrt{T}}$ (left) and directly reflects the entropy of the incoherent signal. For averaging durations up to 60 s this line-splitting determines entirely the axial frequency resolution. The precision can be improved by decreasing the linewidth of the dip (right) for example via decoupling the ion from the tank circuit.
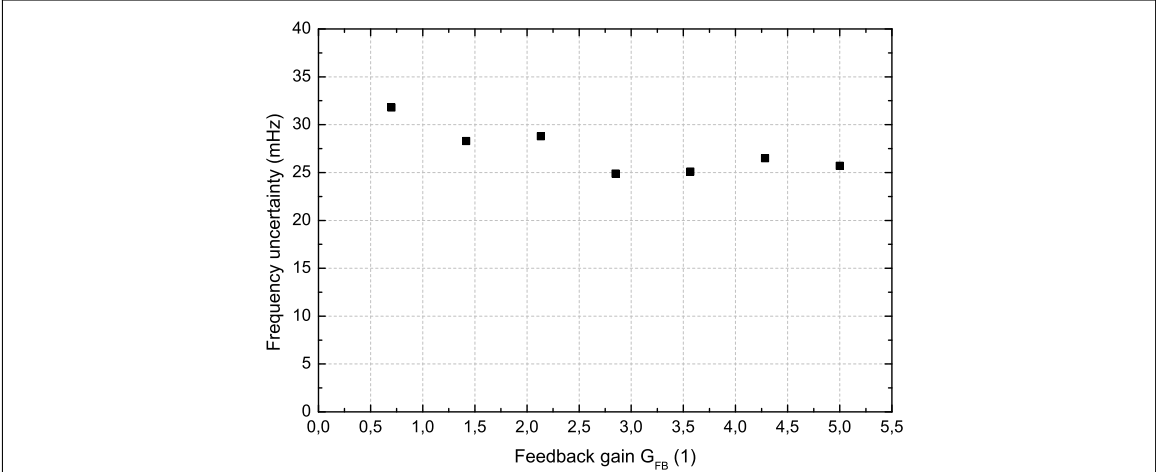
Figure 5.3: The linesplitting performance is roughly independent of the feedback gain, as the increase in the SNR is mostly canceled by the simultaneously increasing linewidth. This demonstrates that the particle can be cooled with noise feedback without sacrificing linesplitting precision.

5.4.2   Radial mode detection

The detection of the noise dip allows the determination of the axial eigenfrequency. The radial modes do not couple directly to the axial resonator and have to be detected with the sideband coupling method introduced in chapter 3.4.3. If the coupling between one of the radial eigenmodes and the axial motion is mediated by a suitable continuous wave (cw) quadrupolar radiofrequency drive at the sideband frequencies $\omega_{\rm rf} = \omega_+ - \omega_z$ or $\omega_{\rm rf} = \omega_z + \omega_-$, the sought-after eigenfrequency can be deduced from the dressed state frequencies [34] introduced in chapter 3.4.3. As a result of the periodic energy transfer between the modes, the amplitude of both modes is modulated with a beat frequency analogue to the Rabi frequency in quantum mechanical dressed states and the noise dip of the axial motion splits into two dips (see figure 3.7). This allows to extract the frequency information from the measurement of only the axial motion with a single detection system.

In general, the spectrum of the dressed state features two distinct noise dips at the frequencies

$$\omega_{r,l} = \omega_z \pm \Omega_2^{r,l} \quad \text{(see equation (3.76))}. \tag{5.3}$$

If the resonance criterium is not exactly met by the sideband coupling drive, the resulting double dip spectrum will not be perfectly symmetric about the original axial frequency but reproduce the classical analogon of the avoided crossing [34]. The difference of the modified dressed spectrum Rabi frequencies $\Omega_{1,2}^r - \Omega_{1,2}^l = \delta$ reproduces the detuning δ of the coupling drive. If the uncoupled eigenfrequency ω_z is measured independently, the sideband eigenfrequency can be deduced from the double dip frequency and the well-known coupling drive frequency $\omega_{\rm rf}$:

$$\omega_+ = \omega_r + \omega_l - \omega_z + \omega_{\rm rf}. \tag{5.4}$$

Since the modulation of the axial motion is complete, the axial frequency information cannot be deduced simultaneously from the same spectrum. If an adequate frequency stability can be assumed for the axial frequency, it is sufficient to measure the axial frequency before and after the double-dip spectrum. The linear interpolation between these frequencies yields a linear drift free measure of the axial frequency during the sideband measurement. This is very important since the important reduced cyclotron frequency is measured as an offset to the inherently less stable axial frequency. This is one the most severe disadvantages of the double-dip technique. When determining the cyclotron frequency, the final uncertainty for a 90 s measurement[3] can be estimated as:

$$\delta\nu_+ \simeq \sqrt{\delta\nu_r^2 + \delta\nu_l^2 + \delta\nu_z^2}. \tag{5.5}$$

Assuming that the frequency error on all frequencies is of purely statistical origin and independent, the uncertainty of the right and left dips is identical. Due to the smaller width of the double dip[4], the uncertainty of the two double dips (see figure 5.2) is accordingly lower than the one of the single dip. However, since two single dip spectra are recorded and the average of both determined frequencies is used, the final uncertainty of the calculated cyclotron frequency can be estimated as:

$$\delta\nu_+ \simeq \sqrt{2\,(0.8\,\delta\nu)^2 + \delta\nu^2/2} \simeq 1.3\,\delta\nu_z. \tag{5.6}$$

This relation shows quite plainly the dependence of the attainable cyclotron frequency resolution on the resolution of the axial frequency. The corresponding statistical uncertainty in the free space cyclotron frequency determined with the invariance theorem can now be calculated:

$$\delta\nu_c = \sqrt{\left(\frac{\nu_+}{\nu_c}\,1.3\,\delta\nu_z\right)^2 + \left(\frac{\nu_z}{\nu_c}\,\delta\nu_z\right)^2 + \left(\frac{\nu_-}{\nu_c}\,1.3\,\delta\nu_z\right)^2}. \tag{5.7}$$

When compared to the cyclotron frequency, the relative statistical precision of a single measurement is approximately

$$\frac{\delta\nu_+}{\nu_+} \simeq \frac{42\text{mHz}}{26.16\text{MHz}} \simeq 1.6 \cdot 10^{-9}. \tag{5.8}$$

This is the lower bound for the achievable single shot precision with a 90 s measurement. On top of this the magnetic field wander during the measurements degrades the achievable precision slightly. The final precision of the experiment gains about an order of magnitude from the fit to repeated measurements, allowing to extract the g-factor with a statistical precision of about $\frac{\delta g}{g} \simeq 2 \cdot 10^{-10}$ (see chapter 6.1).

5.4.3 Mode cooling and temperature measurement

The sideband coupling to the radial modes holds the possibility to transfer energy between the modes and with it to cool the radial modes into thermal equilibrium

---

[3]In fact, the complete measurement, including the two single dip spectra, takes 3·90 s.

[4]The occupation probability of the two states is approximately 50% each.

with the axial tank circuit. The temperature of the particle during the measurement determines many of the systematic errors in the frequency measurement as discussed in chapter 6.2.6 and is thus of prime importance for the g-factor experiment. Extensive optimization has been devoted to the task of reaching the lowest possible equilibrium temperature with the setup. The newly developed axial detection system has brought significant advances in this field and for the first time allowed to reach thermal equilibrium between the experiment lattice temperature set to ~ 4.2 K by the contact to the liquid helium bath and the ion temperature. Since the ion is in thermal equilibrium with the effective electron gas temperature, this means that there is no noticeable additional noise source acting on the resonator, leading to (almost) identical lattice and electron temperature. The large SNR of the detection system allows to further reduce this basis temperature below the equilibrium temperature. The significance of this development becomes evident in the calculation of the error budget of the experiment in chapter 6.2.6.

If the axial frequency is in resonance with the tank circuit, the axial energy will fluctuate on the time-scale defined by the cooling time constant τ. The expectation value of the axial energy will take a value

$$\langle E_z \rangle = k_B \, T_{tc}, \tag{5.9}$$

where T_{tc} denotes the temperature of the electron gas of the tank circuit. This expectation value can be interpreted as a temperature of the particle, in terms of the ergodic hypothesis. Although there is only one ion in the trap, the fluctuating energy will follow the Boltzmann distribution at the temperature T_{tc}, as long as the ion is in thermal contact with the resonator. In the instant the particle is decoupled from the tank circuit, the axial energy will stay at its instantaneous value. Repeated measurements of the energy will thus reflect a thermal distribution:

$$p(E_z) = \frac{1}{k_B \, T_z} \, e^{-\frac{E_z}{k_B \, T_z}} \, dE_z \tag{5.10}$$

By additionally coupling the axial and reduced cyclotron mode with a suitable cw quadrupolar drive at the sideband frequency, the cyclotron mode will experience a net cooling according to equation (3.79). Analogous to the axial motion, the cyclotron energy will take a random value after a finite coupling time, reproducing the thermal distribution of energies of the axial mode, transformed by the ratio $\frac{\nu_+}{\nu_-}$. If the process is repeated, the energy in the cyclotron mode will also reproduce a Boltzmann distribution with the scaled temperature $T_+ = \frac{\nu_+}{\nu_z} T_z$:

$$p(E_+) = \frac{\nu_z}{k_B \, \nu_+ \, T_z} \, e^{-\frac{E_+ \, \nu_z}{k_B \, \nu_+ \, T_z}} \, \mathrm{d}E_+. \tag{5.11}$$

In general the cyclotron mode will thus be hotter than the axial mode after sideband cooling, in the special case of the $^{28}\text{Si}^{13+}$ ion the ratio is approximately 40. For the magnetron motion, the equilibrium temperature is accordingly lower:

$$T_- = T_z \frac{\nu_-}{\nu_z} \simeq 64\,\text{mK}. \tag{5.12}$$

The large magnetic bottle of the AT offers the unique possibility to measure the energy in the radial modes very accurately making use of the well-defined dependence of the axial frequency on the radial mode amplitudes given by equation (3.26). The resolution in axial temperature, assuming a typical axial frequency readout jitter of 21 mHz (see chapter 5.4.1) is hence 6 mK or 0.6 µeV. By repeatedly coupling the axial and cyclotron mode and measuring the axial frequency, it is possible to plot the Boltzmann distribution of the axial and cyclotron energy. This opens the possibility to accurately measure the temperature of the axial mode in terms of the ergodic hypothesis. Given that the cyclotron energy remains constant during the adiabatic transport, it is even possible to monitor the temperature of the PT resonator, by sideband coupling in the PT and successive transport into the magnetic bottle. Figure 5.4 shows the result of this measurement. The determined temperature of $T_z^{\text{PT}} = 4.8(0.3)$ K is in good agreement with the lattice temperature of 4.2(1.0) K[5], which demonstrates the negligible back-action effect of the amplifier.

5.4.4   Information entropy cooling of the cyclotron mode

Without active sideband cooling, the cyclotron energy stays virtually constant, meaning that the measuring process which determines the current cyclotron energy extracts entropy from the particle. By simply stopping the coupling process when the energy is minimal, the cyclotron energy can be minimized far below thermal equilibrium with the axial motion. The attainable temperature is only limited by the available time (since the process is statistical) and the residual entropy arising from the contribution of the electrostatic field to the axial frequency stability. This technique is routinely used to limit the cyclotron energy to a maximum value in the AT prior to spin detection in order to minimize mode coupling dependent frequency shifts (see figure 5.5). If the trap electrode geometry allowed efficient coupling of the cyclotron and magnetron modes, the coherent oscillations between these uncooled modes would speed up this process significantly and thus allow for further cooling.

5.5   Novel cyclotron frequency measurement method (PnA)

When the new amplifier was constructed and tested and rendered measurements at far lower temperature than before possible, it became apparent that the statistical

---

[5]The temperature of the experiment is only directly measured close to the liquid helium dewar, the temperature at the position of the PT axial tank circuit will be slightly higher, but is only estimated from rough heat transport calculations.
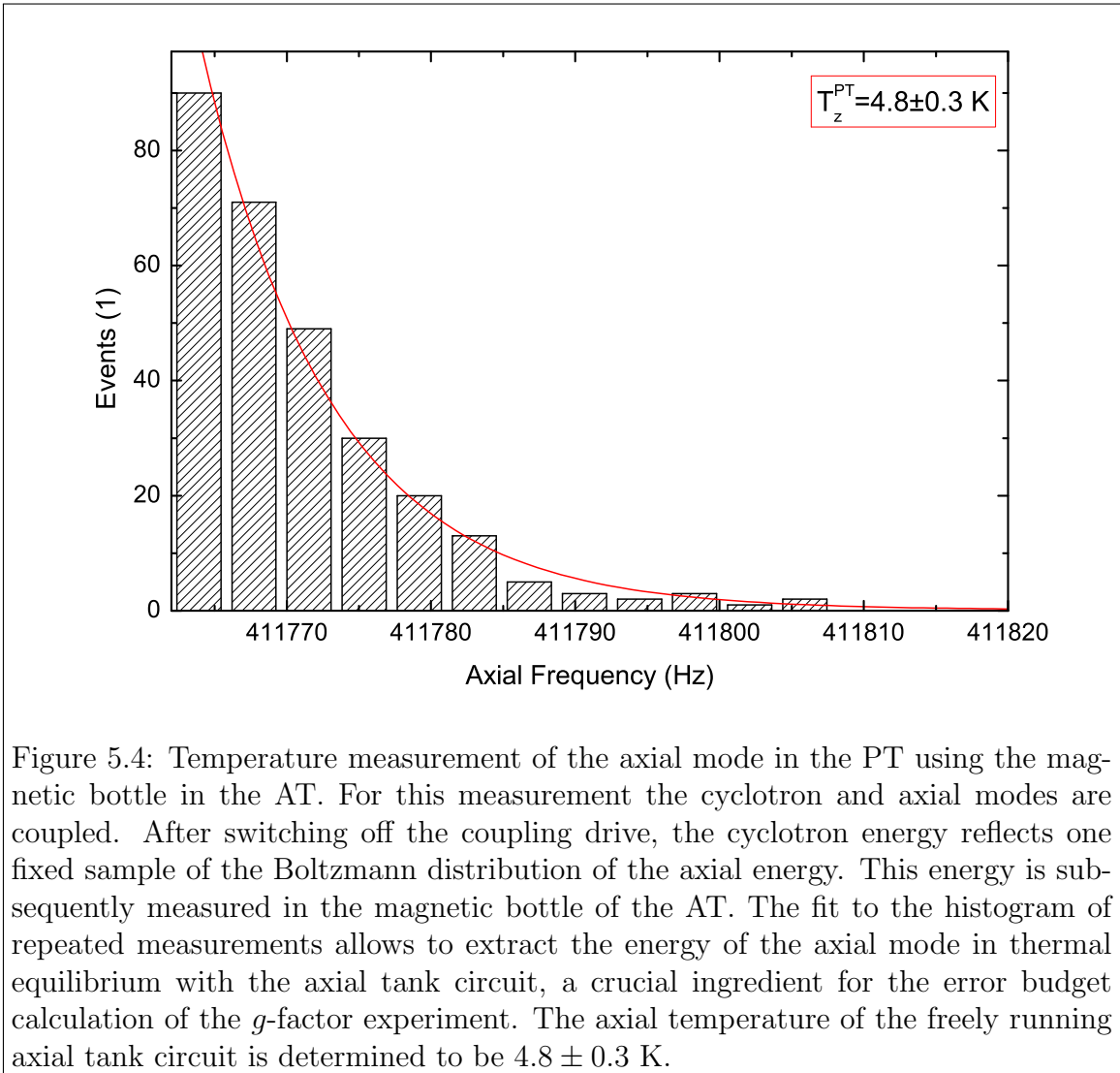
Figure 5.4: Temperature measurement of the axial mode in the PT using the magnetic bottle in the AT. For this measurement the cyclotron and axial modes are coupled. After switching off the coupling drive, the cyclotron energy reflects one fixed sample of the Boltzmann distribution of the axial energy. This energy is subsequently measured in the magnetic bottle of the AT. The fit to the histogram of repeated measurements allows to extract the energy of the axial mode in thermal equilibrium with the axial tank circuit, a crucial ingredient for the error budget calculation of the g-factor experiment. The axial temperature of the freely running axial tank circuit is determined to be 4.8 ± 0.3 K.

precision obtained with the double-dip technique would not suffice to fully exploit advantages of the decreased systematic uncertainties.

The development of a completely novel measurement technique within the course of this thesis [13] allowed improvement in the statistical precision, which is equivalent to a reduction of the necessary measurement time by a factor of roughly 450, while at the same time maintaining the same or better energy dependent systematic shifts. This development has culminated in the measurement of the g-factor of $^{28}\mathrm{Si}^{13+}$ to an accuracy of $\frac{\delta g}{g} = 4 \, 10^{-11}$ (see chapter 6.2). If combined with novel and advanced cooling methods that have been developed in this thesis (see chapter 7.1.2) this method sets the stage for intriguing experiments directly exploiting the quantum properties of these ultra cold ions and breaking the ppt accuracy barrier [71] for Penning-trap spectroscopy.

As discussed in chapter 5.4.1, the statistical precision of the cyclotron frequency determination is limited by the rather large linewidth of the dip that cannot be
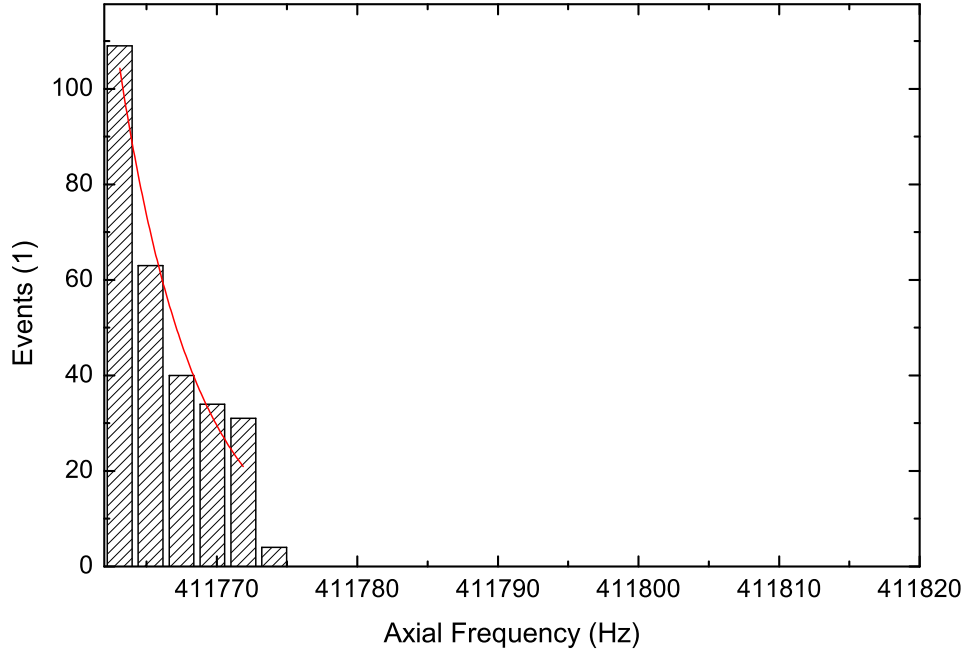
Figure 5.5: Energy distribution measurement of the axial mode in the AT after selecting low temperature ions. The distribution is clearly non-thermal, and the expectation value of the cyclotron energy is far below the equilibrium value. This procedure ensures a cyclotron energy below a defined cutoff value to allow efficient spin-state detection.

reduced arbitrarily without other inconveniences. The inherently long measurement time moreover increases the impact of magnetic field fluctuations on the measurement. Furthermore, the detection of the cyclotron frequency as an offset to the axial frequency significantly decreases the rejection of voltage fluctuations on the determined value of the free space cyclotron frequency. All these issues make the double-dip detection technique look unalluring for measurements with significantly improved precision. The next generation detection method should allow an exceptionally rapid frequency determination, while working at extraordinarily low temperature in order to minimize energy dependent systematic shifts.

5.5.1 Coherent detection

The relatively low information content of the dip line shape originates from the incoherent motion of the particle, driven by the likewise incoherent thermal noise of the tank circuit. Hence, not the ion motion itself, but rather the signature it leaves in the amplitude of the noise is regarded as the detected signal. In order to obtain a good estimate of this noise amplitude, it is necessary to average over extended time periods. The averaging procedure sums the uncorrelated noise and thus the SNR only increases with $\sqrt{T}$. The linewidth of the dip is defined by the cooling

time constant and does not decrease for longer observation times. In combination with the finite amplifier noise, the dip detection needs averaging times typically far beyond the Fourier detection limit.

This scaling behavior can be improved by detecting a coherent signal. For a coherent harmonic motion the amplitude and frequency are orthogonal informations and the linear evolution of the phase with time obviously allows to reconstruct the frequency. The phase-sensitive peak detection introduced within this thesis relies on the determination of the phase evolution of the particle motion within a well-defined time span. For this purpose an initial phase ϕ_{in} is imprinted on the particle motion by a suitable excitation. After a phase evolution time T_{evolv}, during which the particle is detached from the detection electronics, the final phase ϕ_{out} is extracted from the spectrum of the detected particle motion. If appropriate phase unwrapping can be applied[6], the frequency of the particle within the phase evolution period can be expressed as $\nu = \Delta\phi/\Delta T$. Assuming approximately normally distributed phase uncertainties[7], the statistical uncertainty of the frequency is given by:

$$\delta\nu = \frac{1}{T_{\mathrm{evolv}}}\sqrt{\delta\phi_{\mathrm{in}}^2 + \delta\phi_{\mathrm{out}}^2}. \tag{5.13}$$

Obviously the coherent detection shows a very favorable scaling behavior with respect to the measurement duration when compared with the noise dip detection technique. The frequency uncertainty has contributions from both the phase definition ($\delta\phi_{\mathrm{in}}$) and the phase readout ($\delta\phi_{\mathrm{out}}$). Depending on the implementation of the phase initialization and determination, the statistical uncertainty of such measurements can approach very low values.

5.5.2 Previous state of the art: PnP

Phase sensitive cyclotron frequency measurements have already been shown with the well-established PnP[8] technique, introduced by Eric Cornell et al. [72] at the Massachusetts Institute of Technology. Here, the cyclotron motion is brought to a defined amplitude and phase by a short resonant dipolar rf excitation. After a well-defined period, allowing the cyclotron phase to freely evolve according to to the particle's eigenfrequency, the classical action of the cyclotron and the axial mode are exchanged by a suitable π-pulse and a peak appearing on the axial resonator is recorded. From the spectrum of the detected signal the cyclotron phase after the evolution period can be deduced (see figure 5.6).

However this method relies on the excitation of the cyclotron mode to quite large energy, sufficient for the ion signal to overcome the Johnson noise of the axial tank

---

[6]The phase can only be read out ambiguously within the interval $[0, 2\pi]$. For successful frequency determination this ambiguity has to be removed by appropriate additional measurements. This process is commonly called phase unwrapping.

[7]A more careful analysis later will show that this assumption is strictly speaking not true, but for practical cases sufficiently good.

[8]The abbreviation stands for Pulse 'N' Phase, a graphic paraphrase of the method.

circuit (after appropriate transfer of the phase and amplitude information from the cyclotron mode to the axial mode via the π-pulse). This imposes a severe fundamental limitation to the attainable accuracy [72], as the cyclotron energy during the measurement period gives rise to systematic frequency shifts that can be corrected for only partially. Furthermore, due to the limited reproducibility of the cyclotron amplitude, this frequency shift will jitter between successive measurements, severely limiting the statistical precision. Still, the statistical precision obtained with the PnP technique is impressive and makes phase sensitive measurements an attractive prospect, provided that a method is found that allows to use significantly lower cyclotron amplitudes during the measurement period while still enabling a phase readout with sufficient precision.
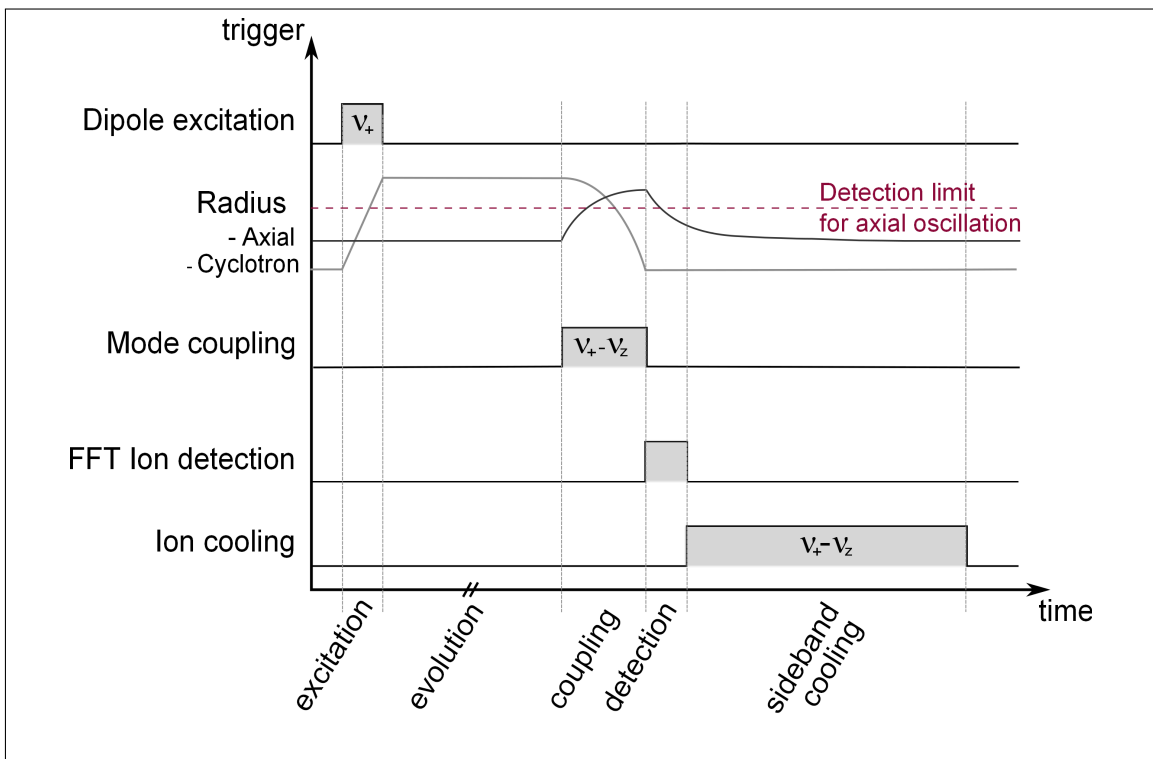
Figure 5.6: Pulse diagram for the PnP cyclotron frequency detection technique. The phase is defined with a resonant pulse on the eigenfrequency of the previously cooled ion and the phase is read out by swapping the information coherently into the axial mode after a well-defined phase evolution period. The initial cyclotron amplitude has to be sufficiently large to allow the resulting axial signal to overcome the thermal noise of the detection system.

5.5.3 Low energy coherent detection: PnA

The novel measurement method, called PnA[9] in the following, allows to read out the phase of the particle motion in the dark, i.e. without the need to detect the

---

[9]In analogy to the PnP technique, this acronym stands for Pulse 'N' Amplify.

motion. This allows to keep the cyclotron amplitude arbitrarily small during the measurement, a key improvement over previous techniques. Instead of directly detecting the motion, the amplitude is amplified by an arbitrary factor while retaining the phase information. With the amplification process the SNR of the signal can be set to arbitrary values. The phase determination precision $\delta\phi_{\text{out}}$ is then not limited anymore by the detection system but solely by the amplification process, allowing to detect the phase of the cyclotron motion at far lower amplitudes (see figure 5.7). With this readout technique, the amplitude during the phase evolution time can be chosen independently of the detection system. In fact, the amplitude has to be only large enough to guarantee that the jitter of the initial phase is sufficiently low. The two methods used in this experiment to define the initial phase are the direct dipolar excitation and the squeezing of the initial thermal distribution, both discussed in chapter 3.4. Although the squeezing technique shows superior performance, both methods rely on an initially cold ion. By cooling the ion to the quantum mechanical motional ground-state, the first excited levels suffice to define the phase. The PnA method then allows to coherently read out the phase of this state. In chapter 7.1 some of the exciting prospects of this technique are discussed.

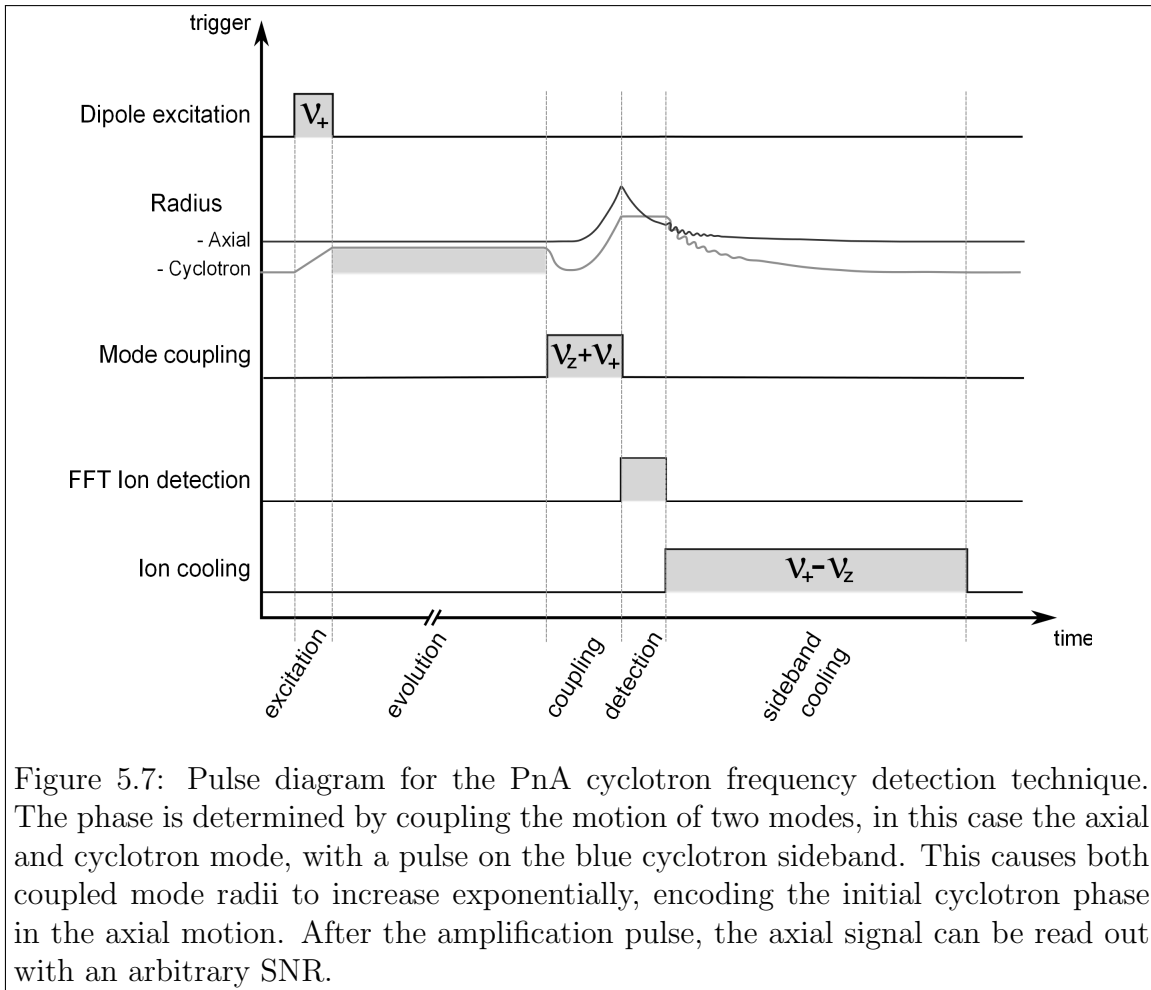Figure 5.7: Pulse diagram for the PnA cyclotron frequency detection technique. The phase is determined by coupling the motion of two modes, in this case the axial and cyclotron mode, with a pulse on the blue cyclotron sideband. This causes both coupled mode radii to increase exponentially, encoding the initial cyclotron phase in the axial motion. After the amplification pulse, the axial signal can be read out with an arbitrary SNR.

5.5.3.1 Implementation of the PnA method

For the first proof-of-principle measurement, the cyclotron motion was cooled by sideband-coupling to the axial detector. By using negative feedback for the axial detector, a cyclotron temperature of roughly 74 K is achievable in the current apparatus.

After cooling the ion, the cyclotron phase is defined with a resonant radiofrequency
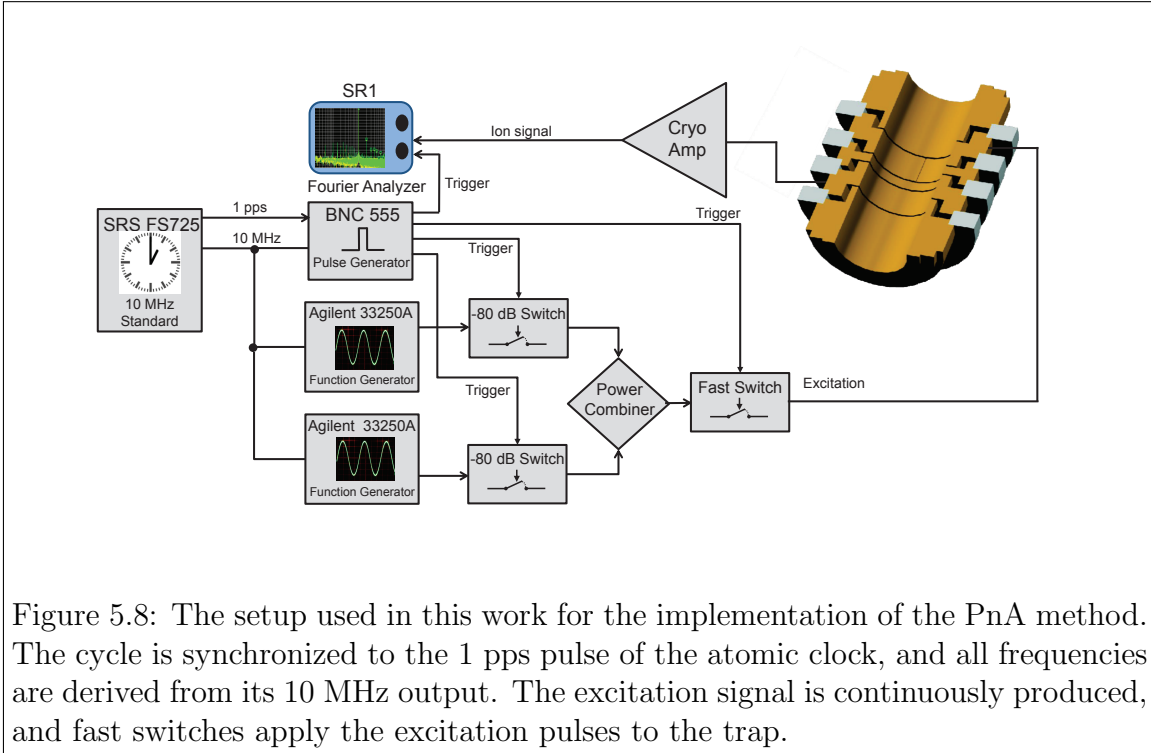
Figure 5.8: The setup used in this work for the implementation of the PnA method. The cycle is synchronized to the 1 pps pulse of the atomic clock, and all frequencies are derived from its 10 MHz output. The excitation signal is continuously produced, and fast switches apply the excitation pulses to the trap.

pulse at the expected reduced cyclotron frequency (ν_{dip}), applied to the split correction electrode. This pulse is generated by an Agilent 33250A arbitrary function generator (AFG). After a well-defined waiting period the amplification pulse at the blue cyclotron sideband (ν_{quad}) is introduced from a second AFG and finally the SR1 Spectrum Analyzer is triggered and starts recording the resultant axial signal.

All generated frequencies and pulses are referenced to a commercial rubidium cell atomic reference clock from Stanford Research Instruments (FS725), which generates a 10 MHz synchronization signal and additionally provides an output with exactly 1 pulse per second (1pps). This is particularly important for the phase sensitive detection, since any tiny time base difference between the function generators would cause the relative phase between the excitation signals to diverge unacceptably. The pulses and triggers are derived from this reference signal by a BNC555 pulse delay generator.

The phase stability of the excitation pulses is absolutely critical for the finally achievable precision. Unfortunately, the jitter of the delay between a TTL trigger pulse from the BNC555 and the start of a signal burst from the AFG (specified to 1 ns$_{\mathrm{rms}}$

in the 33250A datasheet) would cause excess phase noise, significantly compromising the achievable phase stability of the measurement:

$$\delta\phi \geq \sqrt{2} \cdot 360° \cdot \nu_+ \cdot 1\text{ns} \simeq 13°. \tag{5.14}$$

For this reason, the AFG run continuously and the pulses are generated by self developed fast analog switches after the AFG [73]. All excitation frequencies are rounded off to 1 Hz steps and the measurement process is triggered by the 1 pps pulse from the atomic clock. This way, at the beginning of each measurement cycle the phases of the excitation signals are constant. The jitter of the pulse length and timing now only affects the frequency difference between the excitation pulses ($\nu_{\text{quad}} - \nu_{\text{dip}} \simeq \nu_z$). The resulting technical phase jitter is negligible at the current measurement precision. The SR1 function generator is also locked to the 10 MHz reference[10] and is thus able to determine the signal phase in the same reference frame. As a disadvantage of this method the excitation frequencies are continuously generated, even in the free phase evolution period. This causes unwanted excitation especially for the ν_+ excitation if the ion's reduced cyclotron frequency happens to be in close resonance with the excitation. Great care has been taken in the design of the electronic analog switches and the connection to the trap system to prevent the signal to enter the trap. This is a surprisingly complicated task, since the signal generator causes measurable excitation of the ion once it is switched on, even if it is not connected to the trap at all.

  A complete measurement with this method typically consists of several such cycles, each with different evolution periods. From the slope of the measured and unwrapped phases the eigenfrequency can finally be determined. In fact, only the shortest and longest evolution periods are used for the frequency determination, the other measurements are only used for the phase unwrapping procedure. The shortest period is almost insensitive to the ion frequency and is measured repeatedly to decrease the statistic noise. The frequency information is thus extracted entirely from the longest measurement period. Hence, the microwave excitation that probes the spin transition can be applied exactly simultaneously to the phase evolution, such that the cyclotron frequency and the Larmor frequency are determined at exactly the same time. To simplify the phase unwrapping procedure, a double dip is measured before the PnA process is started to provide a decent initial guess of the current cyclotron frequency. The maximum evolution period is bounded by the stability of the magnetic field. In order to unambiguously determine the phase, the phase jitter between successive measurements should be sufficiently small to make 2π jumps adequately unlikely. In the current setup, a phase evolution up to 10 s typically still shows sufficiently low error rate.

5.5.3.2 Frequency uncertainty of the PnA method

In order to discuss the performance of the PnA method, it is necessary to distinguish between technical readout noise, generated by the measurement process, and jitter

---

[10]This is a rather unusual feature for FFT analyzers and was in fact one of the main reasons for choosing this device.
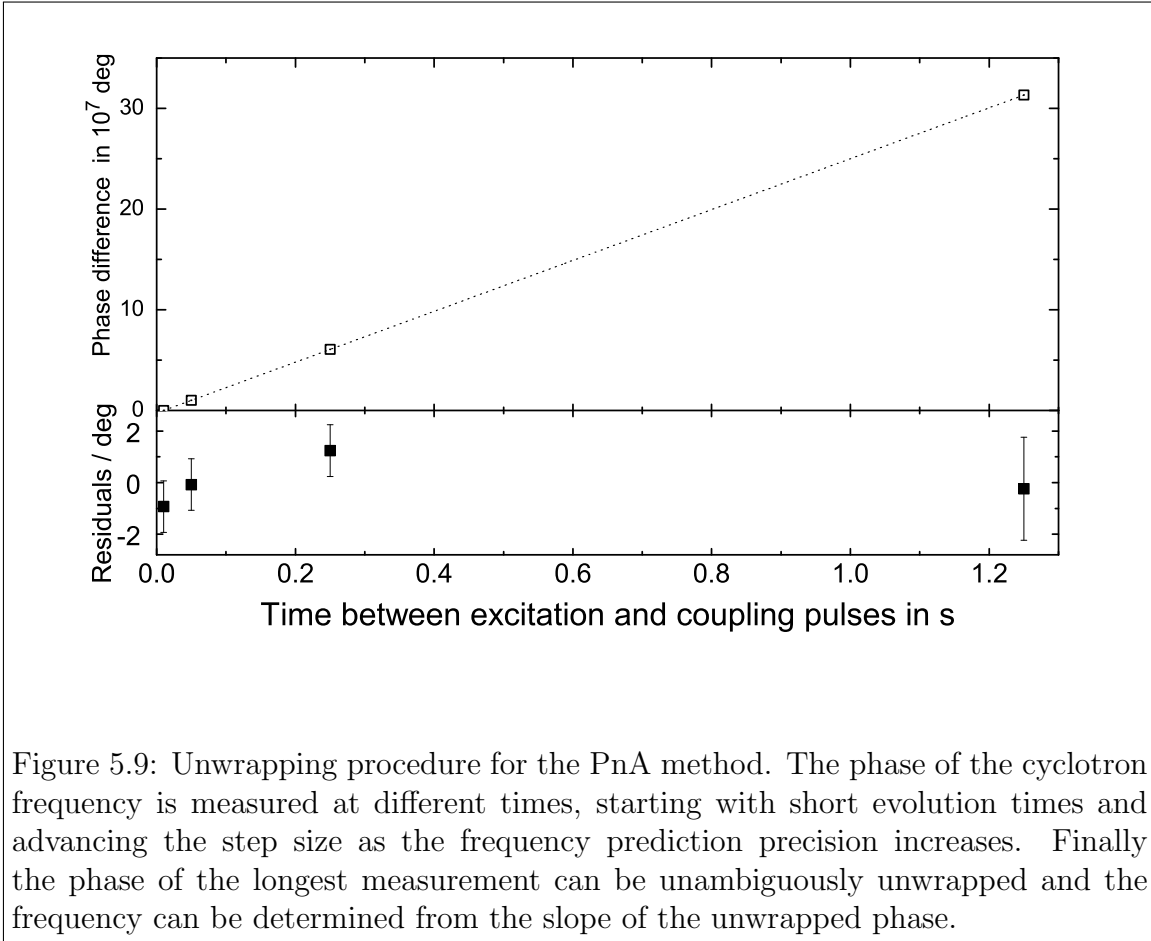
Figure 5.9: Unwrapping procedure for the PnA method. The phase of the cyclotron frequency is measured at different times, starting with short evolution times and advancing the step size as the frequency prediction precision increases. Finally the phase of the longest measurement can be unambiguously unwrapped and the frequency can be determined from the slope of the unwrapped phase.

of the measured eigenfrequency that is not related to the measurement method but given by the stability of the trapping fields, mainly the magnetic field. For reasonable settings the technical noise of the PnA method is dominated by the jitter of the initial phase. The repeatability of the phase definition is limited by the ratio of excited to cooled ion energy, as shown in figure 3.6. By increasing the excited energy level, the phase definition jitter decreases, but the unwanted systematic shift of the eigenfrequency due to the magnetic inhomogeneity and the relativistic mass increase finally sets a limit to the available energy. Decreasing the initial temperature is a more appealing option. For the current setup, not using the advantageous cooling with the cyclotron resonator[11], figure 5.12 shows the attainable phase stability. When choosing an excitation energy equivalent to a $3 \cdot 10^{-11}$ relative relativistic mass shift, a phase stability of roughly $14°$ can be achieved, resulting in a relative frequency jitter for a $^{28}\mathrm{Si}^{13+}$ ion of

$$\frac{\delta\nu_+}{\nu_+} = \frac{\delta\phi}{360°\nu_+ T_{\mathrm{evolv}}} \simeq 1.5 \cdot 10^{-9} \frac{s}{T_{\mathrm{evolv}}}, \tag{5.15}$$

---

[11]At the time of the measurement the cyclotron resonator was detuned from the cyclotron frequency of $^{28}\mathrm{Si}^{13+}$ by several linewidths due to technical reasons.

or $1.5 \cdot 10^{-10}$ for a 10 s measurement. This can be compared to the technical jitter of the double-dip technique that can be estimated to

$$\frac{\delta \nu_+}{\nu_+} = \simeq 1.5 \cdot 10^{-8} \sqrt{\frac{s}{T}}, \tag{5.16}$$

or $4.8 \cdot 10^{-9}$ for a 10 s measurement[12]. For longer measurement times the advantage of the PnA method increases, and for a 90 s measurement the frequency determinability is a factor of 95 better than with the double-dip technique. Figure 5.10 shows a measurement of the achieved frequency stability, demonstrating an order of magnitude improvement compared to the traditional double-dip technique. On
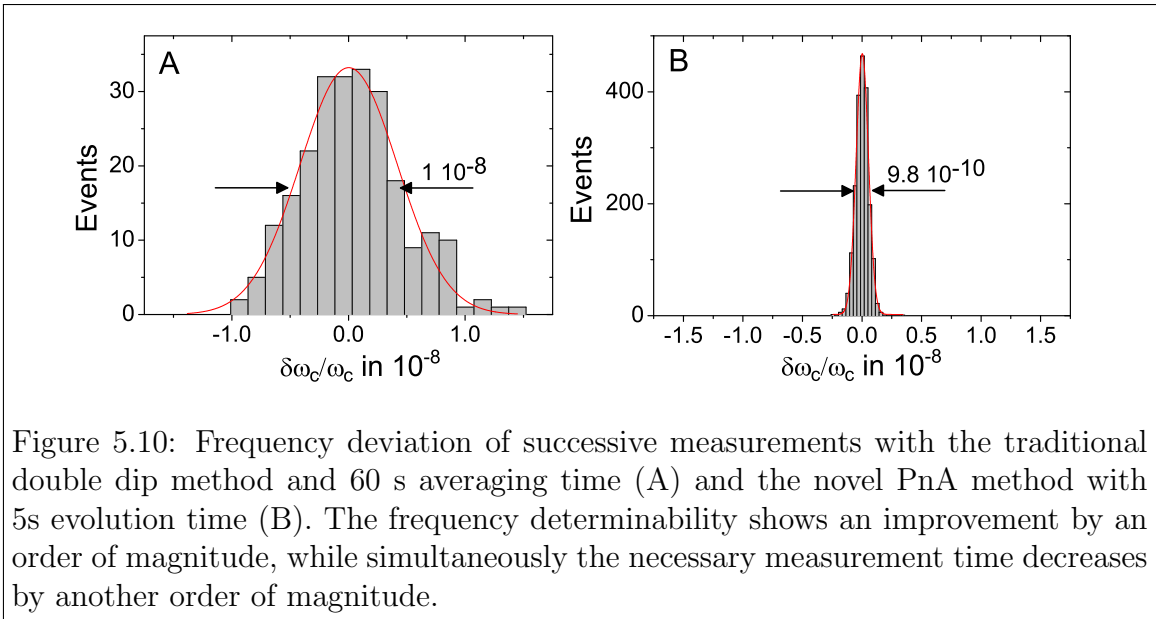
Figure 5.10: Frequency deviation of successive measurements with the traditional double dip method and 60 s averaging time (A) and the novel PnA method with 5s evolution time (B). The frequency determinability shows an improvement by an order of magnitude, while simultaneously the necessary measurement time decreases by another order of magnitude.

top of the technical frequency readout jitter the magnetic field changes during the measurement time and between two successive measurements. This magnetic field drifts cannot be improved with the measurement method, but the necessary detection time can be decreased, allowing the measurement in a more favorable interval. Figure 5.11 shows the measured time averaged Allan standard deviation [74] of the magnetic field measured with the PnA method. However, the Allan deviation plot is somewhat misleading, since it only gives an indication of the stability of the mean cyclotron frequency. The Larmor frequency determination employed in this experiment however shows a nonlinear averaging behavior, leading to imperfect cancellation of the magnetic field wander during one measurement. This effect makes shorter measurement periods, which are inaccessible by the double-dip technique, even more preferable.

---

[12]In fact a 10 s measurement does not allow to reliably fit the double dip.

Figure 5.11: Overlapping time averaged Allan standard deviation for the magnetic field measured with the PnA method. For comparison the predicted line-splitting accuracy of the double-dip technique is added. The PnA shows superior performance over the complete span of measurement periods.
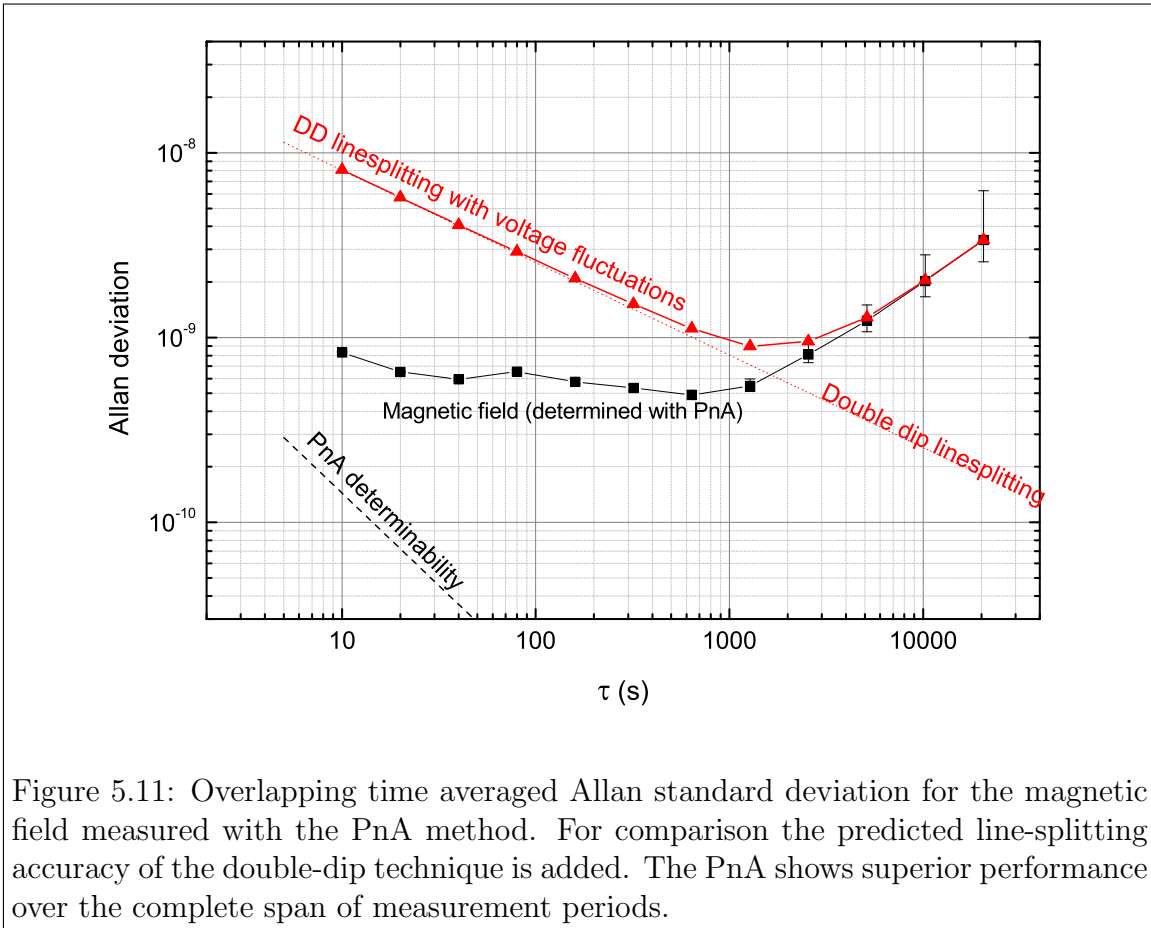
5.6 Magnetic field measurement

The two main observables of the experiment, the Larmor frequency of the electron and the cyclotron frequency of the ion are defined both by the externally applied magnetic field of the superconducting magnet. It is hence of great importance to keep this field virtually perfectly stable over the measurement period and to know at least the leading order corrections to the homogeneity of the magnetic field. Fortunately, it is conveniently possible to measure both quantities with the trapped ion.

5.6.1 Measurement of the field inhomogeneities

Since the magnetic field is tuned to be almost perfectly homogeneous and the ion is cooled to very small radii during the measurement, the first two orders of the series expansion, B_1 and B_2, are sufficient for the accurate determination of the systematic shifts arising from the magnetic field inhomogeneities in the PT. In the AT, the knowledge of the strength of the magnetic bottle contribution furthermore enables the accurate energy calibration and measurement as shown in chapter 5.4.3. Here, the B_2 contribution is dominated entirely by the effect of the ferromagnetic ring electrode. For this reason, the strength of the magnetic bottle can be accu-
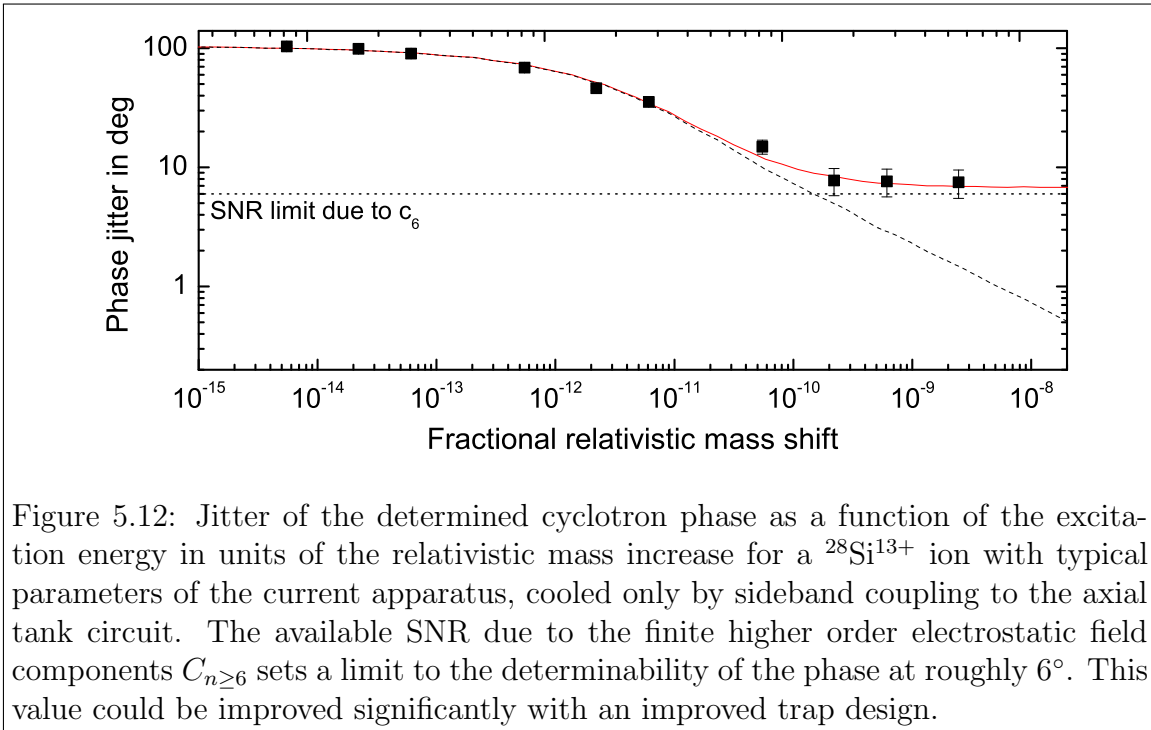
Figure 5.12: Jitter of the determined cyclotron phase as a function of the excitation energy in units of the relativistic mass increase for a $^{28}\text{Si}^{13+}$ ion with typical parameters of the current apparatus, cooled only by sideband coupling to the axial tank circuit. The available SNR due to the finite higher order electrostatic field components $C_{n\geq6}$ sets a limit to the determinability of the phase at roughly 6°. This value could be improved significantly with an improved trap design.

rately predicted, limited only by the knowledge of the material parameters[13] and machining precision (see figure 5.13). In the PT however, the residual contribution of the ferromagnetic ring is very small compared to inhomogeneities caused by other magnetic materials in the magnet bore and the initial homogeneity of the magnet.

In both traps the field inhomogeneity can be determined by displacing the trapped ion along the axial direction with help of the electrostatic trapping potential [37]. The electrostatic potential contributions of the electrodes can be extracted e.g. from the numerical solution of the trapping field as introduced in chapter 4.2.2. Small offset voltages that are asymmetric with respect to the ring electrode allow to shift the mean axial ion position with nm resolution. By measuring the free cyclotron frequency at each position, the magnetic field shape can be scanned around the equilibrium position of the ion. With a simple polynomial fit the field contributions can finally be determined. Figure 5.14 shows such a measurement for the magnetic field in the PT, a similar measurement can be found in the Ph.D. thesis of Birgit Schabinger [46] for the strength of the magnetic bottle. The precision of the determination is limited however by the inevitable temporal variations of the magnetic field between successive measurement steps. In chapter 6.2.6 a more precise method for the determination of the B_2 component is presented, giving congruent results with smaller uncertainty. However, the direct measurement of the axial magnetic field has the advantage of being model-free.

---

[13]The saturation magnetization of nickel of 0.645 T was taken from [44].
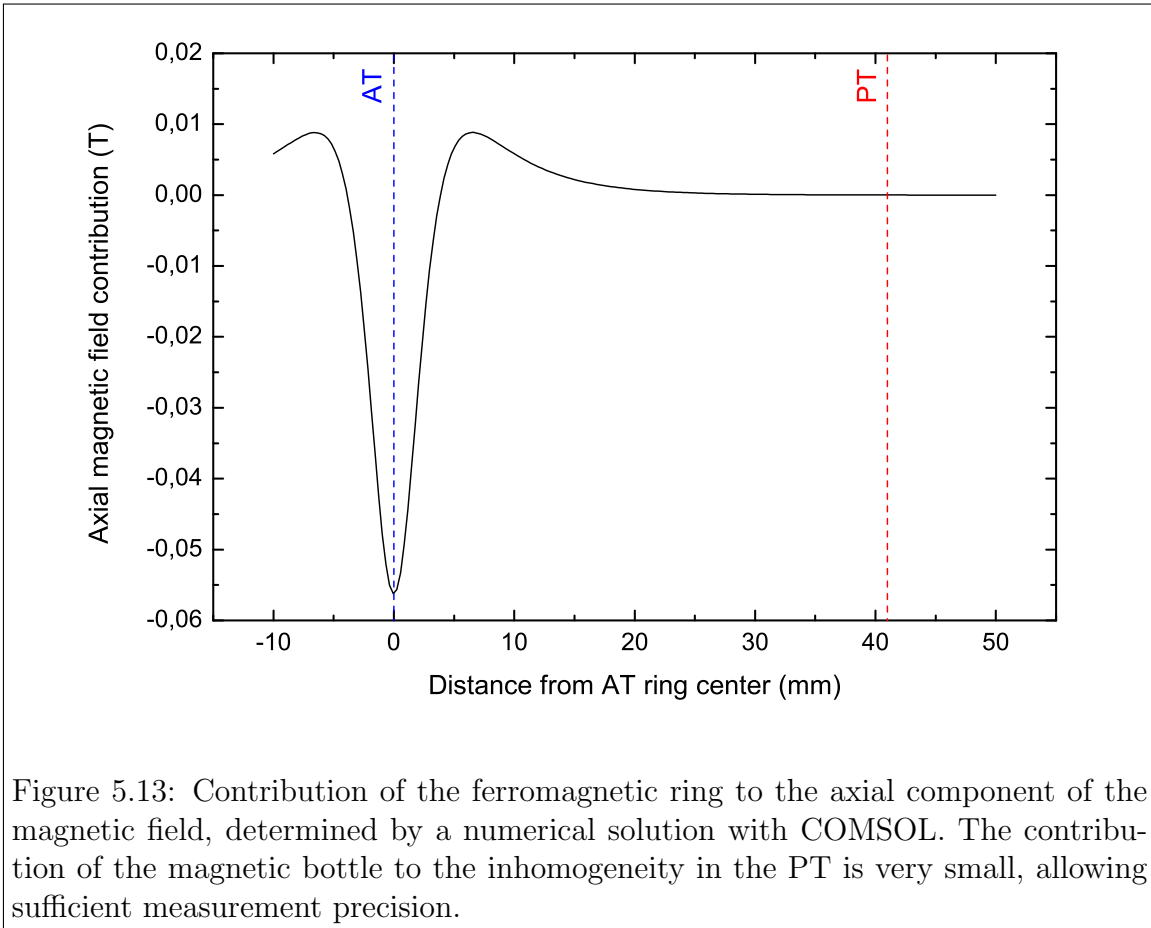
Figure 5.13: Contribution of the ferromagnetic ring to the axial component of the magnetic field, determined by a numerical solution with COMSOL. The contribution of the magnetic bottle to the inhomogeneity in the PT is very small, allowing sufficient measurement precision.

5.7   Spin-state detection

The g-factor determination technique employed in the experiment crucially requires the ability to unambiguously detect the spin state of the electron bound to the trapped ion. Within the magnetic bottle field of the analysis trap, the spin state manifests as a change of the axial frequency by 240 mHz (see chapter 3.2.2.2), a relative difference of only $6 \cdot 10^{-7}$. For an unambiguous detection of the spin state with an error rate of less than 5%, a stability of the determined axial frequency of better than $\delta\nu_z \leq 58$ mHz is required, corresponding to a relative frequency jitter of only $1.4 \cdot 10^{-7}$. This requirement proved to be hard to meet, since it requires the cyclotron mode amplitude to remain extremely stable over the timescale of the axial frequency measurement and the microwave excitation. In the course of this thesis the two main sources of instability could finally be identified and eliminated, allowing the successful detection of spin flips in $^{28}Si^{13+}$. The electrostatic field errors have been diminished by more careful surface preparation of the electrodes, combined with a high-voltage reflector with improved geometry which reduced the amount of charges impinging on the electrodes, as discussed in chapter 4.2.3. Over and above, cryogenic solid state switches drastically reduced the amount of radiofrequency disturbances which would cause highly undesired cyclotron energy fluctuations.
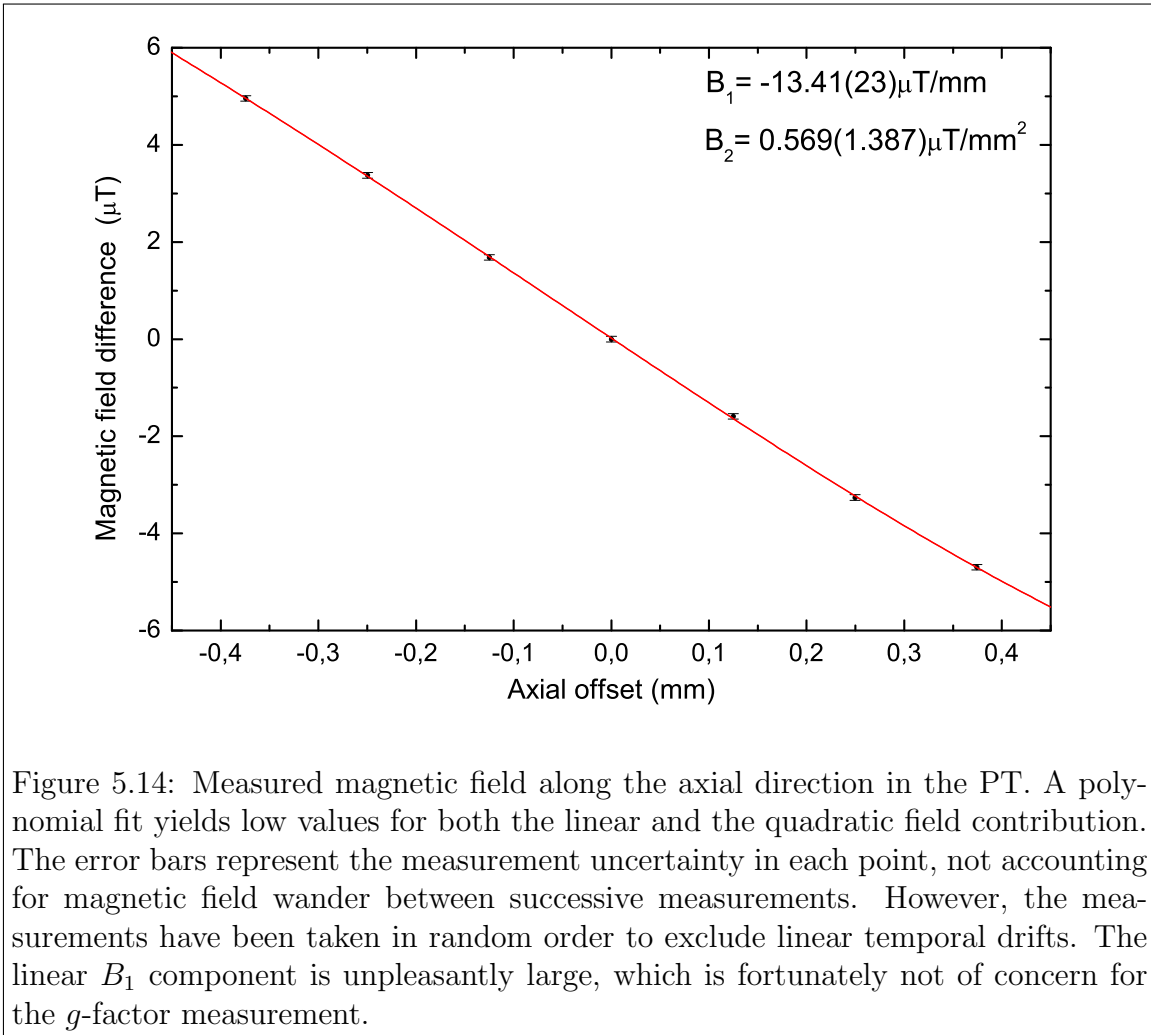
Figure 5.14: Measured magnetic field along the axial direction in the PT. A polynomial fit yields low values for both the linear and the quadratic field contribution. The error bars represent the measurement uncertainty in each point, not accounting for magnetic field wander between successive measurements. However, the measurements have been taken in random order to exclude linear temporal drifts. The linear B_1 component is unpleasantly large, which is fortunately not of concern for the g-factor measurement.

With these developments, combined with the phase-sensitive detection technique, the way towards successful spin-state detection was finally cleared.

5.7.1 Phase sensitive axial frequency measurement

For the detection of the spin state, it is necessary to resolve tiny frequency differences, rather than provide an accurate measurement of the absolute axial frequency. The frequency determination via the noise-dip technique is thus not ideally suited for this purpose, as it pays for the low systematic shifts with a poor SNR, resulting in the necessity of long averaging times. The axial frequency is hence monitored with a phase sensitive technique, as originally proposed by S. Stahl [75] for this purpose, which provides a far superior performance for the detection of small frequency differences.

For the phase-sensitive technique the ion is initially excited to rather large amplitudes with a pulsed dipolar excitation at roughly the axial eigenfrequency. Subsequently the axial resonator is shifted out of resonance with the ion with a 180° electronic feedback loop, resulting in a negligible axial damping. This allows to

let the axial motion and phase evolve from its initial value, according to the true eigenfrequency for about a second. The final phase after a well-defined evolution time is eventually determined from the FFT spectrum recorded by switching the axial resonator back to the original frequency. The peak appearing superimposed onto the Johnson noise of the resonator contains the coherent phase information of the ion motion and thus allows to determine the axial frequency. This procedure is outlined in figure 5.15. Assuming a SNR of 20 dB, which is simple to achieve with
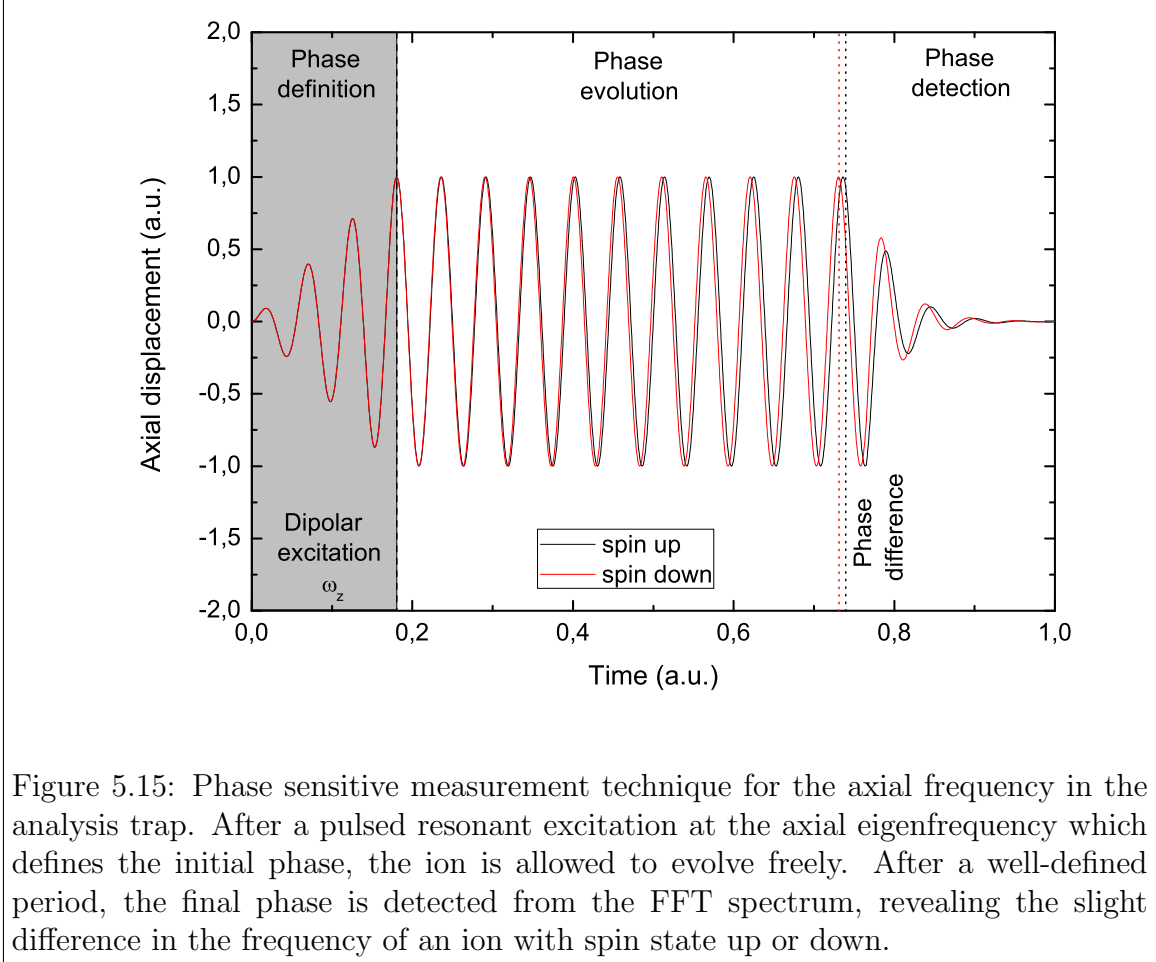
Figure 5.15: Phase sensitive measurement technique for the axial frequency in the analysis trap. After a pulsed resonant excitation at the axial eigenfrequency which defines the initial phase, the ion is allowed to evolve freely. After a well-defined period, the final phase is detected from the FFT spectrum, revealing the slight difference in the frequency of an ion with spin state up or down.

highly charged ions, the determinability of the axial phase is roughly

$$\delta\phi \simeq \frac{1}{\sqrt{2}\,\mathrm{SNR}}.$$

(5.17)

Since the systematic shift of the axial frequency is of minor concern, the phase definition uncertainty is typically negligible due to high excitation energies. For a typical 800 ms measurement period, the frequency resolution with the phase sensitive technique can be calculated:

$$\delta\nu_z = \frac{1}{\sqrt{2}\,\mathrm{SNR}\,2\pi\,T_{\mathrm{meas}}} \simeq 25\mathrm{mHz}.$$

(5.18)

Comparing this to the typically 90 s averaging time necessary to achieve a similar frequency uncertainty with the noise dip gives a good impression of the performance gain of a coherent frequency measurement. If the cryogenic amplifier features sufficiently low input noise, as in this experiment, the peak can be monitored online during the phase evolution period, while the resonator is detuned. Since the SNR scales with the available measurement time as the bin width of the FFT decreases, this allows the ultimate frequency determination performance, limited only by the Cramér-Rao information bounds [65]. This means there is no better method for the estimation of the frequency possible at this specific SNR. The SNR itself can however not be increased arbitrarily, since the increasing axial amplitude introduces excessive systematic frequency shifts and jitter, as the ion leaves the harmonic region of the trap. By deliberately introducing finite C_4 and C_6 components of the electrostatic field, a specific large amplitude can be found where the frequency becomes independent of the amplitude to first order. In this region the frequency jitter is small, while the SNR can be very large. This method might be advantageous for lowly charged particles, however, it was not routinely applied in this experiment due to the excessive setup complexity.

Figure 5.16 shows the attainable frequency stability in the analysis trap and a series of clearly visible spin quantum jumps of the electron bound to the trapped ion. With this frequency stability, spinflips that are induced with resonant microwave excitation can be readily identified.
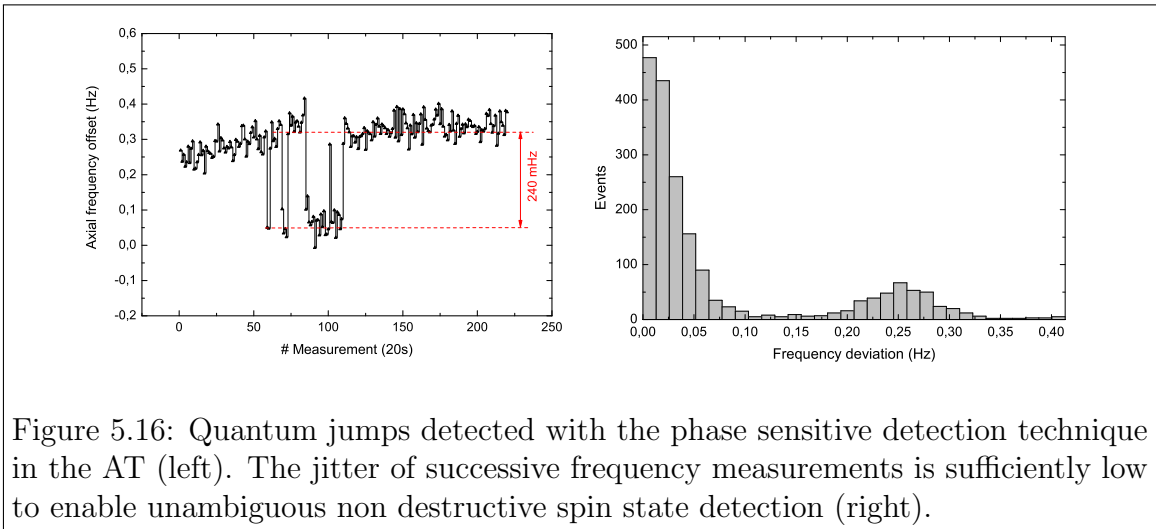
Figure 5.16: Quantum jumps detected with the phase sensitive detection technique in the AT (left). The jitter of successive frequency measurements is sufficiently low to enable unambiguous non destructive spin state detection (right).

5.7.2 Larmor-resonance in the magnetic bottle

The detection of the spin state made possible by the advanced design of the AT instantly enables a first rough determination of the g-factor in the AT. By scanning the microwave excitation frequency across the Larmor resonance, and detecting the rate of induced spinflips as a function of the microwave frequency and the measured cyclotron frequency, a spinflip resonance can be mapped out within about 12 hours. Due to the large magnetic field inhomogeneity in the AT, the Larmor frequency of

the trapped ion becomes strongly dependent on the mode radii of the ion. Considering the typical values of the mode amplitudes (see table 3.1) it is obvious that the axial amplitude dominates the shift of the magnetic field. As the axial energy changes on the timescale of the cooling time constant $\tau_z \ll 1$s, the Larmor frequency takes momentary values according to the Boltzmann distribution of the axial energy. Since the transition between the Zeemann sublevels is driven incoherently[14] on the timescale of several seconds, the spinflip resonance represents the statistical average of the axial energy during the microwave excitation, causing the spinflip resonance to reflect the broad and asymmetric thermal Boltzmann distribution. However, with the current apparatus, employing negative electronic feedback to cool the axial motion, it is already possible to reach a precision of roughly $5 \cdot 10^{-8}$ in the adverse conditions of the AT.
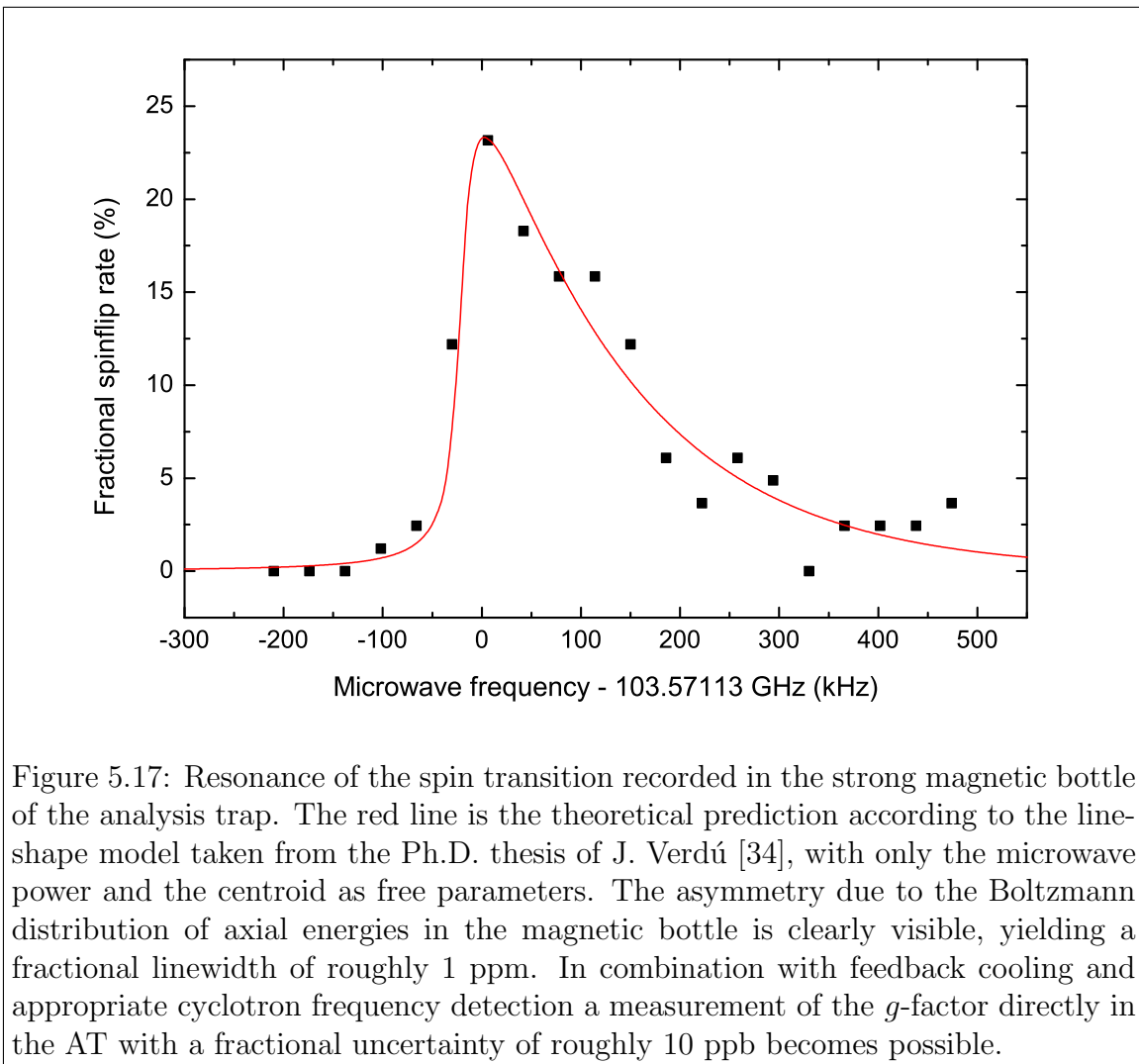
Figure 5.17: Resonance of the spin transition recorded in the strong magnetic bottle of the analysis trap. The red line is the theoretical prediction according to the lineshape model taken from the Ph.D. thesis of J. Verdú [34], with only the microwave power and the centroid as free parameters. The asymmetry due to the Boltzmann distribution of axial energies in the magnetic bottle is clearly visible, yielding a fractional linewidth of roughly 1 ppm. In combination with feedback cooling and appropriate cyclotron frequency detection a measurement of the g-factor directly in the AT with a fractional uncertainty of roughly 10 ppb becomes possible.

---

[14]The magnetic field and with it the momentary Larmor frequency is modulated by the axial motion on the ppm scale. For a coherent excitation at 105 GHz over the duration of 30 s, the magnetic field stability should however be roughly 1 ppt.

5.7.3   Detection of spinflips in the precision trap

In order to reach the precision aimed for, it is necessary to probe the Zeeman transition in the homogeneous magnetic field of the PT. In order to detect the spin state, the ion has to be transported back to the AT. If spontaneous spinflips during the transport can be excluded, it becomes possible to detect spinflips occuring in the PT by comparing the spin states detected in the AT before and after the microwave excitation in the PT. This spatial separation of the spin detection and frequency measurement enables a leap in the precision attainable in the g-factor measurement [45].
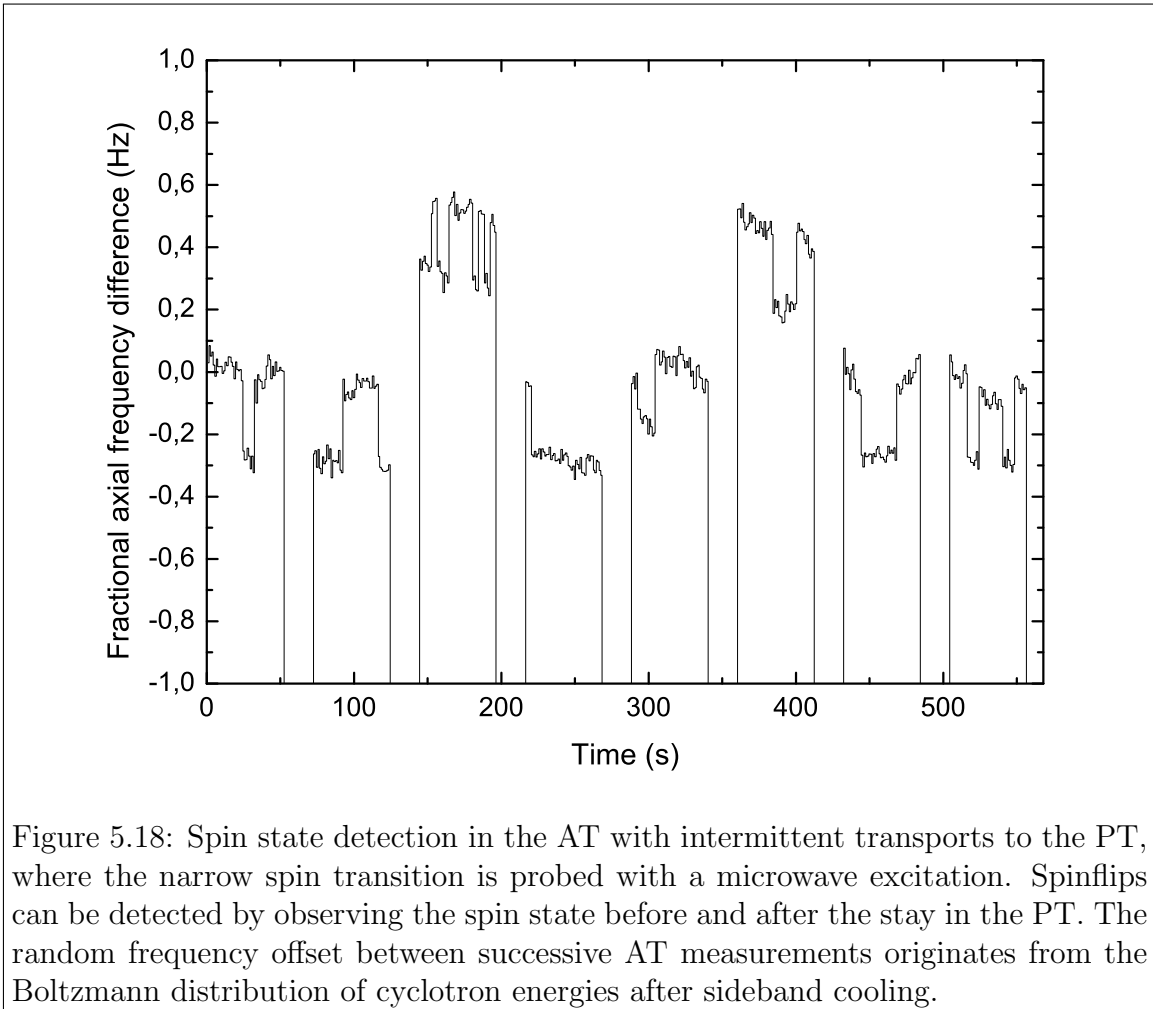
Figure 5.18: Spin state detection in the AT with intermittent transports to the PT, where the narrow spin transition is probed with a microwave excitation. Spinflips can be detected by observing the spin state before and after the stay in the PT. The random frequency offset between successive AT measurements originates from the Boltzmann distribution of cyclotron energies after sideband cooling.

6. The g-factor of $^{28}\mathrm{Si}^{13+}$

"However beautiful the strategy, you should occasionally look at the results."

Winston Churchill

With the techniques introduced in the previous chapter, the foundation for the measurement of the g-factor is established. In the course of this thesis two independent measurements of the g-factor of $^{28}\mathrm{Si}^{13+}$ have been performed, one with the well-known double-dip technique, and a second measurement with the novel PnA method, providing an order of magnitude improvement in the final accuracy. The agreement of both results creates confidence in the understanding of the apparatus and the physics governing the properties of the trapped ion.

6.1 Results with the double-dip technique

The first measurement was done with the double-dip mode coupling technique [34]. Although this technique implies a significant limitation for the attainable precision compared to the PnA method, the result is still more accurate than any other bound electron g-factor measured to date and surpasses the theoretical prediction. The comparison to the g-factor predicted by BS-QED calculations provided the most stringent test of the BS-QED in strong fields to date, as becomes apparent below, and was published in Physical Review Letters [12]. Furthermore, the measurement provides a valuable possibility to verify the error budget of both techniques.

6.1.1 Measurement procedure

After a single ion has been created and prepared in the PT as described in chapters 5.1 and 5.3, the computer automated g-factor measurement starts with the ion in the AT.

1. Automatic resistive sideband cooling of the axial and magnetron motion to thermal equilibrium.

2. Sideband coupling of the cyclotron and axial mode

3. Measurement of the momentary cyclotron energy, repeat step 2 until the energy is below a threshold value

4. 8 successive phase sensitive measurements of the axial frequency

5. Strong microwave excitation at the Larmor frequency for 30 seconds to induce spinflips

6. Loop to step 4 until at least 1 spinflip is detected

7. Adiabatic transport to the PT

8. Sideband cooling of all eigenmodes

9. Wait for 30 seconds to let the trapping voltage settle

10. Open cryogenic switches[1]

11. Detection of a single-dip spectrum for 90 seconds

12. Detection of a double-dip spectrum with a quadrupolar coupling at ν_{coup} for 90 seconds and simultaneous microwave excitation at a *random* frequency ν_{mw} around the predicted Larmor frequency

13. Detection of a second single dip spectrum

14. Close cryogenic switches

15. Adiabatic transport to the AT

16. Loop to first step

During this fully automated process the computer control records all necessary information. The process described above takes approximately 15 minutes, depending on the time necessary to induce a spinflip in the AT, and has to be repeated numerous times in order to obtain a g-factor resonance. The measurement process typically runs continuously for several days, and measurements during and after disturbances are discarded in the data evaluation process. After typically one week, a g-factor resonance has collected sufficient statistics and a new resonance is started with one or more parameters changed. A single resonance contains typically 300 individual measurement steps, with different frequency ratios ν_{mw}/ν_c each. The final g-factor

---

[1]The switches are opened for each excitation, but are left open during the precision measurement to prevent a possible systematic influence.

is determined from all resonances after careful checks for systematic effects. Alto-
gether, 6 resonances were recorded, equivalent to approximately 1.5 months of data
taking. Further collection of statistics would be unprofitable, since a further splitting
of the resonance appears too venturous.

6.1.2 *g*-factor resonances

The linewidth in the improved setup is entirely dominated by the measurement noise
of the dip detection technique as discussed in chapter 5.4.1. Since the determined free
cyclotron frequency shows a normally distributed measurement error, the *g*-factor
lineshape is likewise expected to be predominately Gaussian. For the determination
of the *g*-factor the measured resonance is thus fitted to a Gaussian line and the error
introduced by this simplification will be discussed in chapter 6.1.3.6.

6.1.2.1 Maximum likelihood fit

The resonance consists of two sets of frequency ratios of microwave and cyclotron
frequency, one for successful and one for failed spinflip attempts. These sets can
be binned into appropriate intervals in order to yield a visual representation of
the resonance line. However, the binning procedure introduces several inaccuracies.
The bin width can be chosen arbitrarily within certain limits and the determined
value can depend on the specific choice of this parameter, especially for resonances
with low statistics [37]. Furthermore, the error assigned to the binned data points
is determined by the binomial probability distribution and is strongly asymmetric
especially for bins with low spinflip probability. However, the nonlinear regression
based on the least squares method implicitly assumes normally distributed errors.
This can introduce significant bias into the fit result especially if the statistical error
is asymmetric about the resonance line and generally produces excessively optimistic
parameter error estimates.
Contrary to previous experiments a maximum likelihood fit is used to determine the
g-factor in this thesis. The maximum likelihood method considers the statistical
probability of the *complete* set of measured ratios as a function of a set of lineshape
parameters. The likelihood function $\mathcal{L}$ [76] of the experiment is defined as the
uncorrelated probability of the realization of the set of measurements:

$$\mathcal{L} = \prod_i p_i\left(\{P\}\right). \tag{6.1}$$

The result of the global maximization of the likelihood function provides an unbiased
estimator of the parameter set $\{P\}$. The individual probabilities p_i can be deter-
mined trivially from the lineshape, without the need of any binning. Furthermore,
the binomial error of the process is consistently integrated in this method, allowing
to extract accurate parameter error estimates.
In practice, the logarithm of the likelihood function is maximized, which is equivalent
to the aforementioned procedure, but is numerically more effective as the logarithm
can be decomposed into a sum, which eliminates the product of very small numbers

that potentially causes numerical problems in the calculation of the goal function in the minimization process:

$$\log \mathcal{L} = \sum_i \log p_i \left(\{P\}\right). \tag{6.2}$$

The fitted resonance (see figure 6.1) has a linewidth which is indeed in good agreement with the linewidth of the cyclotron frequency noise. This clearly demonstrates that the origin of the statistical noise is well understood. The remeasurement of the g-factor with the PnA method furthermore proves the anticipated reduction of the linewidth due to the improved cyclotron frequency measurement precision.

6.1.2.2   Determination of the g-factor

From the result of this fitting procedure, it is possible to determine the ratio $\Gamma_0 \equiv \frac{v_L}{\nu_c}$, which in turn allows to calculate the g-factor:

$$g = 2\Gamma_0 \frac{m_e}{m_{\mathrm{ion}}} \frac{13}{}. \tag{6.3}$$

The final result is obtained from a weighted average of all 6 recorded resonances. Figure 6.1 shows an exemplary resonance. In the visualization, data points from a binning procedure are displayed, however these points do not affect the fitting procedure.

6.1.3   Error budget and technical parameters

The frequencies measured in a Penning trap are subject to some obvious and a number of subtle systematic shifts. Before the final g-factor value can be determined, these effects have to be thoroughly analyzed and corrected. It is possible to distinguish between mode energy dependent shifts and static shifts. The improvements of the new apparatus and the measurement techniques acts to cut down the effect of most of the energy dependent shifts considerably, but the improved precision requires to consider previously neglected effects.

6.1.3.1   Magnetic field homogeneity

Although the homogeneity of the magnetic field in the PT has been considerably improved, magnetic field inhomogeneities can still generate significant shifts of the eigenfrequencies. The influence of the shift of the eigenfrequencies on the value of the determined free cyclotron frequency depends on the measurement method or more specifically on the mode energies during the measurement of the individual frequencies.

If all frequencies are determined with the axial double-dip technique, the resulting frequency shift is extremely small. The energy in the radial modes is directly connected to the thermal energy expectation value of the axial mode:

$$\begin{aligned}
\langle E_+ \rangle &= \frac{\omega_+}{\omega_z} \langle E_z \rangle \\
\langle E_- \rangle &= -\frac{\omega_-}{\omega_z} \langle E_z \rangle.
\end{aligned}$$

Figure 6.1: One of the 6 recorded resonances with the double-dip detection technique. Compared to previous g-factor experiments the linewidth is significantly smaller and the resonance shows no asymmetry. The relative precision obtainable from this resonance is about $\delta g / g = 0.4$ ppb. Corrections for systematic shifts arising from the interaction with the cavity are not included in the resonance. The dark gray area represents the 1-σ prediction band for the measurements, while the dark gray region displays the confidence band of the fit with respect to the centroid parameter. The data points are merely plotted for visualization and do not enter the fitting procedure.

With equation (3.26) it is thus possible to calculate the resulting shift of the free cyclotron frequency. The dominant contribution in this configuration originates from the shift of the cyclotron frequency due to the finite axial radius:

$$\delta \nu_+ = \langle E_z \rangle \, \frac{B_2}{B_0 \, m \, (2\pi\nu_z)^2} \nu_+ \left(1 - \frac{\nu_z}{\nu_+} \right). \tag{6.4}$$

The leading order contributions of the cyclotron energy on the axial- and cyclotron frequency cancel and the contribution of the magnetron energy and frequency are negligible:

$$\bar{\nu}_c \simeq \sqrt{(\nu_+ + \delta\nu_+)^2 + (\nu_z + \delta\nu_z)^2 + (\nu_- + \delta\nu_-)^2} \tag{6.5}$$

$$\simeq \sqrt{\nu_c^2 + 2\nu_+\delta\nu_+ + 2\nu_z\delta\nu_z + 2\nu_-\delta\nu_-} \tag{6.6}$$

$$\simeq \nu_c \left(1 + \langle E_z \rangle \frac{B_2}{B_0\, m\, (2\pi\nu_z)^2}\right). \tag{6.7}$$

The expected relative shift of the free cyclotron frequency during the double-dip measurement at 4.8 K is thus:

$$\frac{\delta\nu_c}{\nu_c} \simeq 2 \cdot 10^{-11}, \tag{6.8}$$

highlighting once again the exceptional importance of a low axial energy during the measurement process.

However, in a g-factor measurement, where the Larmor frequency is measured simultaneously, the leading order contributions of the magnetic field cancel and the residual contributions are suppressed by a factor of $\frac{\nu_z}{\nu_+}$. On the level of accuracy reached in the double-dip measurement, the contribution of the magnetic field shift is thus negligible.

6.1.3.2 Relativistic shift

As a result of the reduced magnetic inhomogeneity and the improved precision, the frequency shifts arising from special relativity can become substantial in this experiment. However, in the case of the sideband cooled cyclotron mode this shift is very small, as there is almost no contribution from the slow axial motion. The relativistic shift of the free cyclotron frequency is predominantly given by the relativistic mass increase of the ion:

$$\frac{\delta\nu_c}{\nu_c} \simeq -\frac{\nu_+}{\nu_z mc^2}\langle E_z \rangle \simeq -6 \cdot 10^{-13}. \tag{6.9}$$

The relativistic shift of the Larmor frequency is even smaller by a factor of $\frac{\nu_c}{\nu_L}$:

$$\frac{\delta\nu_L}{\nu_L} \simeq \frac{\delta\nu_c}{\nu_c}\frac{\nu_c}{\nu_L} \simeq -1.5 \cdot 10^{-16}. \tag{6.10}$$

6.1.3.3 Anharmonic electrostatic potential

The electrostatic potential can be tuned very precisely, leaving only very small residual anharmonicities. The tuning ratio can be easily determined to better than 10 ppm, resulting in a residual C_4 term of roughly $2.55 \cdot 10^5$ V/m^4. Following equation (3.14) the cyclotron frequency shift from the electrostatic field anharmonicity can be deduced:

$$\frac{\delta\nu_c}{\nu_c} \simeq \frac{3\, C_4\, \nu_z^2}{2\, q\, C_2^2\, \nu_c^2}\langle E_z \rangle \simeq -1.8 \cdot 10^{-13}. \tag{6.11}$$

There is no respective shift of the Larmor frequency, hence the influence of the trapping potential is negligible in the double-dip measurement.

6.1.3.4   Drift of the electrostatic field

Since the axial frequency is not measured simultaneously to the double-dip spectrum, in principle a drift of the trapping potential could produce a shift of the determined cyclotron frequency. By measuring single dip spectra immediately before and after the double dip, linear drifts are canceled by taking the average axial frequency of both measurements. The comparison of the two single-dip measurements reveals a slight residual drift resulting from the drift of the trapping voltage that is changed when the ion arrives in the PT. The waiting time introduced in the measurement process decreases this drift to approximately 7 mHz (see figure 6.2). The error introduced onto the cyclotron frequency should thus be well below 0.1 ppb.
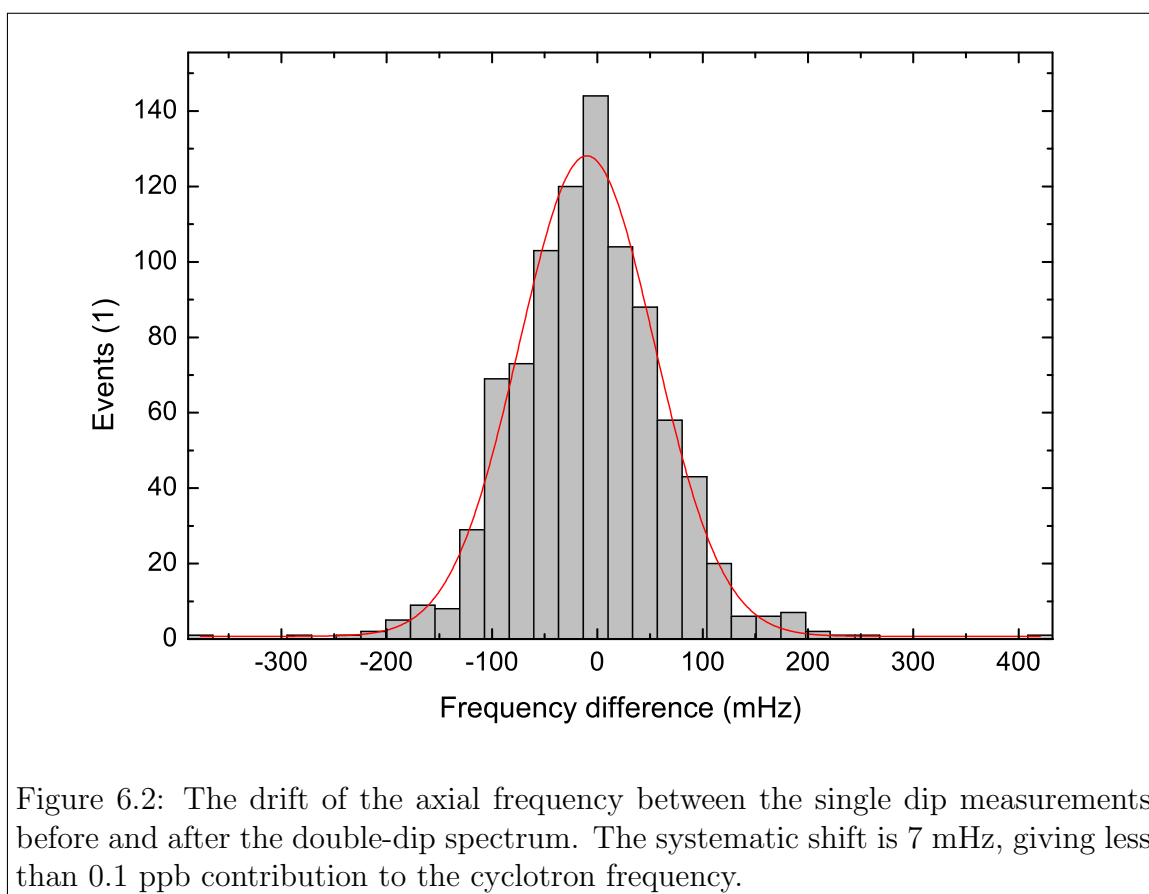
Figure 6.2: The drift of the axial frequency between the single dip measurements before and after the double-dip spectrum. The systematic shift is 7 mHz, giving less than 0.1 ppb contribution to the cyclotron frequency.

6.1.3.5   Tilt of the electrostatic potential

The solution of the equations of motion of the Penning trap implicitly assumes a perfectly aligned magnetic and electric field. In reality, despite great efforts to reach the highest possible manufacturing precision, there will always be a residual tilt of the electric trap axis with respect to the magnetic field lines, causing systematic

shifts of the eigenfrequencies compared to the ideal trap. Fortunately, the invariance theorem allows to cancel the effect of both the tilt of the trap axis and a possible first order deviation from the cylindrical symmetry, which can be parametrized as an effective ellipticity.

The difference between the cyclotron frequency determined with the invariance theorem, which depends on the absolute value of the magnetic field, and with the sum frequency $\bar{\omega}_c = \omega_+ + \omega_-$, which measures the axial component of the magnetic field, can be used to estimate the value of the mechanical tilt θ:

$$\theta^2 - \frac{2}{9}\,\epsilon^2 = \frac{4\,\delta\omega_c}{9\,\omega_-}. \tag{6.12}$$

By neglecting the influence of the ellipticity it is possible to extract an estimation of the tilt:

$$\theta \simeq (0.11 \pm 0.05)^\circ, \tag{6.13}$$

which confirms the precision of the mechanical setup.

6.1.3.6 Lineshape of the g-factor resonance

Most of the previously discussed effects act to shift both the cyclotron and Larmor frequency. However, while the cyclotron frequency is determined at each measurement, the Larmor frequency can only be extracted from the complete set of measurements. The lineshape of the spinflip resonance thus depends on the distribution of mode energies during the measurement. In the case of the double-dip technique, primarily the relatively large axial amplitude acts to sample the increasing magnetic field according to the Boltzmann distribution of the energy:

$$\frac{\delta B}{B_0} \simeq \frac{B_2}{B_0}\,z_{\text{rms}}^2 \leq 3.8 \cdot 10^{-11}, \tag{6.14}$$

for axial temperatures $T_z \leq 4.8\,K^2$, equivalent to amplitudes $z_{\text{rms}} \leq 11\,\mu\text{m}$. This manifests as an asymmetric tail on the right-hand side of the spinflip resonance.

The accurate derivation of the lineshape function was carried out in the Ph.D. thesis of J. Verdú [34] in order to describe the spinflip resonance of the oxygen g-factor experiment, with the assumption that the lineshape is predominantly given by the contribution of the magnetic field inhomogeneity. However, technical advances in both the magnetic field homogeneity and ion temperature have decreased the inhomogeneity shifts by almost 3 orders of magnitude, leaving the cyclotron frequency uncertainty as the dominant contribution to the linewidth. The jitter of the cyclotron frequency readout is clearly normally distributed, with a linewidth that is typically orders of magnitude larger than the inhomogeneity shifts, especially for the double-dip measurement (see figure 5.10). The resulting lineshape is predominantly Gaussian, with a very slight asymmetry. In fact the thorough analysis of the lineshape following the discussion in the Ph.D. thesis of J. Verdú (see figure 6.3)

---

^{2}Depending on the applied feedback.

confirms that a Gaussian fit to the measured resonance introduces an error signifi-
cantly below $\delta g/g \leq 5 \cdot 10^{-11}$ without negative feedback and $\delta g/g \leq 1 \cdot 10^{-11}$ with
appropriate negative feedback as used during the PnA measurement.
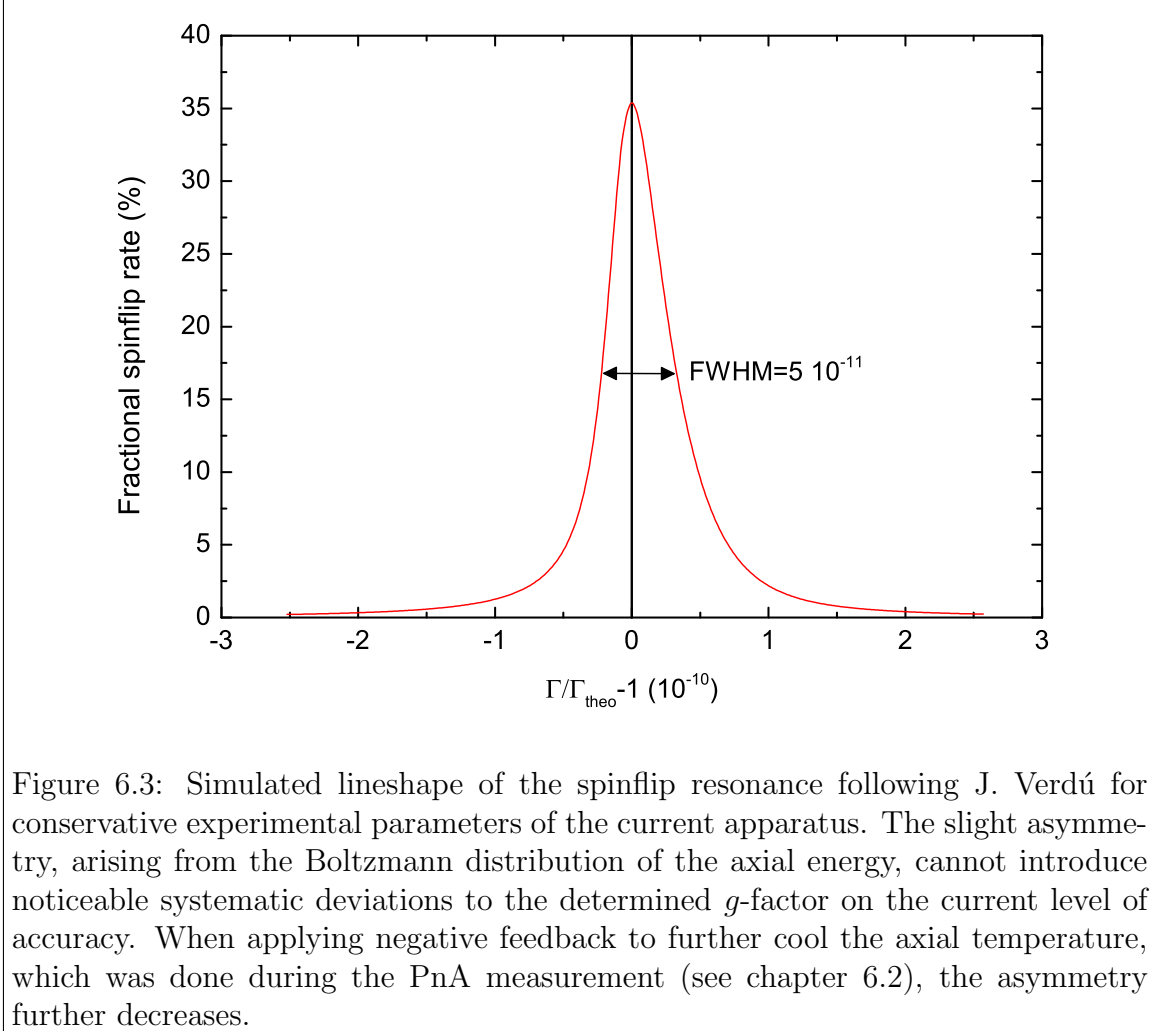
Figure 6.3: Simulated lineshape of the spinflip resonance following J. Verdú for
conservative experimental parameters of the current apparatus. The slight asymme-
try, arising from the Boltzmann distribution of the axial energy, cannot introduce
noticeable systematic deviations to the determined g-factor on the current level of
accuracy. When applying negative feedback to further cool the axial temperature,
which was done during the PnA measurement (see chapter 6.2), the asymmetry
further decreases.

6.1.3.7   Image current shift

Both the axial and cyclotron mode are weakly coupled to tank circuits that exert
some back action on the particle. As discussed in chapter 3.3, the ion experiences a
force due to the voltage induced onto the resonator by its own motion:

$$F_d(\dot{x}(t)) = \frac{q^2}{D^2} Z(\omega) \dot{x}(t), \tag{6.15}$$

where $Z(\omega)$ denotes the in general complex impedance of the tank circuit. The
respective equation of motion is analogue to a harmonic oscillator with complex
damping:

$$\ddot{x}(t) = -\omega_+^2 x(t) - 2\delta \dot{x}(t), \tag{6.16}$$

where $\delta \equiv \frac{q^2}{2\,m\,D^2} Z(\omega_+)$ denotes the complex damping constant. The solutions to this effective eom are given by:

$$x(t) = x_0^{1,2}\, e^{\mp \delta\, t \pm \sqrt{\omega_+^2 - \delta^2}\,t}. \tag{6.17}$$

The real part of the impedance causes an exponential damping of the motion with the cooling time constant τ, as already discussed, but has only a marginal influence on the eigenfrequency. However, the imaginary part of the impedance features a more subtle effect [77] that can potentially have significant influence on the measured frequency: The effective back action on the ion is in phase with the particle position, giving rise to an effective electrostatic potential, similar to the image charge field discussed in chapter 6.1.3.8, but originating from the phase shifted ion current rather than the static ion charge. Neglecting the insignificant contribution of the damping, the effective eigenfrequency of the ion thus becomes:

$$\tilde{\omega}_+ \simeq \omega_+ - \operatorname{Im}\delta(\omega_+). \tag{6.18}$$

Assuming a purely capacitive impedance of 10 pF, the frequency shift becomes rather small:

$$\frac{\delta\omega_+}{\omega_+} \simeq 4 \cdot 10^{-13}. \tag{6.19}$$

However, if the imaginary impedance is enhanced close to the resonance of the tank circuit, this frequency error can become significant:

$$
\begin{aligned}
\frac{\delta\omega_+}{\omega_+} \quad &= -\frac{\operatorname{Im}(\delta(\omega_+))}{\omega_+} \\
&= -\frac{1}{\tau_+\, R\, \omega_+}\, \mathcal{I}\left(Z(\omega_+)\right) \\
&\simeq -\frac{Q}{\tau_+}\, \frac{\Delta\omega}{\omega_+^2 + 4\, Q^2\, \Delta\omega^2},
\end{aligned}
\tag{6.20}
$$

where ω_R denotes the resonance frequency of the tank circuit, τ_+ is the cooling time constant of the cyclotron mode in resonance and $\Delta\omega \equiv \omega_R - \omega_+$ denotes the detuning of the ion with respect to the tank circuit. Figure 6.4 shows the dependence of the frequency shift from the detuning of the ion. The shift can be controlled by either bringing the ion exactly in resonance with the tank circuit, where the impedance is completely real, or by shifting the resonator sufficiently far away from the ion. Since the detection and control of the absolute resonance center to better than 1% is a rather adventurous task, in practice it is simpler to shift the tank circuit with controllable parallel capacitances. Far away from resonance, the shift is sufficiently insensitive to detuning in order to allow accurate correction for the residual shift.

The relatively low parallel resistance of the cyclotron tank circuit results in a negligible frequency shift on the precision level of the double-dip measurement. For the higher precision measurement with the PnA method, this shift however has to be considered.
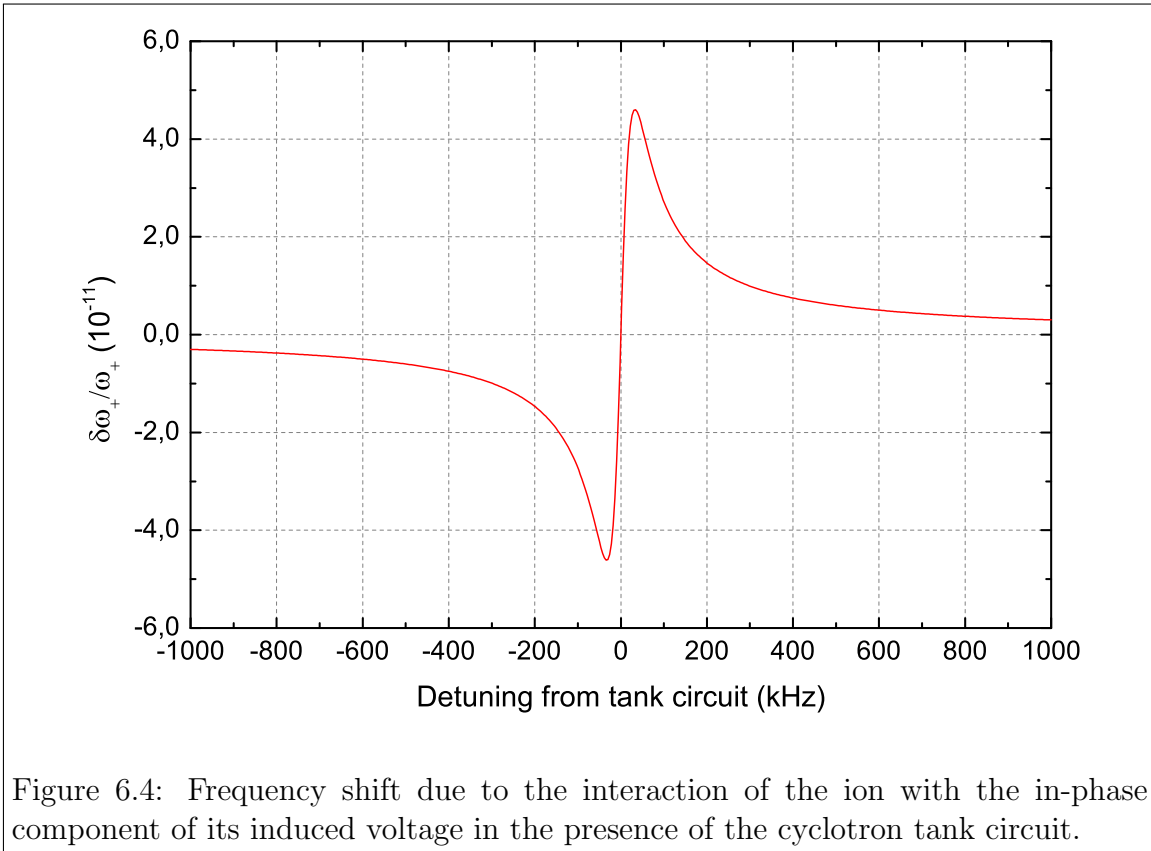
Figure 6.4: Frequency shift due to the interaction of the ion with the in-phase component of its induced voltage in the presence of the cyclotron tank circuit.

6.1.3.8   Image charge shift

Even at rest, the electrode structure has influence on the eigenfrequencies of the ion, independent of the tank circuit. The charge of the ion induces image charges in the electrodes, which again generate an additional electrostatic field [37, 78]. Similar to the previously mentioned image current shift, the back action of the induced charges on the ion can be divided into in-phase and out-of-phase components. The out-of-phase component is caused by the portion of the image charge field that arrives time-retarded due to the finite speed of light. However, considering the radius of the trap and the wavelength of the cyclotron frequency

$$\frac{r_0}{\lambda_+} = \frac{c\, r_0}{\nu_+} \simeq 0.04, \tag{6.21}$$

this contribution can be safely neglected compared to the in-phase component[3].
The in-phase component causes an additional effective electrostatic potential in the rest frame of the ion. As this potential is caused by the presence of the charge in the trap region, it does not fulfill the Laplace equation and thus causes a frequency shift that is in first order not canceled by the invariance theorem[4].
The image charge potential can be approximated by neglecting the slits between

---

[3]In the Ph.D. thesis of H. Häffner this effect is estimated to be smaller than 0.01 ppt.
[4]The invariance theorem accounts for electrostatic potentials and magnetic inhomogeneities in quadratic order as explained in chapter 3.2.5

the electrodes and assuming the electrode set to form an infinite cylinder. In this approximation the potential has been evaluated by H. Häffner, yielding

$$\Phi_{ic} = \frac{q}{8\,\pi\,\epsilon_0\,r_0^3}\,\rho^2. \tag{6.22}$$

Since the image charge potential is mediated by the conducting electrodes, independent of the trapping field, the center of the pseudo-potential is referenced to the geometrical center of the trap, rather than the electrostatic center. Since the potential is quadratic in good approximation, it can be added to the quadratic trapping potential even if both are spatially displaced due to patch potentials.

Due to the inherent axial symmetry, the force of the image charge has only a radial component. In the radial plane, the quadratic potential adds to the trapping potential and yields in first order a harmonic shift of the magnetron and cyclotron frequency:

$$\Delta\omega_{\pm} \simeq \mp\frac{q^2}{4\,\pi\,\epsilon_0\,m\,r_0^3\,\omega_c} \simeq \mp 18.4\,\text{mHz}. \tag{6.23}$$

Although the magnetron and cyclotron frequencies shift both by the same amount but with opposite sign, if the invariance theorem is used to calculate the free cyclotron frequency, the resulting relative shift is very significant on the current level of accuracy:

$$\frac{\Delta\omega_c}{\omega_c} \simeq -6.86 \cdot 10^{-10}. \tag{6.24}$$

This is the dominant systematic frequency error of the experiment. Just like the image current shift, the image charge shift increases strongly with the charge of the ion:

$$\Delta\omega_+ \sim \frac{q^2}{m}, \tag{6.25}$$

making the image charge shift increasingly problematic for the measurement of heavier ions. However, the strong dependence on the trap radius r_0,

$$\Delta\omega_+ \sim \frac{1}{r_0^3}, \tag{6.26}$$

allows to reduce the effect by making the trap accordingly larger. The development of the PnA method allows to increase the trap size without sacrificing signal strength. For the current trap, the manufacturing accuracy of the electrodes causes a relative uncertainty of the correction of roughly 1%. Since the influence of the slits between the individual electrodes is not yet evaluated, a conservative uncertainty of 5% is attributed to the correction. This allows to correct the free cyclotron frequency to $3.3 \cdot 10^{-11}$.

6.1.3.9   Time reference

The experiment is based on the determination of the ratio of two frequencies, such that fluctuations of the absolute time reference are canceled to a large extend. However, the averaging properties of the spin transition are in general non-linear, so

that excessive fluctuations of the absolute microwave frequency, comparable with the linewidth of the g-factor resonance, cause an undesired broadening of the resonance. For this reason, all frequency generators and the FFT analyzer are referenced to a commercial 10 MHz rubidium clock. The residual fluctuations and inaccuracies are negligible on the current level of accuracy.

6.1.3.10 Dip line shape

The double-dip detection relies on the extraction of the eigenfrequencies from a fit with a known lineshape. However, the dip linewidth is large compared to the required precision. The determination of the g-factor with the double-dip technique to a relative precision of 0.1 ppb corresponds to splitting the dip line to roughly 1‰, a rather precarious intend, provided that any nonlinearity of the detection system transfer function[5] can potentially cause systematic shifts of the mean determined frequency. Although no significant deviations from the theoretical lineshape can be detected even in excessively long averaged dip spectra, a rather conservative line shape uncertainty of 3 mHz is assumed.

6.1.4 Final result

In total, six g-factor resonances were recorded with the double-dip technique, each containing roughly 300 cycles. Although the theoretical estimations of the energy dependent shifts with the improved setup are clearly negligible compared to the static shifts and the uncertainty of the electron mass [79, 80], the axial temperature and the microwave power were varied between the measurements, in order to check the validity of the calculations. From the fits to the individual resonances, the preliminary uncorrected frequency ratio $\Gamma_0' = 3912.866066(1)$ is extracted. Before the g-factor can be calculated, the previously presented corrections to systematic shifts have to be applied, which are summarized in tables 6.1, 6.2 and 6.3. The

Effect	relative size (ppt)	uncertainty of final result (ppt)
Magnetic field inhomogeneity[6]	20	< 1
Special relativity	0.6	0.6
Electrostatic potential	0.2	0.2
g-factor lineshape	< 10	< 10
Sum (quadratic)	< 23	< 10

Table 6.1: Energy dependent systematic shifts

error budget of the measured frequency ratio Γ_0 is thus dominated by the static shifts,

---

[5]Note that the lineshape used in the data evaluation takes linear transfer functions into account

[6]Shift of the cyclotron frequency. With the presented method magnetic inhomogeneity does not produce systematic shifts of the g-factor in leading order.

Effect	relative size (ppt)	uncertainty of final result (ppt)
Image current	20	10
Image charge	686	34
Dip lineshape	100	100
Timebase	< 10	< 10
Sum (quadratic)	694	108

Table 6.2: Static systematic shifts

Constant	relative uncertainty (ppt)
Electron mass in u	400
Ion mass in u	35
Sum	402

Table 6.3: External constants uncertainty

originating predominantly from the interaction of the ion with its own image charge and the dip lineshape uncertainty. Subsequently, the g-factor can be calculated:

$$g = 2\Gamma_0 \frac{13\, m_e}{m_{\mathrm{ion}}}. \tag{6.27}$$

The required electron mass is taken from the current (2010) CODATA compilation:

$$m_e = 5.485\,799\,0946(22) \cdot 10^{-4}\,\mathrm{u}, \tag{6.28}$$

and the ion mass can be calculated from the atomic mass measured by Redshaw *et al.*

$$M\!\left(^{28}\mathrm{Si}\right) = 27.976\,926\,535\,0(6)\mathrm{u}, \tag{6.29}$$

corrected by the masses of 13 electrons and their respective binding energies, taken from [81]:

$$M\!\left(^{28}\mathrm{Si}^{13+}\right) = 27.969\,800\,594\,9(7)\mathrm{u}. \tag{6.30}$$

The final value of the g-factor is deduced from the weighted average of the individually corrected values of the 6 resonances, summarized in figure 6.5:

$$\boxed{g_{\mathrm{exp}} = 1.995\,348\,958\,66(50)(30)(80).} \tag{6.31}$$

The first uncertainty represents the statistical precision of the determination of Γ_0 from the recorded resonances, the second one denotes the systematic uncertainty and the last one represents the uncertainty of the electron mass. This value can now be compared with the prediction from state-of-the-art BS-QED calculations [12]:

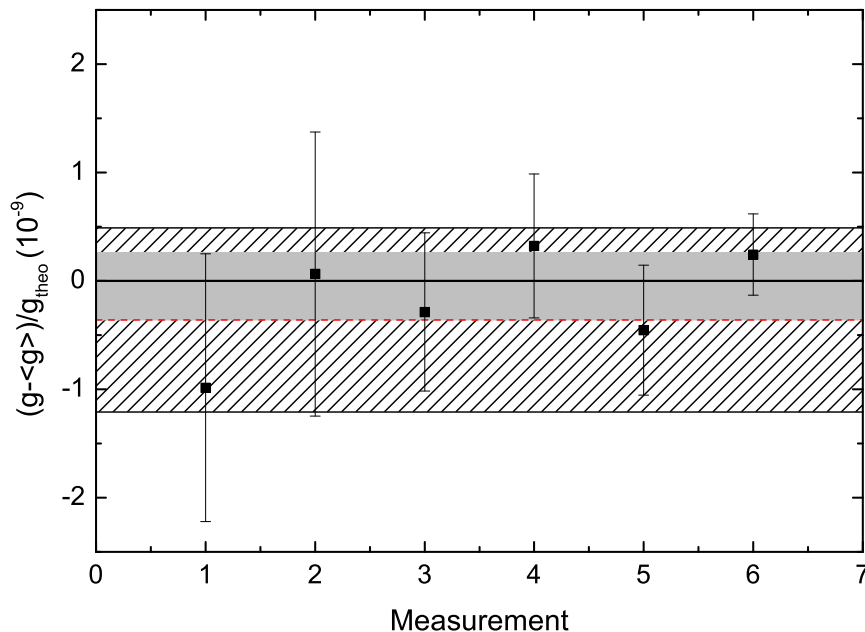$$\boxed{g_{\mathrm{theo}} = 1.995\,348\,9580(17).} \tag{6.32}$$

Figure 6.5: The corrected g-factor values determined from the six individual resonances. The gray band represents the statistical uncertainty of the experimental value, while the hatched area is the uncertainty of the theoretical prediction. Obviously, both are in perfect agreement.

Both values agree perfectly, however the experimental result is significantly more accurate, despite the limitation from the electron mass value. The presented measurement is the result of one month of data taking, after roughly seven years of preparation. The result is the most accurate determination of an atomic g-factor ever performed.

With the experimental result it becomes possible to verify the validity of the BS-QED theory in extreme situations by comparing the determined value with the theoretical prediction. Indeed, even at this level of accuracy and sophistication, QED once more is in perfect agreement with the experimental observation.

The achieved accuracy, even including the temporary limitation due to the uncertainty of the CODATA value of the electron mass, allows to validate all contributions to the theoretical g-factor considered in chapter 2, for the first time including vacuum polarization and nuclear size effects as well as higher order contributions of the two loop theory.

6.1.5 The nuclear charge radius of $^{28}\text{Si}^{13+}$

For the g-factor of $^{28}\text{Si}^{13+}$, the contribution of the finite nuclear size is for the first time significant. This contribution can be calculated by using independent values for the charge radius of the nucleus. On the other hand, the measurement can be

used to determine the charge radius by comparing the predicted g-factor as function of the charge radius with the experimentally determined value. If all other input parameters are known to sufficient precision, the charge radius is the value that satisfies the relation

$$g_{\text{exp}} = g_{\text{theo}}\left(\sqrt{\langle r^2_{^{28}\text{Si}}\rangle}\right). \tag{6.33}$$

With the afore-mentioned g-factor values the charge radius is

$$\sqrt{\langle r^2_{^{28}\text{Si}}\rangle} = 3.18(15)\text{fm}, \tag{6.34}$$

in perfect agreement with the literature value of 3.1223(24) fm [82], but significantly less precise. The precision of the charge radius extraction is predominantly limited by the theoretical knowledge of the higher order QED contributions and the uncertainty of the electron mass. Nevertheless, this method to determine nuclear charge radii can become interesting in the future. If the precision of the QED calculation can be increased, the achieved experimental accuracy with the PnA method (see next chapter) is principally sufficient to provide competitive values already for ^{28}Si. As the nuclear size contribution increases strongly in heavier systems, it is conceivable to determine extremely accurate charge radii for these systems.

6.1.6   Comparison with other QED tests

The large number of relevant contributions, in combination with the accuracy of the comparison and the magnitude of the electric field strength in the $^{28}\text{Si}^{13+}$ ion, render this measurement the most stringent test of the BS-QED to date.

The previous bound-state g-factor measurements on hydrogenlike carbon and oxygen are far less sensitive, owing to the lower experimental accuracy of 4 ppb and the drastically lower electric field in the lighter systems. However, the determination of the electron mass from the result of the carbon experiment is the basis of the accuracy of this result.

The measurement of the free electron anomaly with a relative accuracy of 0.4 ppb by Gabrielse can be used as a test of low-field QED, if an independent value of the finestructure constant is available. Currently, the most accurate independent value comes from atomic recoil measurements, yielding a precision of 0.8 ppb for the comparison. These two measurements together constitute the most stringent QED test in the low field regime.

In order to form conclusive tests of bound-state QED, it is necessary to identify systems where observable or combinations of observables are available that allow both accurate calculation and experimental determination and which are sensitive to QED effects. Some of the most prominent examples include the determination of the hyperfine splitting (HFS) in different electronic states of light atoms and ions [83]. Although high-precision measurements are available for a number of light species, the strong dependence of the HFS on the structure of the nucleus renders the extraction of a precision test of BS-QED in these systems impossible. However, by comparing the HFS in two different electronic states, it is possible to construct observables that cancel the nuclear structure effect while still featuring significant

sensitivity to QED. The most successful test comes from the comparison of the HFS of the 1s and 2s states of ^{3}He$^+$ ions [84, 85]. Experiment and theory show reasonable agreement, allowing to test QED on the level of roughly 1 ppm. However, the field strength in these light systems is still very small, which brings many effects of the BS-QED out of reach of this test.

In the high field regime, most tests suffer from the extremely strong influence of the nuclear structure (NS) on all observables. For the HFS of hydrogenlike Pb, the NS contribution prevents the conclusive extraction of BS-QED contributions [86]. Nevertheless, the determination of the Lamb shift in hydrogenlike uranium at the GSI ESR, despite the low accuracy of the experimental value of only 1%, gives access to QED contributions, since the Lamb shift in itself is a QED effect. In this regime of extremely strong fields, this experiment is still the only source of conclusive information [8].

In order to validate BS-QED in all regimes, all of the mentioned experiments have to contribute. However, the bound-state g-factor determination clearly covers the largest regime of all tests.

6.2   Results with the PnA method

The analysis of the data from the double-dip technique has shown that the experiment has surpassed the precision of the theoretical prediction. On the other hand, the error budget shows that the dominant uncertainty contributions originate from the double-dip technique. Specifically, the cyclotron frequency determination jitter prevents to fully exploit the extremely low systematic errors in the improved setup. The PnA measurement thus opens exciting prospects for ultra precision determination of g-factors. Obviously the determination of a bound-state g-factor on a level below 0.1 ppb further challenges the progress of theoretical calculations, which will in the future allow even more stringent BS-QED verifications. Furthermore, the g-factors of light species are already presently known to sufficient accuracy, allowing the extraction of fundamental constants.

The determination of the g-factor of ^{28}Si^{13+} with the PnA method thus paves the way to intriguing measurements in the near future.

6.2.1   Measurement procedure

The measurement procedure is basically similar to the previously described technique. Primarily the PnA measurement is added to the existing procedure. The cyclotron frequency measurement consists of a set of phase measurements with different evolution times in order to allow the unwrapping of the cyclotron phase. The shortest evolution period (10 ms) is repeatedly measured to yield a precise starting phase. A previously measured double-dip spectrum serves to provide an initial guess of the cyclotron frequency for the unwrapping procedure. The typical jitter of the double-dip measurement of roughly 100 mHz allows to reliably predict the phase up to two seconds evolution time[7]. Since the double dip is recorded additionally to the

---

[7]Two seconds evolution correspond of 500 mHz unambiguous phase-jump free range.

PnA cycle, the complete measurement cycle is effectively longer than during the first g-factor measurement, although the PnA cycle alone is intrinsically faster than the double-dip cycle.

The longest evolution period, 5 seconds in this case, is repeated twice. The first determination serves for accurately predicting the Larmor frequency at the time of the actual measurement. Finally, coincidently with the second 5 second measurement, a microwave excitation at a random frequency close to the estimated Larmor frequency is introduced. For the calculation of the cyclotron frequency, only the magnetic field during the longest measurement is critical, the sensitivity of the short measurement is suppressed by the ratio of the evolution times $\frac{t_1}{t_2}$. This allows the simultaneous measurement of the Larmor- and cyclotron frequency. Although the short measurements are essentially invariant, they are recorded in each cycle in order to exclude accidental shifts of the starting phase[8].

The axial frequency is determined in the same way as before, once before and once after the PnA measurement. However, since the PnA technique implements a direct determination of the cyclotron frequency, rather than an offset to the axial frequency as in the double-dip technique, the contribution of the axial frequency to the free cyclotron frequency value is now suppressed by a further factor of $\frac{\omega_z}{\omega_+} \simeq \frac{1}{37}$, which significantly relaxes the requirements for the precision.

The complete measurement procedure is very similar to the double-dip measurement:

1. Automatic resistive sideband cooling of the axial and magnetron motion to thermal equilibrium.

2. Sideband coupling of the cyclotron and axial mode

3. Measurement of the momentary cyclotron energy, repeat step 2 until the energy is below a threshold value

4. Eight successive phase sensitive measurements of the axial frequency

5. Strong microwave excitation at the Larmor frequency for 30 seconds to induce spinflips

6. Loop to step 4 until at least 1 spinflip is detected

7. Adiabatic transport to the PT

8. Sideband cooling of all eigenmodes

9. Wait for 30 seconds to let the trapping voltage settle

10. Open cryogenic switches[9]

---

[8]Although such a shift was never observed during the measurement, any change in the parameter of the detection system could potentially contribute.

[9]The switches are opened for each excitation, but are left open during the precision measurement to prevent a possible systematic influence.

11. Detection of a double-dip spectrum with a quadrupolar coupling at ν_{coup} to provide a cyclotron frequency *estimate* for the phase unwrapping

12. Detection of a single dip spectrum for 90 seconds

13. Activate negative feedback

14. Measurement of 6 PnA cycles with 10 ms evolution time to fix the initial phase, with sideband cooling after each measurement

15. Measurement of 4 PnA cycles with intermediate evolution times, with sideband cooling after each measurement (not used for evaluation)

16. Measurement of 1 PnA cycle with 5 s evolution time to provide an accurate estimate of the Larmor frequency

17. Measurement of 1 PnA cycle with 5 s evolution time with simultaneous microwave excitation at a *random* frequency close to the Larmor frequency estimate

18. Deactivate negative feedback

19. Detection of a second single dip spectrum

20. Close cryogenic switches

21. Adiabatic transport to the AT

22. Loop to first step

6.2.2   Achievable linewidth

Before each PnA cycle, the cyclotron mode has to be cooled. Since the cyclotron tank circuit was not available during the measurement due to accidental detuning, the cyclotron mode was only sideband cooled via the axial tank circuit. In order to achieve the lowest possible temperature, negative feedback was applied to the resonator during the cooling time as well as during the measurement.

Nevertheless, the elevated basis temperature imposes a limit on the achievable phase definition jitter. In order to avoid significant systematic frequency shifts, the cyclotron excitation energy is limited. According to figure 5.12, a phase definition jitter of $\delta\phi_{\mathrm{in}} \simeq 15°$ is achievable with a resulting acceptable systematic shift of 70 ppt. For a 5 second measurement this translates into an achievable minimum jitter of the cyclotron frequency readout of

$$\frac{\delta\nu_+}{\nu_+} \ \leq \frac{15°}{360° \, 5s \, \nu_+} \sqrt{\tfrac{1}{6} + 1} \simeq 3.3 \cdot 10^{-10} \ \ \Rightarrow \ \mathrm{FWHM} \geq 7.8 \cdot 10^{-10}. \qquad (6.35)$$

The cyclotron frequency readout jitter causes a broadening of the recorded spinflip resonance of the same magnitude. Indeed, the corresponding *g*-factor resonance has

almost exactly the predicted linewidth, demonstrating that the cyclotron frequency readout precision is still the limiting factor, while true magnetic field fluctuations play a secondary role even on this improved level of precision.

6.2.3   Energy calibration

For the determination of the systematic frequency shifts the absolute cyclotron energy resulting from a certain excitation pulse strength has to be known. The simplest method to obtain this information is to measure the cyclotron frequency shift as a function of the pulse power. Since the cyclotron frequency shift, arising from the magnetic bottle and the relativistic mass increase, is proportional to the square of the cyclotron radius r_+^2[10], a linear relation to the pulse power is expected[10]. However, the statistical fluctuations due to magnetic field wander are larger than the expected systematic shifts. By repeatedly measuring the cyclotron frequency difference between successive measurements with randomly chosen excitation energies it is possible to beat the statistical fluctuations of the magnetic field and map out the frequency shift directly. Figure 6.6 shows the result of such a measurement. The frequency shift is clearly linear in the excitation power as expected, confirming the validity of the theory. From a fit to the measured data the parameter κ can be extracted which relates the excitation power with the cyclotron frequency shift in this specific setup:

$$\frac{\delta \nu_+}{\nu_+} = \kappa V_{\text{exc}}^2. \tag{6.36}$$

 By using an independently obtained value of the magnetic bottle strength in the PT, B_2, it is thus possible to establish a relation between the excitation amplitude and the true cyclotron radius via equations (3.26) and (3.36):

$$r_+ \simeq \sqrt{\frac{\kappa}{\frac{\omega_+^2}{2\,c^2} + \frac{B_2}{2\,B_0}}}\, V_{\text{exc}} \simeq 57(22) \frac{\upmu\text{m}}{V}\, V_{\text{exc}}. \tag{6.37}$$

The precision of the determined radius suffers from the limited knowledge of the magnetic bottle strength in the PT.

6.2.4 g-factor resonances

A total of eight resonances with varying cyclotron energies were recorded for the determination of the g-factor of $^{28}\text{Si}^{13+}$ with the PnA method. The resonances with the lowest energies almost entirely determine the g-factor value due to the amount of statistics. The high energy resonances mainly serve for the validation of the theoretically predicted scaling behavior. The energy dependence of the resonance centroids results mainly from the different relativistic scaling of the Larmor- and cyclotron frequency (see chapter 3.2.3) and is in perfect agreement with the theoretical prediction. This difference can be exploited by combining the fitted slope

---

[10]The cyclotron radius depends linearly on the pulse amplitude and the pulse power is quadratic in the amplitude.
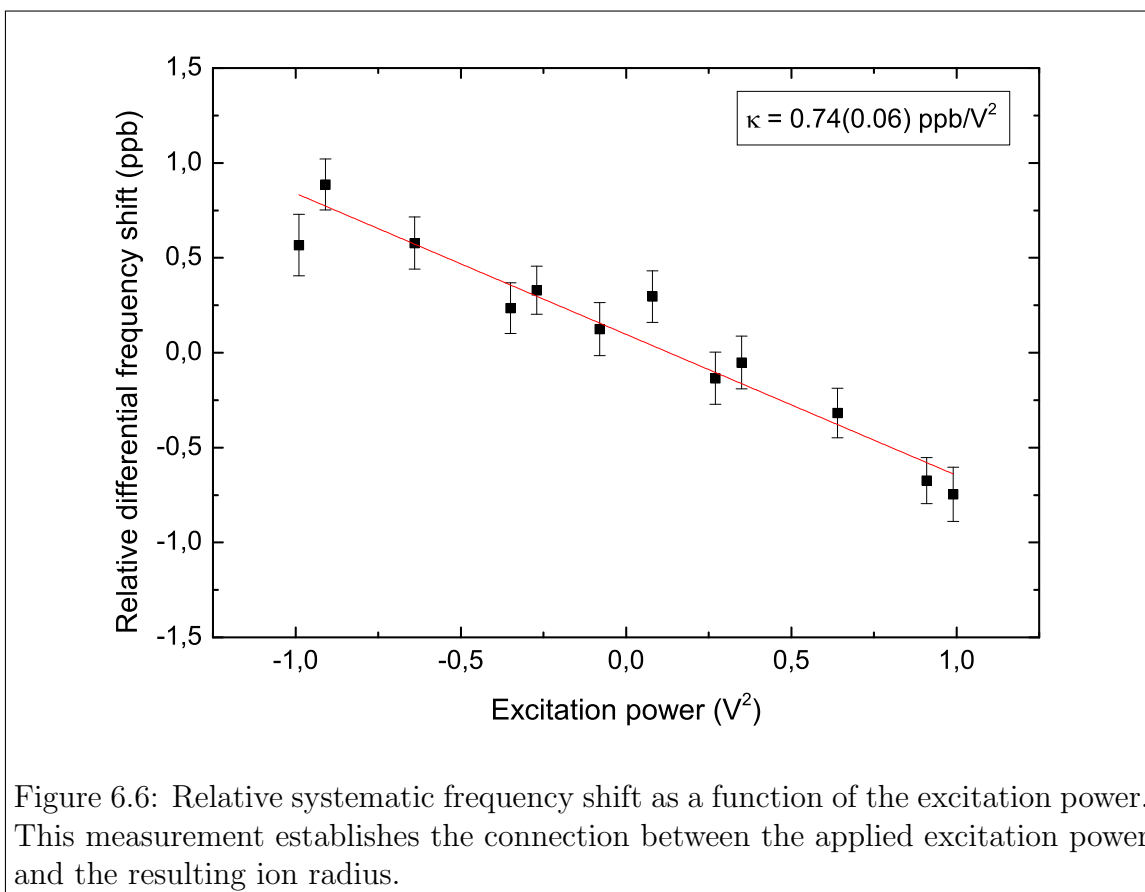
Figure 6.6: Relative systematic frequency shift as a function of the excitation power. This measurement establishes the connection between the applied excitation power and the resulting ion radius.

of the energy dependent centroids with the cyclotron frequency shift measurement in figure 6.6 to determine a significantly more precise value of the magnetic bottle strength B_2 (see next chapter). As predicted, the resonances show no observable asymmetry, a result of the low axial energy due to the improved detection system in combination with the electronic feedback, and the small residual magnetic inhomogeneity compared to previous experiments[11]. The linewidth of 0.8 ppb is in perfect agreement with the expectation from the phase definition jitter of 0.78 ppb, discussed in chapter 6.2.2. This demonstrates on the one hand the drastic improvement due to the phase sensitive detection, on the other hand it substantiates the advantage of improved cooling techniques, which would allow lower phase definition jitter. For coming experiments, the direct cooling with a cyclotron tank circuit will allow reaching an order of magnitude lower temperatures, allowing to fully exploit the possibilities of the PnA technique.

Similarly to the double-dip measurement, the final result is determined from a weighted fit to the corrected centroids of the individual resonances.

---

[11]The distance between AT and PT was increased compared to the original apparatus in order to reduce the influence of the ferromagnetic ring in the PT.
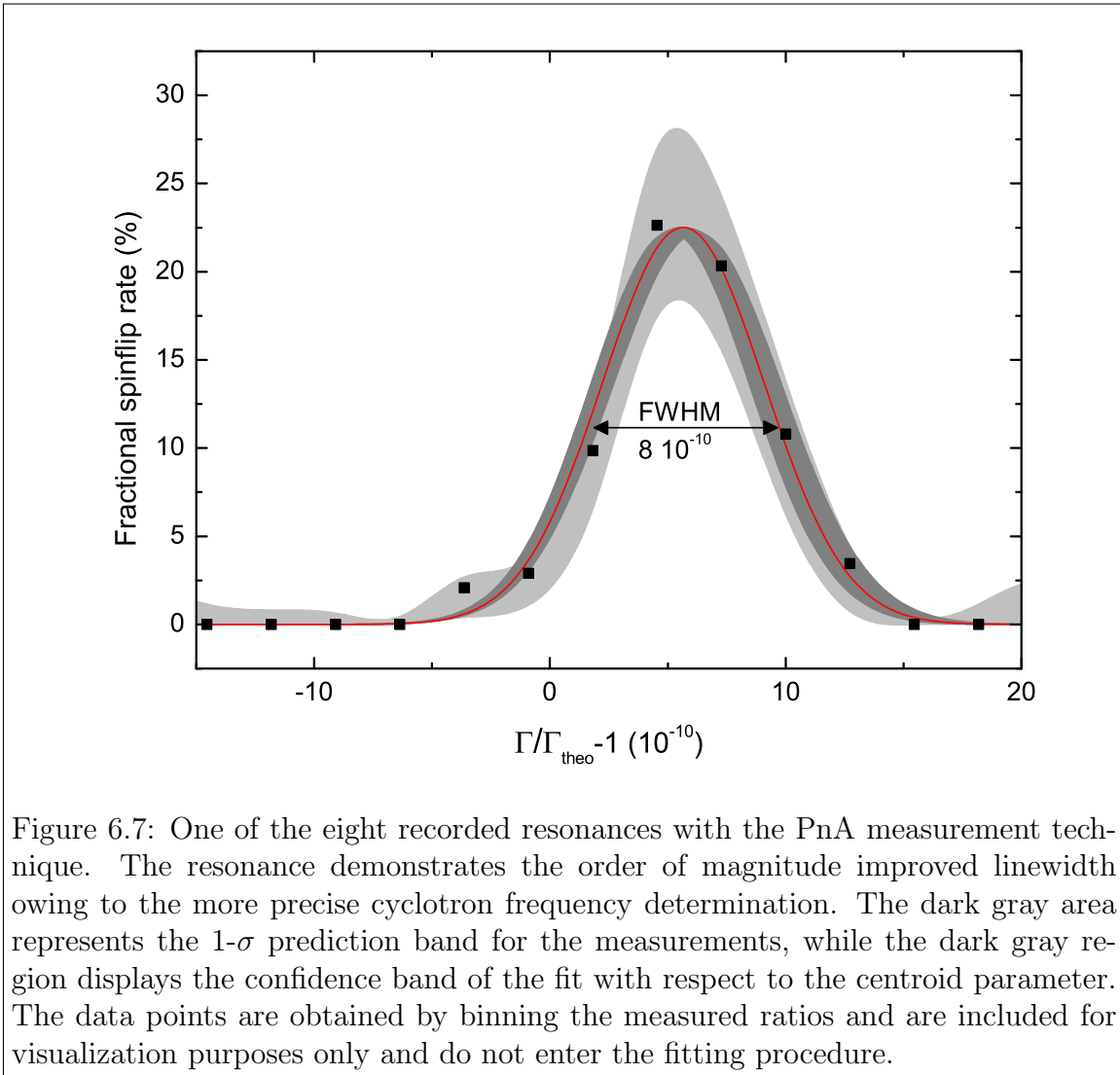
Figure 6.7: One of the eight recorded resonances with the PnA measurement technique. The resonance demonstrates the order of magnitude improved linewidth owing to the more precise cyclotron frequency determination. The dark gray area represents the 1-σ prediction band for the measurements, while the dark gray region displays the confidence band of the fit with respect to the centroid parameter. The data points are obtained by binning the measured ratios and are included for visualization purposes only and do not enter the fitting procedure.

6.2.5   Result and error budget

Although the individual effects contributing to the systematic uncertainty of the measurement are conceptually similar to the double-dip measurement, the different values of the experimental parameters change the error budget of the experiment. Although the PnA measurement principally allows the detection of small cyclotron amplitudes, the unavailability of the direct cyclotron tank circuit cooling during the measurement enforces the use of comparably large cyclotron energies. Simultaneously, the use of negative feedback during the PnA detection decreases the axial amplitude and thus the asymmetry and linewidth of the *g*-factor resonance. Below, only the most important systematic shifts are once more discussed, and the error budget with all contributions is presented.
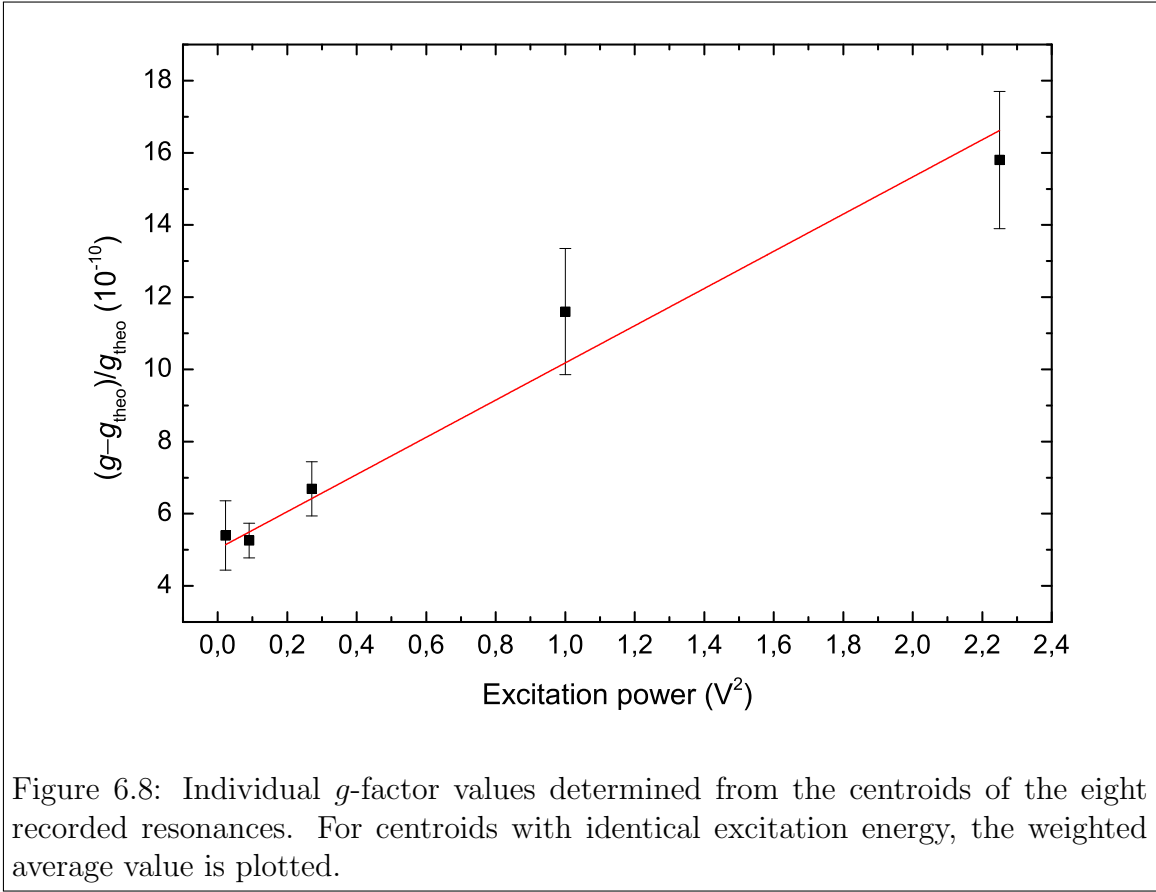
Figure 6.8: Individual *g*-factor values determined from the centroids of the eight recorded resonances. For centroids with identical excitation energy, the weighted average value is plotted.

6.2.6 Energy dependent shifts

Since the PnA measurement implements a direct detection of the cyclotron frequency, the contribution of the axial and magnetron frequency to the determined free cyclotron frequency is significantly reduced. However, the eigenfrequencies are now detected at different energies. The magnetron frequency is still deduced from a double-dip spectrum by sideband coupling to the axial mode. The temperature of the magnetron mode upon detection is thus very low: $|T_-| = \frac{\omega_-}{\omega_z} T_z \simeq 63\,\mathrm{mK}$. Furthermore, the invariance theorem suppresses the contribution of the magnetron frequency so far that the determined value can safely be regarded as the ideal magnetron frequency. The axial frequency is determined from a single dip spectrum at 4.8 K, but this temperature is still low enough to neglect any systematic shift on the cyclotron frequency. This was already true for the double-dip measurement at roughly 0.2 ppt, and this effect is now suppressed by an additional factor $\frac{\omega_z}{\omega_+} \simeq 1/40$ due to the direct measurement[12]. However, the uncertainty of the dip line splitting imposes a more severe limit for the determination of the cyclotron frequency. Using the same relative uncertainty as for the double-dip measurement, the accuracy of the

---

[12]The cyclotron frequency during the dip measurement shifts slightly due to the finite axial temperature, however this has no influence on the axial frequency, which is merely an input parameter to the invariance theorem which yields the cyclotron frequency at the time of the PnA cycle, not the axial frequency measurement.

PnA measurement in the current setup is bounded at 0.1 ppb $\cdot \frac{\omega_z}{\omega_+} \simeq 3$ ppt. While this is a severe relaxation compared to the double-dip technique, the axial frequency determination should be reviewed if the precision of the experiment is further improved in the future.

The energy dependence of the free cyclotron frequency determined with the PnA method originates almost entirely from the reduced cyclotron frequency:

$$\frac{\delta\nu_c}{\nu_c} = \left(\frac{\nu_+}{\nu_c}\right)^2 \frac{\delta\nu_+}{\nu_+} \simeq (1 - 0.7\text{‰})\,\delta\nu_+. \tag{6.38}$$

The energy scaling of the determined free cyclotron frequency thus reflects almost perfectly the inhomogeneity of the magnetic field, which also defines the scaling of the Larmor frequency. This is an important conceptual advantage of measuring the axial frequency independently at low cyclotron energy. Otherwise, the magnetic moment associated to the cyclotron motion would alter the axial frequency, canceling the scaling of the cyclotron frequency due to the magnetic inhomogeneity (almost) entirely:

$$\bar{\nu}_c = \sqrt{\bar{\nu}_+^2 + \bar{\nu}_z^2 + \nu_-^2} = \sqrt{(\nu_+ + \delta\nu_+)^2 + (\nu_z + \frac{\nu_+}{\nu_z}\delta\nu_+)^2 + \nu_-^2} \simeq \nu_c. \tag{6.39}$$

Here, $\bar{\nu}_+$ and $\bar{\nu}_z$ denote the respective eigenfrequencies measured at an elevated cyclotron temperature T_+. The disadvantage of this cancellation is that the ratio of Larmor and cyclotron frequency is now not anymore invariant with respect to the energy in the residual magnetic bottle. While the resulting systematic shift can be corrected, the jitter due to slightly different excitation energies between successive measurements would inevitably cause a clearly undesired broadening of the g-factor resonance.

Similar to the double-dip measurement, the largest contribution to the cyclotron frequency shift in the magnetic inhomogeneity comes from the finite axial energy rather than the cyclotron energy. However, due to the negative feedback applied during the measurement, this contribution is smaller (9 ppt) than in the previous measurement. In any case, the axial energy induced magnetic field shift does not find expression in the frequency ratio, as it affects both the Larmor and cyclotron frequency in a similar way.

Ultimately, only the relativistic mass increase causes a systematic shift of the frequency ratio Γ, because it causes dissimilar effects on the two frequencies. Although the systematic shift at the lowest excitation energy is only 14 ppt, by using excessively strong excitations it is possible to provoke significant systematic shifts (see figure 6.8). The slope of the determined g-factor values can be used to determine the cyclotron radius without the need to know B_2 explicitly:

$$r_+ = \sqrt{\frac{c^2}{2\,\pi^2\,\nu_+^2} \frac{\delta g(V_{\text{exc}})}{g}}. \tag{6.40}$$

In combination with equation (6.37), it is possible to deduce a very precise value of the magnetic bottle strength B_2:

$$B_2^{\mathrm{PT}} = 0.52(16) \, \frac{\mu\mathrm{T}}{\mathrm{mm}^2}. \tag{6.41}$$

This value is in perfect agreement with the independently obtained value presented in chapter 5.6.1, but is an order of magnitude more precise. The validity of the B_2 determination once again confirms the validity of the systematic shift calculation.

6.2.6.1 Static shifts

On top of the very low systematic shifts, the determined frequencies, especially the cyclotron frequency, is subject to the same static shifts that have been considered for the double-dip measurement. The two dominant contributions come from of the self-interaction of the ion with its charge and current via the trap electrodes. The image current shift becomes almost significant, due to the higher precision of the measurement, and is corrected for. The image charge shift, which is unchanged by the measurement method, is now the dominant source of uncertainty for the frequency ratio Γ. The limited knowledge of the position of the ion in the trap, especially in the axial direction, enforces a very conservative 5% uncertainty estimate of this contribution, corresponding to a contribution of 34 ppt to the final error budget. For future measurements this uncertainty has to be decreased by either increasing the trap radius or by very careful theoretical and experimental examination of this shift [87].

The tables 6.4, 6.5 and 6.6 summarize the considered systematic shifts and uncertainties. The error budget of the frequency ratio Γ_0 is obviously still dominated by

Effect	relative size (ppt)	uncertainty of final result (ppt)
Magnetic field inhomogeneity[13]	9	< 1
Special relativity	15	3
Electrostatic potential	$\ll 1$	$\ll 1$
g-factor lineshape	< 10	< 10
Sum (quadratic)	< 20	< 11

Table 6.4: Energy dependent systematic shifts

the static shifts, although the statistical uncertainty has been lowered by an order of magnitude. Similar to the double-dip result, the g-factor can be calculated from the corrected Γ_0 value. The result,

$$g_{\mathrm{exp}}^{\mathrm{PnA}} = 1.995\,348\,959\,04(7)(7)(80)^{14}, \tag{6.42}$$

---

[13]Shift of the cyclotron frequency. With the presented method magnetic inhomogeneity does not produce systematic shifts of the g-factor in leading order.

Effect	relative size (ppt)	uncertainty of final result (ppt)
Image current	20	10
Image charge	686	34
Dip lineshape	< 2.6	2.6
Timebase	< 10	< 10
Sum (quadratic)	686	< 37

Table 6.5: Static systematic shifts

Constant	relative uncertainty (ppt)
Electron mass in u	400
Ion mass in u	35
Sum	402

Table 6.6: External constants uncertainty

is again in perfect agreement with both the theoretical prediction and the double-dip result. However, it is entirely limited by the knowledge of the electron mass in atomic mass units. For this reason, the frequency ratio Γ_0, which is a direct result of the experiment and not subject to the uncertainty of external constants, is regarded as the true result of the experiment:

$$\Gamma_0^{\text{PnA}} = 3912.866\,064\,88(13)(13),\tag{6.43}$$

where the errors indicate the statistic and systematic uncertainty, respectively. As soon as the electron mass is independently measured to higher precision, this value can be transformed to an ultra high-precision g-factor.

6.2.7   Comparison with double-dip method

The above results clearly demonstrate that the PnA is superior to the double-dip method in all relevant concerns. Both results agree perfectly with each other as well as the theoretical prediction. If the temperature of the ion can be cooled better, e.g. with direct cyclotron cooling, the cyclotron temperature can be lower than in the double-dip case, which basically removes all energy dependent systematic shifts. Apart from the higher precision achievable with the PnA, it also removes the limitation due to the line splitting of the dip. This might be one of the most welcome improvements of the novel method, as it makes the cyclotron frequency determination basically independent from model-based lineshapes.

---

[14]The errors indicate the complete statistic and systematic experimental error of the PnA measurement and the external constant uncertainty, respectively.

6.2.7.1   Limitations and opportunities

The precision of the PnA measurement is limited by the amount of statistics collected during the data-taking, partly due to the limited amount of time, but also due to the low spin transition rate chosen. In further measurements, it might be advantageous to increase the microwave excitation power to increase the rate of detected spinflips. As long as the transition probability stays clear of the saturation limit around 50%, the resulting broadening of the line is negligible. In the current measurement, the transition rate was around 20% for all resonances, so that increasing the microwave power holds promise to increase the statistical precision by at least a factor of $\sqrt{2}$. Alternatively, the cyclotron frequency measurement precision can be increased by lowering the phase definition jitter, which is easily possible by decreasing the cyclotron temperature before the PnA cycle by direct cooling via the cyclotron resonator. The lower cyclotron temperature allows to decrease the phase definition jitter by a factor of 5 without increasing the systematic shifts. By increasing the measurement time, the statistical precision can in principal be arbitrarily increased, however the phase ambiguities caused by magnetic field fluctuations during the measurement period prevents the use of arbitrarily long measurement times. By stabilizing the magnetic field, as suggested in the outlook, longer measurement times will soon become accessible allowing a further increase of the already fascinating precision of the experiment.

If the cyclotron frequency precision can be increased, the precision of the axial frequency measurement via the dip spectrum will impose a limit in the low ppt regime. By applying the PnA method for the axial phase, rather than the cyclotron phase, it is possible to perform a phase sensitive measurement of the axial frequency. This will allow to beat the limit of the axial frequency, provided that the trapping voltage during the measurement is sufficiently stable to prevent excessive jitter.

Finally, the limit of the g-factor measurement will be given by the static frequency shifts, primarily the image charge shift. While this effect is only a weak limit for ions with low charge as e.g. $^{12}\text{C}^{5+}$, for highly charged ions the image charge effect will have to be controlled by either a direct measurement or an increase of the trap size. In any case, the PnA method offers plenty of room for further improvements.

7. Conclusions and Outlook

In the course of this thesis the g-factor of the electron bound in hydrogenlike silicon $^{28}\mathrm{Si}^{13+}$ was determined to a previously inconceivable accuracy:

$$g_{\mathrm{exp}}^{^{28}\mathrm{Si}^{13+}} = 1.995\,348\,959\,04(7)(7)(80). \tag{7.1}$$

The errors originate from the statistic and systematic uncertainties of the measured frequency ratio and the uncertainty of the tabulated electron mass, respectively. The excellent agreement with the value predicted by state of the art BS-QED calculations,

$$g_{\mathrm{theo}}^{^{28}\mathrm{Si}^{13+}} = 1.995\,348\,9580(17). \tag{7.2}$$

constitutes the most stringent test of BS-QED in strong electric fields [12]. The combination of theoretical prediction and experimental observation allows to verify the QED contributions to the electron g-factor with a precision of 0.8 ppm. If those contributions that have been already thoroughly tested by other experiments are left aside, the explicit BS-QED contributions are still tested to a level of 0.4‰.

The accuracy of the measurement was made possible by the development of a significantly improved Penning trap system and cryogenic precision electronics at the edge of feasibility on the one hand [88], and the invention and application of a novel frequency measurement technique, termed PnA [13], which enables to beat the previous precision limits by orders of magnitude on the other hand. This measurement constitutes the most accurate measurement of any atomic g-factor to date.

The order of magnitude improved precision of the experiment features prospects for fascinating future measurements, some of which will be discussed in the following. The dominant limitation of the experimental precision by the uncertainty of the tabulated electron mass leads to the first and most obvious application, the extraction of the electron mass from an improved determination of the g-factor of $^{12}\mathrm{C}^{5+}$. By

solving equation (6.27) for the electron mass, a simple relation between the measured frequency ratio Γ_0 and the theoretical g-factor prediction is established [89]:

$$m_e = \frac{g_\text{theo}}{2\,\Gamma_0}\,\frac{m_{^{12}\text{C}}}{q}.$$

(7.3)

Already with the present setup, an improvement of the tabulated electron mass value by more than an order of magnitude seems plausible. Further improvements that have been already initiated (see chapter 7.1), will probably extend the reach of the experiment even further. Furthermore, the measurement of other ions will allow even more stringent BS-QED tests. The extension to higher charge states gives access to stronger binding potentials, with possibly more pronounced consequences of hypothetical nonlinearities of QED with respect to the field tensor $F^{\mu\nu}$. The current setup is designed to allow charge-breeding of hydrogenlike calcium, where the expectation value of the electric field strength in the 1s state is significantly higher. Moreover, the measurement of the g-factor of multi electron systems, for example in lithium like ions, allows the investigation of interelectronic interaction and correlation.

Finally, g-factor determinations also allow the determination of nuclear masses. This is particularly interesting since the use of the Larmor frequency as a probe of the local magnetic field eliminates systematic shifts arising from dissimilar equilibrium positions of different ions which are a troubling source of uncertainty for ultra high precision mass comparisons.

7.1   Future improvements

This chapter will introduce some of the technical improvements that will enable further refinement of the measurements. The analysis of the PnA measurement has clearly revealed the major sources of limitation for the measurement precision. Apart from the image charge shift, which can be easily reduced by increasing the radius of the PT[1], the magnetic field wander during and between successive measurements in combination with the finite base temperature of the ion before excitation restrict the further decrease of the g-factor linewidth.

For both sources of limitation, appropriate solution approaches have been driven forth within this thesis.

7.1.1   Magnetic field self-stabilization coil

The random fluctuations of the magnetic field first and foremost yield an upper bound for the usable evolution time T_evol of the PnA cycle, since the fluctuations

---

[1]Only the inner PT electrodes have to be enlarged, which helps to keep the length of the trap tower within reasonable limits.

themselves cancel to first order in the ratio Γ. If the typical fluctuations of the determined phase, which depend linearly on the evolution time, become comparable to π, the unambiguous phase unwrapping becomes impossible. The maximum achievable frequency readout precision then reads:

$$\frac{\delta\nu_+}{\nu_+} \geq \frac{\delta\phi_{\mathrm{in}}}{2\pi\, T_{\mathrm{evol}}\, \nu_+}. \tag{7.4}$$

Obviously, for a certain initial phase resolution, given by the amount of accepted systematic frequency shift and the base temperature, the resolution only depends on the available measurement time. By increasing the stability of the magnetic field, longer evolution periods become accessible.

The magnetic field fluctuations at the location of the ion can be composed of fluctuations of the external magnetic field, originating from changes of the local earth magnetic field, motion of nearby macroscopic ferromagnetic objects and magnetic disturbances from electronic devices, and fluctuations of the internal magnetic field, caused by changes of the operating parameters of the superconducting magnet [90]. For one thing, the magnetic flux trapped by the superconducting solenoids can change due to the Flux-Creep effect [91]. However, this contribution is typically displaced by the consequences of changes in the temperature and pressure of the cryogenic liquids in the dewars of the experiment. The fluctuating pressure in the cryogenic dewars causes susceptibility changes of materials in the bore of the magnet, and changes of the geometric dimensions of the solenoids. Furthermore, the pressure change can induce excessive boiling of the cryogenic liquids, which can generate a change of the geometrical position of the setup in the magnetic field of the solenoid due to thermal contraction of the mechanical supports of the setup.

By adding a self-contained superconducting solenoid of suitable geometry which traps the magnetic flux in the region around the trap, the magnetic field at one specific location can be made invariant under changes of the external field. This technique was proposed and employed by G. Gabrielse for shielding complete magnets against external disturbances [92]. However, by winding of the coil directly around the trap chamber, the magnetic field at the ion's location becomes not only shielded against external fluctuations but also against all fluctuations inside the magnet bore[2] and even against the result of translations along the magnetic field lines. Furthermore, because the magnetic field inside the coil is very similar to the surrounding field, the diffusion of flux quanta is strongly suppressed.

First tests of the shielding coil suggest a successful shielding of external fluctuations by more than 2 orders of magnitude. The characterization of the shielding coil and its consequences for the experiment is part of the Ph.D. thesis of A. Wagner.

---

[2]Provided that these can be considered sufficiently homogeneous across the spatial extent of the shielding coil.

7.1.2 Direct cyclotron mode cooling

Additional to the stabilization of the magnetic field, the initial phase jitter can be
lowered by decreasing the base temperature of the ion in the cyclotron mode. A
straightforward possibility to achieve a lower temperature is to couple the cyclotron
mode directly to a tank circuit. This way, the cyclotron mode can be brought into
thermal equilibrium with the physical temperature of the setup, which amounts
to 4.2 K [37]. This corresponds to a reduction of the cyclotron temperature by
at least a factor 20, or even more if negative feedback is applied to the cyclotron
resonator. Considering that the systematic shifts of the cyclotron frequency scales
linearly with the mode energy, this holds promise for a drastic improvement in
the achievable precision. Furthermore, a cryogenic switch was introduced into the
setup which allows to shift the resonance frequency of the axial tank circuit by a
large amount. Doing so, the axial mode is practically decoupled from the thermal
bath and can be brought into thermal equilibrium with the cyclotron mode via
radiofrequency sideband coupling. The achievable axial temperature in this case
amounts to $T_z = \frac{\nu_z}{\nu_c} T_+ \simeq 52$ mK, which holds promise for eventually breaking the
ppt barrier.

7.1.3 Beating the phase definition jitter:
Non-classical motion

If the base temperature of the ion is further reduced, the PnA method, combined
with the magnetic bottle, opens a fascinating window into the quantum world. Cool-
ing into the motional ground state [93], which seems on the long term possible via
e.g. sympathetic resolved sideband laser cooling, allows to prepare well-defined ini-
tial states, which become essentially independent of the base temperature in this
limit. While the initial phase uncertainty due to the thermal motion vanishes, quan-
tum effects start limiting the jitter of the measured phase. This is not surprising
considering that the (spatial) phase operator of quantum mechanics [94] is only con-
sistently defined for classical, coherent states. While the state that is measured,
after application of the amplification pulse of PnA, can be clearly represented as
a coherent state, the initial state can be potentially non-classical. In particular, it
might be possible to prepare a squeezed vacuum state from the ground state[3], which
allows to achieve phase resolutions better than the quantum limit for the coherent
state, roughly given by the number-phase uncertainty relation [95]:

$$\Delta\phi \sim \frac{90°}{\pi\sqrt{N}}. \tag{7.5}$$

However, already the quantum limited coherent states allow to achieve a similar
phase resolution as the current experiment at a fractional relativistic shift of only

---

[3]Conceptually this state preparation is very similar to the classical quadrature squeezing which
is already currently employed for purely classical states (see chapter 3.4.1).

$3.3 \cdot 10^{-17}$, or a 1° resolution at only $3.3 \cdot 10^{-15}$, giving an idea of the prospects for precision measurements. However, the possibilities of the PnA method seem to reach even further. The ability to transfer the quantum mechanical state information onto classical coherent states might allow quantum state tomography [96] of the initial correlated state. The initial state can potentially entangle N arbitrary number states. A weak interaction of these states might be controllably introduced by the induced image charge. Finally, the addition of a magnetic inhomogeneity, which is already existing in the AT, can possibly provoke the initial state to (partially) collapse towards a Fock number state, which might be temporally resolved by the state tomography and allows to get detailed insight into the transition from the quantum world to classical mechanics. Of course, there might and will be other limits, however, they first have to come.

This likewise speculative and highly fascinating perspective concludes this thesis.

References

[1] R. Feynman. *QED: The Strange Theory of Light and Matter.* Princeton University Press (1985).

[2] I. Aitchison and H. A. *Gauge Theories in Particle Physics: A Practical Introduction.* Institute of Physics (2003).

[3] T. Aoyama, M. Hayakawa, T. Kinoshita, and M. Nio. *Revised value of the eighth-order QED contribution to the anomalous magnetic moment of the electron.* Phys. Rev. D **77**, 053012 (2008).

[4] F. Scheck. *Theoretische Physik 4, Quantisierte Felder.* Springer-Verlag (2001).

[5] R. Van Dyck Jr, P. Schwinberg, and H. Dehmelt. *Electron magnetic moment from geonium spectra: Early experiments and background concepts.* Phys. Rev. D **34**(3), 722 (1986).

[6] D. Hanneke, S. Fogwell, and G. Gabrielse. *New measurement of the electron magnetic moment and the fine structure constant.* Phys. Rev. Lett. **100**(12), 120801 (2008).

[7] P. Seelig *et al. Ground State Hyperfine Splitting of Hydrogenlike $^{207}Pb^{81+}$ by Laser Excitation of a Bunched Ion Beam in the GSI Experimental Storage Ring.* Phys. Rev. Lett. **81**, 4824–4827 (1998).

[8] T. Stöhlker *et al. 1s Lamb shift in hydrogenlike uranium measured on cooled, decelerated ion beams.* Phys. Rev. Lett. **85**(15), 3109–3112 (2000).

[9] H. Dehmelt. *Continuous Stern-Gerlach effect: Principle and idealized apparatus.* Proc. Natl. Acad. Sci. **83**(8), 2291 (1986).

[10] H. Häffner *et al. High-Accuracy Measurement of the Magnetic Moment Anomaly of the Electron Bound in Hydrogenlike Carbon.* Phys. Rev. Lett. **85**(25), 5308–5311 (2000).

[11] J. Verdú *et al. Electronic g Factor of Hydrogenlike Oxygen $^{16}O^{7+}$.* Phys. Rev. Lett. **92**(9), 093002 (2004).

[12] S. Sturm *et al.* *g Factor of Hydrogenlike* ^{28}Si^{13+}. Phys. Rev. Lett. **107**, 023002 (2011).

[13] S. Sturm, A. Wagner, B. Schabinger, and K. Blaum. *Phase-Sensitive Cyclotron Frequency Measurements at Ultralow Energies.* Phys. Rev. Lett. **107**, 143003 (2011).

[14] P. A. M. Dirac. *The Quantum Theory of the Emission and Absorption of Radiation.* Proceedings of the Royal Society of London. Series A **114**(767), 243–265 (1927).

[15] W. Lamb and R. Retherford. *Fine structure of the hydrogen atom by a microwave method.* Phys. Rev. **72**(3), 241–243 (1947).

[16] G. Ross. *Grand unified theories.* Westview Press (1984).

[17] R. Bouchendira *et al.* *New Determination of the Fine Structure Constant and Test of the Quantum Electrodynamics.* Phys. Rev. Lett. **106**, 080801 (2011).

[18] M. Acciarri *et al.* *Tests of QED at LEP energies using* e^+ $e^- \rightarrow \gamma\gamma(\gamma)$ *and* e^+ $e^- \rightarrow l^+l^-\gamma\gamma$. Phys. Lett. B **353**(1), 136–144 (1995).

[19] P. Kusch and H. Foley. *The magnetic moment of the electron.* Phys. Rev. **74**(3), 250 (1948).

[20] T. Kinoshita. *Theory of the Anomalous Magnetic Moment of the Electron-Numerical Approach.* Quantum Electrodynamics 218–321 (1990).

[21] J. Miller, E. De Rafael, and B. Lee Roberts. *Muon (g- 2): experiment and theory.* Rep. Prog. Phys. **70**, 795 (2007).

[22] T. Beier. *The g_j factor of a bound electron and the hyperfine structure splitting in hydrogenlike ions.* Phys. Rep. **339**(2), 79–213 (2000).

[23] G. Breit. *The magnetic moment of the electron.* Nature **122**(3078), 649–649 (1928).

[24] V. Shabaev and V. Yerokhin. *Recoil Correction to the Bound-Electron g Factor in H-like Atoms to All orders in* αZ. Phys. Rev. Lett. **88**(9), 91801 (2002).

[25] J. Zatorski, N. Oreshkina, C. Keitel, and Z. Harman. *Nuclear Shape Effect on the g Factor of Hydrogenlike Ions.* Arxiv preprint arXiv:1110.3330 (2011).

[26] A. Nefiodov, G. Plunien, and G. Soff. *Nuclear-polarization correction to the bound-electron g factor in heavy hydrogenlike ions.* Phys. Rev. Lett. **89**(8), 81802 (2002).

[27] J. Zatorski, Z. Harman, and C. H. Keitel. *private communication* (2010).

[28] L. Brown and G. Gabrielse. *Precision spectroscopy of a charged particle in an imperfect Penning trap.* Phys. Rev. A **25**(4), 2423 (1982).

[29] L. Brown and G. Gabrielse. *Geonium theory: Physics of a single electron or ion in a Penning trap.* Rev. Mod. Phys. **58**(1), 233 (1986).

[30] G. Gabrielse. *Why Is Sideband Mass Spectrometry Possible with Ions in a Penning Trap?* Phys. Rev. Lett. **102**, 172501 (2009).

[31] J. Tan and G. Gabrielse. *One electron in an orthogonalized cylindrical Penning trap.* Appl. Phys. Lett. **55**(20), 2144–2146 (1989).

[32] H. Bateman. *The transformation of the electrodynamical equations.* Proceedings of the London Mathematical Society **2**(1), 223–264 (1910).

[33] W. Gerlach and O. Stern. *Der Experimentelle Nachweis der Richtungsquantelung im Magnetfeld.* Zeitschrift für Physik A Hadrons and Nuclei **9**(1), 349–352 (1922).

[34] J. Verdú. *Ultrapräzise Messung des elektronischen g-Faktors in wasserstoffähnlichem Sauerstoff.* Ph.D. thesis, Johannes Gutenberg-Universität Mainz (2003).

[35] L. Thomas. *The motion of the spinning electron.* Nature **117**(2945), 514–514 (1926).

[36] F. Combley, F. Farley, J. Field, and E. Picasso. *g-2 Experiments as a Test of Special Relativity.* Phys. Rev. Lett. **42**(21), 1383–1385 (1979).

[37] H. Häffner. *Präzisionsmessung des magnetischen Moments des Elektrons in wasserstoffähnlichem Kohlenstoff.* Ph.D. thesis, Johannes Gutenberg-Universität Mainz (2000).

[38] S. Eliseev *et al.* *Octupolar excitation of ions stored in a Penning trap mass spectrometer–A study performed at SHIPTRAP.* Int. J. Mass spectrom. **262**(1-2), 45–50 (2007).

[39] R. Ringle *et al.* *Octupolar excitation of ion motion in a Penning trap–A study performed at LEBIT.* Int. J. Mass spectrom. **262**(1-2), 33–44 (2007).

[40] M. Tabor. *Chaos and integrability in nonlinear dynamics: an introduction.* Wiley New York (1989).

[41] S. Ulmer. *First Observation of Spin Flips with a Single Proton Stored in a Cryogenic Penning Trap.* Ph.D. thesis, Ruperto-Carola University of Heidelberg (2011).

[42] V. Natarajan, F. DiFilippo, and D. Pritchard. *Classical squeezing of an oscillator for subthermal noise operation.* Phys. Rev. Lett. **74**(15), 2855–2858 (1995).

[43] E. Cornell, R. Weisskoff, K. Boyce, and D. Pritchard. *Mode coupling in a Penning trap: π pulses and a classical avoided crossing.* Phys. Rev. A **41**(1), 312–315 (1990).

[44] S. Stahl. *Aufbau eines Experimentes zur Bestimmung elektronischer g-Faktoren.* Ph.D. thesis, Johannes Gutenberg-Universität Mainz (1998).

[45] N. Hermanspahn. *Das magnetische Moment des Elektrons gebunden in wasserstoffartigem Kohlenstoff (C^{5+}).* Ph.D. thesis, Johannes Gutenberg-Universität Mainz (1999).

[46] B. Schabinger. *Ein Experiment zur Bestimmung des g-Faktors des gebundenen Elektrons in wasserstoff- und lithiumähnlichen mittelschweren Ionen.* Ph.D. thesis, Johannes Gutenberg-Universität Mainz (2011).

[47] J. Alonso *et al. A miniature electron-beam ion source for in-trap creation of highly charged ions.* Rev. Sci. Instrum. **77**, 03A901 (2006).

[48] J. Alonso. *Development of an Experiment for Ultrahigh-Precision g-Factor Measurements in a Penning-Trap Setup.* Ph.D. thesis, Johannes Gutenberg-Universität, Mainz (2007).

[49] stahl electronics.com. *UM 1-14 and UM 1-5* (2008).

[50] J. Johnson. *Thermal agitation of electricity in conductors.* Phys. Rev. **32**(1), 97 (1928).

[51] J. Nilsson and S. Riedel. *Electric circuits*, vol. 8. Prentice Hall (2009).

[52] D. Camin, G. PESS1NA, and E. Previtali. *Cryogenic Semiconductor Electronics.* Jpn. J. Appi. Phys. Vol **37**, 37–2 (1998).

[53] B. Ivanov *et al. Cryogenic ultra-low-noise SiGe transistor amplifier.* Rev. Sci. Instrum. **82**, 104705 (2011).

[54] A. Marshall, C. Hendrickson, and G. Jackson. *Fourier transform ion cyclotron resonance mass spectrometry: a primer.* Mass Spectrom. Rev. **17**(1), 1–35 (1998).

[55] A. Podell. *A functional GaAs FET noise model.* Electron Devices, IEEE Transactions on **28**(5), 511–517 (1981).

[56] R. Kirschman and J. Lipa. *Further evaluation of GaAs FETs for cryogenic readout.* In *Proceedings of SPIE*, vol. 350 (1946).

[57] K. H. Lundberg. *Noise Sources in Bulk CMOS.*

[58] C. Sah. *Fundamentals of solid-state electronics.* World Scientific Pub Co Inc (1991).

[59] J. Miller. *Dependence of the input impedance of a three-electrode vacuum tube upon the load in the plate circuit*, vol. 351. Govt. Print. Off. (1919).

[60] J. Ketelaer *et al. TRIGA-SPEC: A setup for mass spectrometry and laser spectroscopy at the research reactor TRIGA Mainz.* Nucl. Instrum. Methods Phys. Res., Sect. A **594**(2), 162–177 (2008).

[61] R. Von Hahn *et al. CSR-a cryogenic storage ring at MPI-K.* In *Proc. European Part. Acc. Conf., Lucerne, Switzerland* (2004).

[62] J. Repp *et al. PENTATRAP: A novel cryogenic multi-Penning trap experiment for high-precision mass measurements on highly charged ions.* Arxiv preprint arXiv:1110.2919 (2011).

[63] M. Skolnik *et al. Radar handbook*, vol. 2. McGraw-Hill New York (1990).

[64] D. Brian Richard. *Cooling and self-excitation of a one-electron oscillator.* Ph.D. thesis, Harvard University (2003).

[65] S. Cavassila *et al. Cramér–Rao bounds: an evaluation tool for quantitation.* NMR Biomed. **14**(4), 278–283 (2001).

[66] B. D'Urso *et al. Single-particle self-excited oscillator.* Phys. Rev. Lett. **94**(11), 113002 (2005).

[67] I. Bergström *et al. High-precision mass measurements of hydrogen-like $^{24}Mg^{11+}$ and $^{26}Mg^{11+}$ ions in a Penning trap.* Eur. Phys. J. D **22**(1), 41–45 (2003).

[68] K. Pachucki, A. Czarnecki, U. Jentschura, and V. Yerokhin. *Complete two-loop correction to the bound-electron g factor.* Phys. Rev. A **72**(2), 022108 (2005).

[69] R. Cody, R. Hein, S. Goodman, and A. Marshall. *Stored waveform inverse Fourier transform excitation for obtaining increased parent ion selectivity in collisionally activated dissociation: preliminary results.* Rapid Commun. Mass Spectrom. **1**(6), 99–102 (1987).

[70] I. Sobol. *Die Monte-Carlo-Methode.* VEB Deutscher Verl. der Wissenschaften (1983).

[71] S. Rainville, J. Thompson, and D. Pritchard. *An ion balance for ultra-high-precision atomic mass measurements.* Science **303**(5656), 334 (2004).

[72] E. Cornell *et al. Single-ion cyclotron resonance measurement of $M(CO^+)/M$ (N_2^+).* Phys. Rev. Lett. **63**(16), 1674–1677 (1989).

[73] D. Pritchard, S. Rainville *et al. A two-ion balance for high precision mass spectrometry.* Ph.D. thesis, Massachusetts Institute of Technology (2003).

[74] D. Sullivan, N. I. of Standards, and T. (US). *Characterization of clocks and oscillators*. US Dept. of Commerce, National Institute of Standards and Technology (1990).

[75] S. Stahl *et al.* *Phase-sensitive measurement of trapped particle motions*. J. Phys. B: At. Mol. Opt. Phys. **38**, 297 (2005).

[76] A. Van den Bos. *Parameter estimation for scientists and engineers*. Wiley Online Library (2007).

[77] V. Natarajan. *Penning trap mass spectroscopy at 0.1 ppb*. Ph.D. thesis, Massachusetts Institute of Technology (1993).

[78] R. Van Dyck Jr, F. Moore, D. Farnham, and P. Schwinberg. *Number dependency in the compensated Penning trap*. Phys. Rev. A **40**(11), 6308 (1989).

[79] *The NIST Reference on Constants, Units, and Uncertainty*. (2010). URL http://physics.nist.gov.

[80] P. J. Mohr, B. N. Taylor, and D. B. Newell. *CODATA recommended values of the fundamental physical constants: 2006*. Rev. Mod. Phys. **80**(2), 633–730 (2008).

[81] W. Martin and R. Zalubas. *Energy levels of silicon, Si I through Si XIV*. American Chemical Society and the American Institute of Physics for the National Bureau of Standards (1983).

[82] I. Angeli. *A consistent set of nuclear rms charge radii: properties of the radius surface $R(N, Z)$*. At. Data Nucl. Data Tables **87**(2), 185–206 (2004).

[83] S. Karshenboim. *Precision physics of simple atoms: QED tests, nuclear structure and fundamental constants*. Phys. Rep. **422**(1-2), 1–63 (2005).

[84] H. A. Schuessler, E. N. Fortson, and H. G. Dehmelt. *Hyperfine Structure of the Ground State of ^{3}He$^+$ by the Ion-Storage Exchange-Collision Technique*. Phys. Rev. **187**, 5–38 (1969).

[85] M. Prior and E. Wang. *Hyperfine structure of the 2s state of $^3He^+$*. Phys. Rev. A **16**(1), 6 (1977).

[86] P. Beiersdorfer *et al.* *Hyperfine structure of heavy hydrogen-like ions*. Nucl. Instrum. Methods Phys. Res., Sect. B **205**, 62–65 (2003).

[87] J. Porto. *Series solution for the image charge fields in arbitrary cylindrically symmetric Penning traps*. Phys. Rev. A **64**(2), 023403 (2001).

[88] S. Sturm *et al.* *On g-factor experiments with individual ions*. J. Phys. B: At. Mol. Opt. Phys. **43**, 074016 (2010).

[89] T. Beier *et al.* *New determination of the electron's mass.* Phys. Rev. Lett. **88**(1), 11603 (2001).

[90] R. Van Dyck Jr, D. Farnham, S. Zafonte, and P. Schwinberg. *Ultrastable superconducting magnet system for a penning trap mass spectrometer.* Rev. Sci. Instrum. **70**, 1665 (1999).

[91] R. G. Mints. *Flux creep and flux jumping.* Phys. Rev. B **53**, 12311–12317 (1996).

[92] G. Gabrielse and J. Tan. *Self-shielding superconducting solenoid systems.* J. Appl. Phys. **63**(10), 5143–5148 (1988).

[93] C. Monroe *et al.* *Resolved-Sideband Raman Cooling of a Bound Atom to the 3D Zero-Point Energy.* Phys. Rev. Lett. **75**, 4011–4014 (1995).

[94] B. Varga and S. Aks. *Phase operator for the harmonic oscillator.* Phys. Lett. A **31**(1), 40–41 (1970).

[95] P. Carruthers and M. Nieto. *Coherent states and the number-phase uncertainty relation.* Phys. Rev. Lett.. **14**(11), 387–389 (1965).

[96] U. Leonhardt. *Quantum-state tomography and discrete Wigner function.* Phys. Rev. Lett. **74**(21), 4101–4105 (1995).

Lebenslauf

Sven Sturm
geboren am 16.06.1981 in Koblenz
Staatsangehörigkeit: deutsch

wohnhaft: Willi-Wolf-Straße 24
55128 Mainz

Ausbildung

1987 bis 1991	Grundschule Kobern-Gondorf
1991 bis Juni 2000	Hilda Gymnasium Koblenz
2000 bis 2001	Zivildienst beim Deutschen Roten Kreuz, Ausbildung zum Rettungssanitäter
2001 bis 2007	Physik Studium an der Ruprecht-Karl-Universität Heidelberg
Juli/August 2005	Sommerstudent am CERN/Genf
April 2006 bis April 2007	Diplomarbeit in Experimentalphysik
Juni 2007 bis Dezember 2010	Wissenschaftlicher Mitarbeiter am Institut für Physik der Johannes Gutenberg-Universität Mainz
Januar 2010 bis Dezember 2011	Wissenschaftlicher Mitarbeiter am Max-Planck-Institut für Kernphysik, Heidelberg

Hochschulprüfungen

März 2004	Vordiplom in Physik
Juni 2007	Diplom in Physik

Auszeichnungen

2008	Wolfgang-Paul Studienpreis der Deutschen Gesellschaft für Massenspektrometrie

Familie

Familienstand	ledig
Mai 2006	Geburt der Tochter Tabea

Danksagung

Als erstes möchte ich *Klaus Blaum* danken, für das Vertrauen, die Freiheit und die Freundschaft, die ich genießen durfte. Du hast mir die Möglichkeit gegeben, meine teilweise verrückten Ideen umzusetzen, und schaffst dabei mit Deinem Optimismus und Deiner bedingungslosen Unterstützung die besten Vorraussetzungen für eine kreative Arbeit. Das Umfeld und die Atmosphäre die Du geschaffen hast sind unvergleichlich und machen das Arbeiten mit Dir zur Freude, genauso wie Deine Begeisterungsfähigkeit und Passion für die Physik. Deine Ambition ist mitreißend und macht alles möglich. Gleichzeitig kann man sich auf Dich jederzeit und bedingungslos verlassen, sowohl beruflich wie auch privat. Danke, dass Du mir in so vielen Situationen immer wieder geholfen hast.

Günter Werth danke ich für die viele Unterstützung, vor allem auch mit diversen Manuskripten, genauso wie für die hochinteressanten Gespräche, bei Denen ich immer wieder von der Weitsicht und Erfahrung beeindruckt war. Danke.

Bei meiner Laborkollegin *Anke Wagner* möchte ich mich für die gemeinsame Zeit im Labor, aber auch für die Freundschaft und die vielen schönen Erinnerungen bedanken. Du hast mich immer unterstützt und dabei viele meiner Macken ertragen müssen. Danke, dass Du mir so unzählige Male geholfen hast, und mir viele Probleme vom Hals gehalten hast. Ich hoffe Dir hat die Zeit genauso viel Spaß gemacht wie mir ! Ich wünsche Dir, dass sich Deine Arbeit bald auszahlt und Du gute Ergebnisse bekommst !

Birgit Schabinger möchte ich ebenso für die gemeinsame Zeit und Unterstützung danken. Deine Sorgfältigkeit hat uns viele Male geholfen und die Aufdeckung vieler Effekte ermöglicht. Ich glaube wir haben uns sehr gut ergänzt. Ich wünsche Dir viel Erfolg für Deine Zukunft !

Bei den Mitgliedern des Proton Teams, *Stefan Ulmer*, *Crícia Rodegheri*, *Holger Kracke*, *Andreas Moser*, möchte ich mich für die unvergleichliche Atmosphäre und die tolle gemeinsame Zeit, aber auch für den unendlich wertvollen Erfahrungsaustausch zwischen unseren Experimenten bedanken. Es ist toll, in einer solchen Gruppe zu arbeiten ! Ich bin mir sicher, dass sich Eure Arbeit bald auszahlt.

Bei *Stefan Ulmer* möchte ich mich besonders bedanken, für die vielen inspirierenden Gespräche und Deine unglaubliche Begeisterung für die Physik und Deine Arbeit. Dein Wissen und Dein Können hat unglaublich viel zum Erfolg unserer Gruppe beigetragen. Vielen Dank !